



UNIVERSITAT ROVIRA I VIRGILI

## CATALYTIC CONVERSION OF SYNGAS TO ALCOHOLS AND HYDROCARBONS OVER TRANSITION METAL-BASED MICRO/MESOPOROUS CATALYSTS

Jordi Plana Pallejà

**ADVERTIMENT.** L'accés als continguts d'aquesta tesi doctoral i la seva utilització ha de respectar els drets de la persona autora. Pot ser utilitzada per a consulta o estudi personal, així com en activitats o materials d'investigació i docència en els termes establerts a l'art. 32 del Text Refós de la Llei de Propietat Intel·lectual (RDL 1/1996). Per altres utilitzacions es requereix l'autorització prèvia i expressa de la persona autora. En qualsevol cas, en la utilització dels seus continguts caldrà indicar de forma clara el nom i cognoms de la persona autora i el títol de la tesi doctoral. No s'autoritza la seva reproducció o altres formes d'explotació efectuades amb finalitats de lucre ni la seva comunicació pública des d'un lloc aliè al servei TDX. Tampoc s'autoritza la presentació del seu contingut en una finestra o marc aliè a TDX (framing). Aquesta reserva de drets afecta tant als continguts de la tesi com als seus resums i índexs.

**ADVERTENCIA.** El acceso a los contenidos de esta tesis doctoral y su utilización debe respetar los derechos de la persona autora. Puede ser utilizada para consulta o estudio personal, así como en actividades o materiales de investigación y docencia en los términos establecidos en el art. 32 del Texto Refundido de la Ley de Propiedad Intelectual (RDL 1/1996). Para otros usos se requiere la autorización previa y expresa de la persona autora. En cualquier caso, en la utilización de sus contenidos se deberá indicar de forma clara el nombre y apellidos de la persona autora y el título de la tesis doctoral. No se autoriza su reproducción u otras formas de explotación efectuadas con fines lucrativos ni su comunicación pública desde un sitio ajeno al servicio TDR. Tampoco se autoriza la presentación de su contenido en una ventana o marco ajeno a TDR (framing). Esta reserva de derechos afecta tanto al contenido de la tesis como a sus resúmenes e índices.

**WARNING.** Access to the contents of this doctoral thesis and its use must respect the rights of the author. It can be used for reference or private study, as well as research and learning activities or materials in the terms established by the 32nd article of the Spanish Consolidated Copyright Act (RDL 1/1996). Express and previous authorization of the author is required for any other uses. In any case, when using its content, full name of the author and title of the thesis must be clearly indicated. Reproduction or other forms of for profit use or public communication from outside TDX service is not allowed. Presentation of its content in a window or frame external to TDX (framing) is not authorized either. These rights affect both the content of the thesis and its abstracts and indexes.

Jordi Plana Pallejà

**Catalytic conversion of syngas to  
alcohols and hydrocarbons over  
transition metal-based  
micro/mesoporous catalysts**

Doctoral Thesis

2018



UNIVERSITAT ROVIRA i VIRGILI

UNIVERSITAT ROVIRA I VIRGILI

CATALYTIC CONVERSION OF SYNGAS TO ALCOHOLS AND HYDROCARBONS OVER TRANSITION METAL-BASED  
MICRO/MESOPOROUS CATALYSTS

Jordi Plana Pallejà

UNIVERSITAT ROVIRA I VIRGILI

CATALYTIC CONVERSION OF SYNGAS TO ALCOHOLS AND HYDROCARBONS OVER TRANSITION METAL-BASED

MICRO/MESOPOROUS CATALYSTS

Jordi Plana Pallejà

Jordi Plana Pallejà

**Catalytic conversion of syngas to  
alcohols and hydrocarbons over  
transition metal-based  
micro/mesoporous catalysts**

Doctoral Thesis

2018

Supervised by

Dr. Daniel Montané Calaf

Dr. Sònia Abelló Cros



UNIVERSITAT ROVIRA I VIRGILI



Departament d'Enginyeria Química

Av. Països Catalans, 26

43007 Tarragona, Spain

I state that the present study, entitled “Catalytic conversion of syngas to alcohols and hydrocarbons over transition metal-based micro/mesoporous catalysts”, presented by Jordi Plana Pallejà for the award of the degree of Doctor, has been carried out under my supervision at the Department of Chemical Engineering of this university.

Tarragona, October 3<sup>rd</sup> 2018

Doctoral Thesis Supervisors



Dr. Daniel Montané Calaf



Dr. Sònia Abelló Cros

## Agraïments

S'acaba una etapa, i en comença una altra. Seria una injustícia no agrair el temps i l'esforç que m'han dedicat moltes persones durant tots aquest anys.

En primer lloc, els meus dos directors de tesi, el Daniel Montané i la Sònia Abelló. Sempre hi han estat quan els he necessitat, i sense els seus consells i ajut aquest camí hagués estat molt més difícil. Vull agrair-li especialment a la Sònia, que tantes coses m'ha ensenyat, i que tanta paciència ha tingut amb mi.

També agrair-li a la Carme Güell, que em va ensenyar la satisfacció que hi ha en el treball d'investigació, i que em va encaminar fins a acabar fent aquest doctorat. Per suposat, també m'agradaria agrair als companys d'IREC tots els moments que hem passat junts, i tot el temps i ajut que m'han dedicat sempre que els he necessitat: César Berrueco, Ester Clavero, Joan Salvadó, Ester Lorente, Francesc Valls... Espero que la vida us tracti tan bé com tots m'heu tractat a mi, us ho mereixeu.

Tampoc em puc oblidar dels treballadors del SRCiT, en especial la Rita Marimon i el Francesc Gispert. La vostra paciència i expertesa, i totes les coses que m'heu ensenyat, han estat imprescindibles per poder completar aquest treball. I també per suposat, el meus companys, els ja doctors Javier Recari i Monika Haponska. Gràcies per tots els moments que hem passat.

A l'Ana, i el Simba, que m'han acompanyat i cuidat sempre. M'heu animat en els moments més difícils, i m'heu ajudat a continuar quan pensava que no podia seguir.

A la meva mare, que tantes coses m'ha donat. M'ha ensenyat el valor de l'esforç i el treball honest, i sempre m'ha animat i estimat.

I al meu pare, l'home que espero poder ser algun dia. Vius en mi, i en tots els que t'estimem. Aquesta tesi és per tu.

Gràcies a tots,

Jordi



## Table of contents

<b>List of figures</b> .....	<b>VI</b>
<b>List of tables</b> .....	<b>X</b>
<b>Nomenclature</b> .....	<b>XI</b>
<b>Summary</b> .....	<b>XII</b>
<b>Chapter 1. Introduction</b> .....	<b>1</b>
1.1. Introduction .....	3
1.2. Fischer-Tropsch Synthesis (FTS) .....	3
1.3. Reaction mechanism of Fischer-Tropsch synthesis.....	4
1.4. Methanol Synthesis (MS).....	6
1.5. Reaction mechanism of methanol synthesis.....	6
1.6. Higher Alcohols Synthesis (HAS).....	6
1.7. Reaction mechanism of higher alcohols synthesis.....	7
1.8. HAS catalyst families.....	8
1.9. Catalyst supports .....	9
1.9.1. Zeolite support.....	9
1.9.2. Mesoporous silica .....	10
1.10. Bifunctional FTS catalysts .....	11
1.11. Supported HAS catalysts.....	13
1.12. Objectives and structure of the thesis .....	14
1.13. Bibliography.....	16

<b>Chapter 2. Experimental section .....</b>	<b>21</b>
2.1. Characterization techniques.....	23
2.1.1. Inductively Coupled Plasma-Optical Emission Spectroscopy.....	23
2.1.2. X-Ray Diffraction .....	24
2.1.3. N <sub>2</sub> Adsorption.....	25
2.1.4. Transmission Electron Microscopy .....	26
2.1.5. Diffuse Reflectance Fourier Transform Infrared Spectroscopy .....	26
2.1.6. H <sub>2</sub> -Temperature Programmed Reduction .....	26
2.2. Catalyst preparation .....	27
2.2.1. Fe/ZSM-5 catalysts.....	27
2.2.2. SBA-15/FeCoCu catalysts .....	28
2.3. Catalytic reaction system .....	29
2.3.1. FTS reaction system .....	29
2.3.2. HAS reaction system .....	32
2.4. Conversion, selectivity, and mass balance .....	32
2.5. Bibliography.....	34
<b>Chapter 3. Fischer-Tropsch Synthesis: Influence of zeolite acidity and mesoporosity .....</b>	<b>35</b>
3.1. Characterization of the catalysts.....	37
3.2. Fischer-Tropsch performance.....	45
3.2.1. Influence of Si/Al ratio of the untreated zeolite.....	45
3.2.2. Influence of mesoporosity .....	49
3.3. Bibliography.....	54

<b>Chapter 4. Higher Alcohol Synthesis: Effect of metal load and reaction conditions .....</b>	<b>55</b>
4.1. Catalyst composition: binary vs ternary catalysts .....	57
4.1.1. Characterization of fresh catalysts .....	57
4.1.2. Catalyst screening .....	62
4.1.3. Characterization of used catalysts .....	66
4.2. Ternary catalysts: effect of metal loading .....	67
4.2.1. Characterization of fresh catalysts .....	67
4.2.2. Catalyst activity .....	73
4.2.3. Characterization of the spent catalysts .....	79
4.3. FeCoCu 9/9/18: influence of reaction conditions and alkaline doping .....	81
4.3.1. Characterization of fresh catalysts .....	81
4.3.2. Influence of reaction conditions .....	84
Effect of temperature of reaction .....	84
Effect of contact time .....	89
Effect of H <sub>2</sub> /CO feed ratio .....	92
4.3.3. Alkaline doping .....	94
4.3.4. Characterization of spent catalysts .....	97
4.4. Bibliography .....	99
<b>Chapter 5. Concluding remarks .....</b>	<b>101</b>
5.1. Fischer-Tropsch Synthesis .....	103
5.2. Higher Alcohols Synthesis .....	104
5.3. Future work .....	106

## List of figures

<b>Figure 1.1.</b> Surface reactions of a) FTS, b) MS, and c) HAS. ....	5
<b>Figure 1.2.</b> ZSM-5 structure.....	11
<b>Figure 2.1.</b> Catalytic reaction system. ....	30
<b>Figure 2.2.</b> Contour plot of the analysis of the FTS liquid products by GCxGC/MS over the FeZ240-AT catalyst. Horizontal axis is retention time in the DB-5MS column (proportional to the carbon number of the product), while the vertical axis is retention time in the Innowax column (proportional to the polarity of the product).....	31
<b>Figure 3.1.</b> XRD patterns of the Fe-P precursor and the Fe catalyst (top), and MFI zeolites (bottom). ....	38
<b>Figure 3.2.</b> N <sub>2</sub> adsorption isotherms (left) and BJH adsorption pore size distributions (right) of the Fe catalyst and the native and treated zeolites.....	40
<b>Figure 3.3.</b> Transmission electron micrographs of the Fe catalyst and the native and treated zeolites.....	42
<b>Figure 3.4.</b> FTIR spectra in the OH-stretching region of the native and treated zeolites.....	44
<b>Figure 3.5.</b> CO conversion vs. time during FTS over the Fe catalyst and mixed with the different zeolites. Reaction conditions: H <sub>2</sub> /CO ratio = 2, T = 300°C, WHSV = 0.05 mol <sub>CO</sub> /(g <sub>cat</sub> ·h), and P = 10 bar. ....	46
<b>Figure 3.6.</b> FTS product mass distribution over the Fe catalyst. ....	47
<b>Figure 3.7.</b> FTS product mass distribution over the different Fe-based bifunctional catalysts.....	48
<b>Figure 3.8.</b> Mass selectivity towards paraffins, olefins or aromatics over the different bifunctional catalysts. In each carbon number group, left	

graph: FeZ40 (□), FeZ40-AT (Δ), FeZ40-AT-H (o); right graph: FeZ240 (□), FeZ240-AT (Δ), and FeZ240-AT-H (o)..... 53

**Figure 4.1.** TPR-H<sub>2</sub> profiles of catalysts. A: FeCoCu 0/9/9, B: FeCoCu 0/18/9, C: FeCoCu 0/9/18, D: FeCoCu 9/0/9, E: FeCoCu 18/0/9, F: FeCoCu 9/0/18, G; FeCoCu 9/9/0, H: FeCoCu 9/9/9. .... 59

**Figure 4.2.** XRD of calcined catalysts. A: FeCoCu 0/9/9, B: FeCoCu 0/18/9, C: FeCoCu 0/9/18, D: FeCoCu 9/0/9, E: FeCoCu 18/0/9, F: FeCoCu 9/0/18, G; FeCoCu 9/9/0, H: FeCoCu 9/9/9. □: Cu<sub>x</sub>Co<sub>3-x</sub>O<sub>4</sub>, ○: CuO. .... 60

**Figure 4.3.** TEM images of the binary and ternary catalysts. A: FeCoCu 9/0/9, B: FeCoCu 18/0/9, C: FeCoCu 9/0/18, D: FeCoCu 0/9/9, E: FeCoCu 0/18/9, F: FeCoCu 0/9/18, G; FeCoCu 9/9/0, H: FeCoCu 9/9/9. .... 61

**Figure 4.4.** Conversion and selectivity of binary and ternary catalysts after 24 h of reaction. Reaction conditions: 30 bar, 300°C, 0.3 molCO/gcat·h, H<sub>2</sub>/CO = 2..... 63

**Figure 4.5.** Selectivity towards hydrocarbons of the different catalysts..... 64

**Figure 4.6.** Selectivity towards alcohols of the different catalysts. .... 64

**Figure 4.7.** X-ray diffractograms of the used catalysts. A: FeCoCu 0/9/9, B: FeCoCu 0/18/9, C: FeCoCu 0/9/18, D: FeCoCu 9/0/9, E: FeCoCu 18/0/9, F: FeCoCu 9/0/18, G; FeCoCu 9/9/0, H: FeCoCu 9/9/9. □: CoFe, ○: Co, ●: Cu, ■: C..... 65

**Figure 4.8.** TEM images of used catalysts. A: FeCoCu 0/9/9-U, B: FeCoCu 9/0/9-U, C: FeCoCu 9/9/0-U, and D: FeCoCu 9/9/9-U. .... 66

**Figure 4.9.** XRD of activated catalysts. Crystalline phases: (□) Fe, (●) Cu, (○) Co..... 69

<b>Figure 4.10.</b> TEM images of the calcined catalysts. ....	70
<b>Figure 4.11.</b> Distribution of particle sizes of the metal aggregates present in the calcined catalysts. ....	71
<b>Figure 4.12.</b> H <sub>2</sub> temperature programmed reduction (TPR) profiles of the calcined materials. ....	72
<b>Figure 4.13.</b> Conversion and selectivity of ternary catalysts after 24 hours of reaction (30 bar, 300°C, WHSV = 0.3 mol <sub>CO</sub> /g <sub>cat</sub> ·h, H <sub>2</sub> /CO = 2). ....	74
<b>Figure 4.14.</b> Comparison of ASF plots of the ternary catalysts after 24 hours of reaction (Same conditions than Figure 4.13. Hydrocarbons, □; Alcohols, ○). ....	77
<b>Figure 4.15.</b> Diffractograms of the spent catalysts. Crystalline phases: (□) Fe, (●) Cu, (○) Fe <sub>5</sub> C <sub>2</sub> . ....	78
<b>Figure 4.16.</b> TEM images of the spent catalysts. ....	80
<b>Figure 4.17.</b> Pore size distribution of SBA-15 9/9/18. ....	81
<b>Figure 4.18.</b> XRD of calcined catalysts. Crystalline phases: (□) Fe, (●) Cu. ....	82
<b>Figure 4.19.</b> TEM imaging of (A) fresh SBA-15 9/9/18, (B) fresh SBA-15 9/9/18-Na, (C) fresh SBA-15 9/9/18-K, (D) used SBA-15 9/9/18 after 96 h of reaction at 360°C, (E) used SBA-15 9/9/18-Na after 24 h of reaction at 300°C, (F) used SBA-15 9/9/18-K after 24 h of reaction at 360°C. ....	83
<b>Figure 4.20.</b> Conversion and selectivity at different temperatures at 24, 48, 72, and 96 h of reaction. Top: 300°C, middle: 330°C, bottom: 360°C. ....	85
<b>Figure 4.21.</b> Chain propagation probability for hydrocarbons and alcohols at different temperatures of reaction. Top graph:	

hydrocarbons. Bottom graph: alcohols. Black: 24h; Red: 48h; Blue: 72h; Magenta: 96h. Square: 300°C; Circle: 330°C; Triangle: 360°C. .... 86

**Figure 4.22.** Conversion, selectivity, and chain growth probability at different contact times. Top graph: conversion and selectivity; middle graph: hydrocarbon chain growth probability; bottom graph: alcohol chain growth probability. .... 90

**Figure 4.23.** Conversion, selectivity, and chain growth probability at different gas ratios. Top graph: conversion and selectivity; middle graph: hydrocarbon chain growth probability; bottom graph: alcohol chain growth probability. .... 91

**Figure 4.24.** Effects of alkaline doping in conversion, selectivity, and chain growth probability. Top graph: conversion and selectivity; middle graph: hydrocarbon chain growth probability; bottom graph: alcohol chain growth probability. .... 95

**Figure 4.25.** Effects of temperature in K-doped catalysts in conversion, selectivity, and chain growth probability. Top graph: conversion and selectivity; middle graph: hydrocarbon chain growth probability; bottom graph: alcohol chain growth probability. .... 96

**Figure 4.26.** XRD of used catalysts. Crystalline phases: (□) Fe, (●) Cu. .... 98

## List of tables

<b>Table 3.1:</b> Chemical composition and textural properties of the FTS catalyst and the commercial and alkaline-treated zeolites. ....	39
<b>Table 3.2:</b> Mass selectivity and olefin to paraffin ratio of the Fe catalyst alone and mixed with commercial and alkaline-treated zeolites. ....	45
<b>Table 4.1.</b> Metallic charge of the catalysts.....	58
<b>Table 4.2.</b> Textural properties of the binary and ternary catalysts. ....	59
<b>Table 4.3.</b> Textural properties, metallic load, and H <sub>2</sub> consumption of the calcined FeCoCu catalysts and SBA-15. ....	68
<b>Table 4.4.</b> Selectivity (S <sub>j</sub> ) to alcohols and hydrocarbons by carbon number .....	76
<b>Table 4.5.</b> Selectivity towards hydrocarbons and alcohols at different temperatures.....	87
<b>Table 4.6.</b> Selectivity towards hydrocarbons and alcohols at different gas ratios.....	93

## Nomenclature

AC	Activated Carbon
ASF	Anderson-Schulz-Flory
BET	Brunauer-Emmett-Teller
BJH	Barret-Joyner-Halenda
CNT	Carbon nanotube
DME	Dimethyl ether
DRIFTS	Diffuse Reflectance Fourier Transform Infrared Spectroscopy
H <sub>2</sub> -TPR	H <sub>2</sub> -Temperature programmed reduction
HAS	Higher alcohols synthesis
FID	Flame ionization detector
FTS	Fischer-Tropsch synthesis
FWHM	Full width at half maximum
GC	Gas chromatograph
GCxGC/MS	Two-dimensional GCxGC system coupled to a mass spectrometer
GTL	Gas-to-liquid
ICP-OES	Inductively coupled plasma-optical emission spectroscopy
TEM	Transmission electron microscopy
XRD	X-ray diffraction
ZSM	Zeolite Socony Mobil

## Summary

Due to the rising concerns regarding global warming and climate change, new laws and regulations have been proposed in the European Union to promote the development of clean energy technologies, in order to reduce the dependency on fossil fuels.

Synthesis gas (syngas) can be obtained from the gasification of biomass. This mixture of carbon monoxide and hydrogen offers great versatility, and several reaction processes can be used to obtain a variety of liquid fuels and oxygenated products.

Fischer-Tropsch Synthesis (FTS) is the most extensively used process for the synthesis of linear hydrocarbons from syngas. Lighter products can be used as diesel fuel, and heavier ones can be used as waxes. The most commonly used metals for FTS are Iron and Cobalt. Iron offers high levels of conversion, and the capacity to alter the  $H_2/CO$  ratio of the syngas feed. Cobalt has improved selectivity towards long chain paraffins, and low selectivity towards oxygenated products.

Higher Alcohols Synthesis (HAS) is a reaction process to obtain alcohols containing two or more carbon atoms. These alcohols can be used as intermediates for the synthesis of lubricants, detergents and cosmetics. This process uses a combination of FTS catalysts and methanol synthesis (MS) catalysts (mainly Copper and Chromium), as it involves a combination of both reaction mechanisms (FTS and MS). Common HAS catalysts usually contain a combination of Iron, Cobalt, Chromium and Copper, in order to have both active sites required for the synthesis of higher alcohols.

The objective of this thesis is the study of CO hydrogenation using different types of supported catalysts to obtain fuel-range hydrocarbons via FTS, or to produce higher alcohols via HAS. These experiments were performed in a laboratory-scale reactor, and the catalysts and reaction products were characterized using a variety of techniques.

The first block of the thesis studies the effect of zeolite acidity and mesoporosity in FeCuMgK catalysts supported on ZSM-40 and ZSM-240.

The results show that zeolite acidity is responsible for the cracking of heavy hydrocarbons and the formation of aromatic products through oligomerization, cyclization and dehydrogenation of primary short olefins. The Si/Al ratio induced changes in the composition of the aromatic products, with increased acidity resulting in increased complexity of aromatic products. The formation of mesoporosity resulted in a slight increase in C<sub>2</sub>-C<sub>4</sub> paraffins due to an improved access to the acidic sites through the mesopores, due to the overcracking of heavier molecules. The defining factor towards improved gasoline-range products was acidity, with higher Si/Al ratios offering the best selectivity, with mesoporosity having little to no influence.

The second block evaluates the influence of metal loading on binary and ternary FeCoCu catalysts supported on mesoporous silica SBA-15 for the production of higher alcohols. The results pointed out that ternary catalysts offered improved selectivity towards higher alcohols without compromising CO conversion values. Further analysis of different ternary catalysts showed that catalyst FeCoCu 9/9/18 had the best selectivity towards higher alcohols, with the best chain growth probability towards them. The final part evaluated several reaction conditions, and it was found that moderate temperatures were key to facilitate alcohol selectivity. High contact times and stoichiometric ratios of syngas feed were also beneficial towards alcohols selectivity. Alkaline doping showed an improvement of selectivity towards higher alcohols, but reduced overall CO conversion.

# Chapter 1

## Introduction

UNIVERSITAT ROVIRA I VIRGILI

CATALYTIC CONVERSION OF SYNGAS TO ALCOHOLS AND HYDROCARBONS OVER TRANSITION METAL-BASED  
MICRO/MESOPOROUS CATALYSTS

Jordi Plana Pallejà

## 1.1. Introduction

Nowadays, rising concerns about climate change and global warming are inducing changes in environmental laws, exhorting the use of renewable energy sources, as well as a decrease in the dependency on fossil fuels [1].

Among the many renewable energy sources (solar, wind, geothermal) the use of biomass as a font of energy is showing an increased interest, due to the possibility of transforming it to synthesis gas (syngas), a mixture of carbon monoxide and hydrogen using a process of gasification.

Biomass is usually obtained from byproducts or waste products of other processes, such as crop cultivation (switchgrass, straw), and livestock production (animal waste).

Due to its biogenic origin biomass is usually considered to be neutral concerning CO<sub>2</sub> emissions, since photosynthesis fixes atmospheric carbon dioxide. However, biomass is also considered as a resource with low energetic density and unstable availability due to its dependence on seasonal farming.

Syngas obtained from biomass can be purified and used as building blocks for reactions of synthesis of liquid fuels. Chief among these reactions are Fischer-Tropsch synthesis, for the production of hydrocarbons in the gasoline or diesel range, and higher alcohols synthesis, to produce higher alcohols (ethanol and heavier).

## 1.2. Fischer-Tropsch Synthesis (FTS)

Fischer-Tropsch synthesis was discovered by Franz Fischer and Hans Tropsch in 1925 [2]. Since then, it has been used extensively for the production of hydrocarbons throughout the world. This process renders mostly linear hydrocarbons, which can be used as diesel fuel, as well as heavier products, such

as waxes [3]. Since its discovery, a great number of papers and patents have been published [4,5].

The two metals commonly used for FTS catalysts are Fe and Co, since they provide the best process economics [6]. Cobalt has shown an improved synthesis of long-chain linear hydrocarbons, whereas Fe offers higher levels of conversion as well as the capacity to alter the  $H_2/CO$  ratio of the syngas via the Water-Gas-Shift (WGS) reaction.

Cobalt-based catalysts are used at low temperatures of reaction in order to avoid excessive methane selectivity. They usually produce long chain paraffins, with low selectivity towards oxygenate products due to its high hydrogenation capacity [7,8]. Iron is more advantageous to produce other types of hydrocarbons, such as olefins and aromatic products. It also has higher selectivity towards branched hydrocarbons. These properties can be adjusted with the use of various promoters, which can alter the distribution of products obtained [9,10].

### 1.3. Reaction mechanism of Fischer-Tropsch synthesis

FTS is a surface polymerisation reaction (Fig. 1.1a), and even if the exact mechanism of reaction is not clear, there are two mechanisms of reaction which are mostly accepted: the carbide reaction scheme, where CO is dissociated and hydrogenated to alkyl monomers, which can be further coupled to form heavier hydrocarbons; and the CO insertion mechanism, where CO is not dissociated and, instead, a series of hydrogenation, CO insertion and dehydration steps are involved in chain propagation [11]. Both processes involve a reaction initiation, followed by one or more chain propagation steps, and chain termination.

The carbide mechanism reaction initiation comprises a CO dissociation, with the corresponding formation of  $CH_x$  species. These species can combine to increase the chain length, and the hydrogenation of the chain leads to its

termination, and the formation of the final product. The formation of oxygenated products stems from the insertion of CO into a growing chain, which leads to the chain termination [12].

The CO insertion mechanism involves the initial hydrogenation of a CO monomer, followed by its dehydration to form the alkyl monomer. Chain propagation involves a series of steps of CO insertion, CO hydrogenation, and CO dehydration to continue the chain growth. Chain termination involves a hydrogenation step after the dehydration. In this mechanism, the formation of oxygenates involves a hydrogenation process after CO insertion and before its dehydration [13].

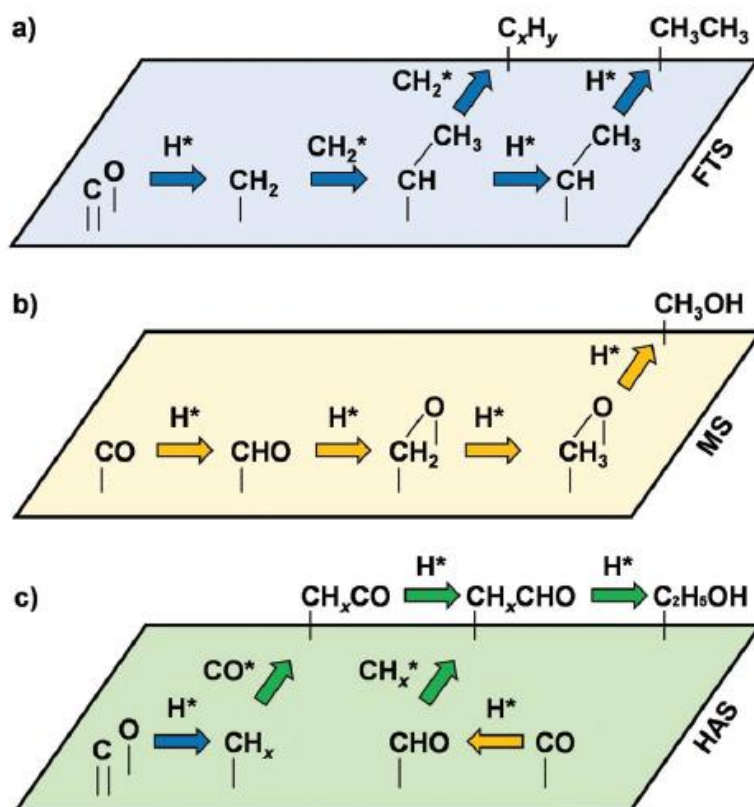


Figure 1.1. Surface reactions of a) FTS, b) MS, and c) HAS [14].

## 1.4. Methanol Synthesis (MS)

Methanol synthesis from syngas was developed by BASF researchers Alwin Mittasch and Mathias Pier [15]. Due to the extreme conditions necessary for their Cr/MnO catalyst to work (220 bar and 450°C), it was not until 1963 when a new catalyst was patented by Forster Snowdon Frederick and Phineas Davies. [16] This Cu-ZnO-Al<sub>2</sub>O<sub>3</sub> catalyst, that could be used in lower reaction conditions (50-100 bar, and 220-300°C), sparked interest in the process, and was extensively studied and optimised. Despite this, the exact mechanism of reaction is not yet understood completely.

## 1.5. Reaction mechanism of methanol synthesis

MS is also a surface polymerisation reaction (Fig. 1.1b), where CO is hydrogenated to CHO and subsequently to methanol. However, it has also been considered that CO<sub>2</sub> obtained from Water-Gas Shift (WGS) reaction might be the main carbon source due to its faster rate of hydrogenation [17]. This mechanism involves the initial oxidation of CO to CO<sub>2</sub> via the WGS reaction, followed by additional hydrogenation steps until the formation of a formate monomer, which is further hydrogenated to a methoxy monomer. A final hydrogenation yields the final product, methanol [18].

## 1.6. Higher Alcohols Synthesis (HAS)

Higher alcohols are usually defined as alcohols containing two or more carbon atoms. They are considered as valuable products due to their wide range of industrial uses. They are intermediate products for the synthesis of lubricants, detergents and cosmetics, among other high-value products [19-22]. Another application of significant importance is their use as additives for gasoline in order to increase the combustion efficiency and raise the octane number [23,24]. Ethanol and isobutanol are seen as future replacements of methyl tert-butyl ether (MTBE) due to the environmental issues of the latter. Another potential

use for ethanol is that of a hydrogen carrier as a safer, more energy-dense alternative to methanol in fuel cells [25].

Currently, the fermentation of sugars is the most widely used method for the production of ethanol and isobutanol [26,27], while heavier alcohols are obtained by the hydration of alkenes obtained from the petrochemical industry [28]. Both processes have important drawbacks: the first process uses several distillation steps, with the required energetic demand, and the second has very low conversion (ca. 5%) per pass.

Syngas has been considered as a precursor for higher alcohol synthesis (HAS) since the 1930s, using a combination of FTS catalysts and methanol synthesis (MS) catalysts to combine carbon chain growth and carbon monoxide hydrogenation capabilities. This research has been heavily related to oil prices, with the last decade showing an increasing number of publications. Despite this increased interest in HAS from syngas, the advances achieved are not enough to warrant full-scale industrial implementation, with few pilot plants built around the world, and a total annual capacity of 12 kt [29].

## **1.7. Reaction mechanism of higher alcohols synthesis**

HAS involves the conversion of CO to ethanol or heavier alcohols (Fig 1.1c). It shows similarities with FTS and MS, and their products usually appear as by-products in FTS and MS. In this reaction the adsorbed CO can experience two types of O dissociation: unassisted or via hydrogenation. In the first case a lone C is obtained, which is then hydrogenated to obtain an alkyl group. In the second case, a formyl group is obtained, and a further hydrogenation leads to the formation of another alkyl group. CO or formyl is then inserted into the alkyl group to obtain an oxygenate product, which can be hydrogenated to terminate the chain, or additional alkyl groups can be integrated into the chain to obtain heavier products, which will then be hydrogenated.

## 1.8. HAS catalyst families

Heterogeneous catalysts for the production of HA are typically classified in four categories: Rh-based, Mo-based, modified FTS and modified MS catalysts.

Rh-based catalysts for the conversion of syngas to HA were developed by Union Carbide Corporation in the 1980s [30] using catalysts supported on  $\text{SiO}_2$  and alkaline metals. However, in order to obtain improved selectivity towards oxygenate products and decrease selectivity towards hydrocarbons, doping with alkali or transition metals is required [31,32].

Mo-based catalysts comprise  $\text{MoS}_2$ , MoP,  $\text{MoO}_x$ , and  $\text{Mo}_2\text{C}$ . The first patents for  $\text{MoS}_2$  catalysts for HA were developed by Dow in the 1980s [33,34], and are the most widely used Mo-based catalysts. Like Rh-based catalysts, the addition of promoters has profound influence in the range of products obtained. In addition to that, the nature of the catalyst support has a noticeable effect in the catalytic performance [35-37].

Modified MS catalysts have been extensively researched since the 1930s, when it was discovered that alkaline impurities in MS catalysts favored the formation of heavy oxygenates during methanol synthesis [38]. Currently there are two major types of modified MS catalysts: high-temperature Cr-based catalysts, and low-temperature Cu-based catalysts. Cr-based catalysts have long catalyst life, but show high HC selectivity, and are not as studied as Cu-based catalysts, which have been found to be some of the most active systems for the formation of branched alcohols. These catalysts, promoted with Co, show an increase in higher alcohol selectivity, specially ethanol [39,40]. The doping effect of alkaline metals (specially Cs), as well as the use of Zn- and Zr-based supports ( $\text{ZnO}$  and  $\text{ZrO}_2$ ) have been found to greatly improve selectivity towards higher alcohols [41-43].

Modified FTS catalysts have been proposed as HAS catalysts since the late 1970s, using catalysts containing Co and Cu. It was found that Co favored CO dissociation and Cu enabled CO adsorption and insertion, as predicted by the dual site model for HAS [44]. Research on Fe-based catalysts began around the same time but were not widely studied until the beginning of the 2000s, where Fe was used as a promoter for Cu-based systems. Similarly to Co, Fe is considered to promote the dissociative adsorption of CO as well as to offer a carbon chain growth site, which in combination with Cu contained the two active sites required for HAS. Doping with alkaline metals is commonly used to improve the catalytic yield towards higher alcohols [45,46]. Many types of supports have been found to improve CO conversion and selectivity towards HA upon alkali doping [47-49].

## **1.9. Catalyst supports**

The use of an adequate support material offers advantages in terms of performance and durability of FTS catalysts. The synthesis of a supported catalyst offers structural advantages, such as a dispersion of the active metals, increased stability, and improved thermal diffusion. Regarding catalytic performance, the effects of the support can be significant, producing changes in CO conversion and selectivity towards hydrocarbons. These effects are due to changes in porosity, acidity, support-active metal interactions, and changes in the distribution of the metal particles [50,51]. The most common supports for FTS catalysts are silica, alumina, titania, magnesia, zirconia, and zeolites [52-55].

### **1.9.1. Zeolite supports**

Zeolites belong to the crystalline aluminosilicate family, and exhibit many beneficial properties, such as high surface area, intrinsic acidity, well-defined microporosity and high hydrothermal stability. Their porous structure also allows the confinement of metal particles in their interior. There are also many different types of zeolites, with varying structures and pore sizes [56]. These

properties make them good supports for improved CO hydrogenation towards specific ranges of products. The combination of acidity and specific pore sizes favors selectivity towards molecules smaller than the volume of the pore channel [57]. This enables shifting of the product range to paraffins, olefins, or aromatics due to the additional effect of the acidic sites [58]. Acidic sites can enable secondary reactions of isomerization, aromatization or cracking. Increased acidity results in higher activity of secondary cracking reactions, which reduce the amounts of heavier hydrocarbons. High acidity also destabilizes long aliphatic molecules, which are cracked into lighter olefins and paraffins. [59,60] Despite these properties, zeolites have several disadvantages, the most important related to the limitations to molecular transport inside the porous structure, as well as the eventual migration of active metals to the external surface of the particles where pore size restriction effects do not exist [61].

Some of the most active supports in FTS are ZSM zeolites, especially ZSM-5 and ZSM-12, which were found to be supports highly active for secondary hydrocarbon conversion reactions in iron-containing catalysts. [62] Those zeolites have a 3-dimensional MFI pore structure, with elliptical straight channels and circular zig-zag channels [56].

### **1.9.2. Mesoporous silica**

Mesoporous silicas have many properties that make them interesting materials in the fields of nanotechnology and biomedicine [63,64]. They have highly ordered pore structures and very high surface areas, due to the nanotemplating applied during their synthesis. One of the most known types of mesoporous silicas is the Santa Barbara Amorphous (SBA-15) [65]. This silica has large pore sizes (50 to 300 Angstrom) and unidimensional hexagonal pores. These properties make SBA-15 an advantageous material to use as a support for metallic catalysts. The ordered channel structure can confine the active metal particles and it can also restrict the access of heavier molecules.

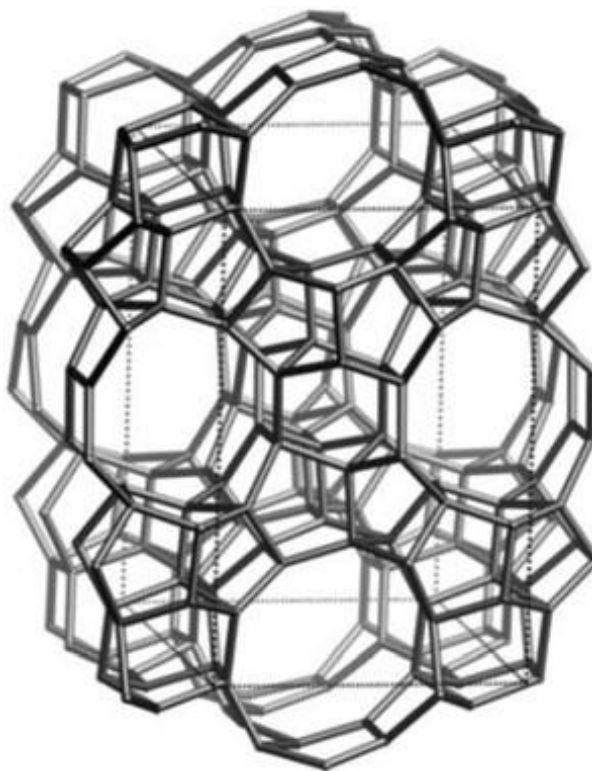


*Figure 1.2. ZSM-5 structure. Obtained from [57].*

### **1.10. Bifunctional FTS catalysts**

A common approach to drive the products towards hydrocarbons in the gasoline or diesel ranges has been to use multifunctional catalysts [66-68]. These materials contain different types of active sites (acidic, metallic, etc.) with complementary functionalities. In the case of FTS, the use of acidic co-catalysts has been a sound choice since it narrows the distribution of products into the gasoline/diesel range by combining reactions of hydrocracking, olefin oligomerization, alkylation, branching and aromatization [69].

Many examples of this approach are available in recent literature, dealing

with the use of a FTS metal catalyst combined with zeolites [70-75]. A common outcome of these studies has been to establish the importance of zeolite porosity and acidity in the performance of such multifunctional catalysts. The Brønsted acidity of the zeolite, due to the presence of Al in its structure, promotes secondary reactions, and therefore the formation of lighter hydrocarbons, both aromatic and branched [76].

Concerning pore structure, it may restrict the chain-growth process thus yielding lighter products, depending on the type of zeolite. Bessell found that cobalt supported on zeolite Y, mordenite and ZSM-5 gave active FTS catalysts, and that the acidity of the support determined the nature of the higher hydrocarbons being produced; the most acidic ZSM-5 supported catalyst produced branched products, while the mordenite channel system was responsible for linear-products [77]. The same author found that product selectivity was governed by the accessibility to the acidic sites within the pore structure rather than the overall acid strength when Co was supported in ZSM-5, ZSM-11, ZSM-12 or ZSM-34 [78]. Botes and Böhringer discovered that a catalyst containing iron and a highly acidic ZSM-5 zeolite (Si/Al ratio of 15) had a higher activity and selectivity towards aromatics and light paraffins, but a faster deactivation than a lower acidity zeolite (Si/Al ratio of 140) [59]. Martínez and López reasserted these findings using a FeCoK catalyst physically mixed with ZSM-5 [58].

Both aspects, pore structure and acidity, seem to be intimately related in FTS. However, the presence of micropores in zeolites often imposes strong diffusion limitations since it restricts the access to the active sites, and therefore it may limit the activity, selectivity and useful lifetime of the catalyst [79]. To overcome this issue, several studies on the effects of mesoporosity generation have been recently published for FTS catalysts based on cobalt/zeolite systems [80-83]. The use of these hierarchical zeolites produced an increase in CO conversion and selectivity towards C<sub>5</sub>-C<sub>11</sub> compared to the untreated zeolites, due to the

optimized hydrocracking and isomerization reactions occurring inside the newly-formed mesopores.

### **1.11. Supported HAS catalysts**

The use of supporting materials to improve HAS catalysts has sparked interest as a way to modify the characteristics of the active metals, and a wide variety of materials have been used by different research groups over the world.

Work from Zhang et al. [84,85] studied the effect of various types of carbon nanotubes (CNT) on CoCu catalysts and found that their presence improved selectivity towards butanol and DME, while keeping good levels of conversion. The improved capability of CNTs to adsorb H<sub>2</sub> was key to achieve increased levels of conversion and selectivity towards alcohols. Pei et al. [86,87] used alumina and silica supports on Co/AC catalysts, with alumina supported catalysts achieving moderate improvements on CO conversion and alcohols selectivity over unsupported catalysts. Silica supported catalysts showed similar improvements on alcohols selectivity, with a decrease in CO conversion values. An investigation performed by Wang et al. [88] compared alumina, silica and CNT supports on CoCu catalysts, and also showed alumina as the most favoring support for improved alcohols selectivity, with all three supports showing similar levels of CO conversion. A work by Lee et al. [89] used magnesia, alumina and zirconia as supports for CoCu catalysts, with zirconia achieving the highest CO conversion, with a low selectivity towards higher alcohols. The use of AC was also tested by Pei et al. [45], using a CoCuMn catalyst, obtaining the best results of CO conversion and HA selectivity with equal amounts of all three elements. A work from Liu et al. [90,91] involved the formation of bimetallic core-shell nanoparticles using silica and zirconia as supports, with catalysts having more exposed Cu sites having improved conversion and selectivity towards alcohols. A study from Yeon et al. [92] studied the effect of titania and AC on Cu-based catalysts, with titania having increased selectivity towards liquid products (oxygenated and hydrocarbons), and AC showing improved selectivity towards

ethanol. These studies show an ongoing search for improved supports to use along HAS catalysts.

## 1.12. Objectives and structure of the thesis

The main goal of this work is the study of CO hydrogenation using different types of supported catalysts to obtain fuel-range hydrocarbons via FTS, or to produce higher alcohols via HAS. Therefore the thesis has two specific objectives:

- Study the effect of zeolite acidity and mesoporosity in FeCuMgK catalysts supported on ZSM-40 and ZSM-240. Evaluate the effect on CO conversion and selectivity towards hydrocarbons, and improvements on selectivity towards fuel-range hydrocarbons.
- Evaluate the influence of metal loading on binary and ternary FeCoCu catalysts supported on mesoporous silica SBA-15 for the production of higher alcohols. Understand the effect of the different active metals, the best ratio between metals, and the best reaction conditions for the production of higher alcohols.

This dissertation is divided in 5 chapters:

- Chapter 1 provides a brief background and the motivation for this thesis.
- The second chapter presents the characterization techniques as well as the reaction systems used in the following chapters.
- The third chapter covers the study of the effect of zeolite acidity and mesoporosity on CO conversion and selectivity towards fuel-range hydrocarbons.
- The fourth chapter is divided in three parts. The first part studies the effect of each metal on conversion and selectivity towards alcohols. The

second part seeks the best metal ratio of Fe, Co, and Cu for the production of higher alcohols. The third and final part analyses the effects of varying reaction conditions on conversion and selectivity towards higher alcohols, using the best catalyst from part 2. Alkaline doping is also studied.

- The fifth chapter summarizes the conclusions obtained in this work and briefly outlines possible future work in this field.

### 1.13. Bibliography

- [1] European Commission. Energy Strategy and Energy Union <https://ec.europa.eu/energy/en/topics/energy-strategy-and-energy-union> (last accessed August 31, 2018).
- [2] F. Fischer, H. Tropsch (1925) DE-484337.
- [3] M. E. Dry, *J. Chem. Technol. Biotechnol.* 77 (2002) 43-50.
- [4] R. Oukaci, A. H. Singleton, J. G. Goodwin Jr., *Appl. Catal. A: Gen.* 186 (1999) 129-144.
- [5] R. L. Espinoza, A. P. Raje, D. Jack (ConocoPhillips Co) (2005) US-6897246 B2.
- [6] F. Diehl, A. Y. Khodakov, *Oil Gas Sci. Technol.* 64 (2009) 11-24.
- [7] A. Y. Khodakov, W. Chu, P. Fongarland, *Chem. Rev.* 107 (2007) 1692-1744.
- [8] S. Li, S. Krishnamoorthy, A. Li, G. D. Meitzner, E. Iglesia, *J. Catal.* 206 (2002) 202-217.
- [9] S. Li, A. Li, S. Krishnamoorthy, E. Iglesia, *Catal. Lett.* 77 (2001) 197-205.
- [10] F. E. M. Farias, F. G. Sales, F. A. N. Fernandes, *J. Nat. Gas Chem.* 17 (2008) 175-178.
- [11] R. A. van Santen, A. J. Markvoort, I. A. W. Filot, M. Ghouri, E. J. M. Hensen, *Phys. Chem. Chem. Phys.* 15 (2013) 17038–17063.
- [12] E. De Smit, B. M. Weckhuysen, *Chem. Soc. Rev.* 37 (2008) 2758-2781.
- [13] M. Zhuo, K. F. Tan, A. Borgna, M. Saeys, *J. Phys. Chem. C* 113 (2009) 8357-8365.
- [14] H. T. Luk, C. Mondelli, D. Curulla Ferré, J. A. Stewart, J. Pérez-Ramírez, *Chem. Soc. Rev.* 46 (2017) 1358-1426.
- [15] A. Mittasge, M. Pier (1926) US-1569775.
- [16] P. Davies, F. Snowdon (1963) US-3326956.
- [17] O. Martin, J. Pérez-Ramírez, *Catal. Sci. Technol.* 3 (2013) 3343-3352.
- [18] L. C. Grabow, M. Mavrikakis, *ACS Catal.* 1 (2011) 365-384.
- [19] P. Forzatti, E. Tronconi, I. Pasquon, *Catal. Rev.: Sci. Eng.* 33 (1991) 109-168.
- [20] K. Fang, D. Li, M. Lin, M. Xiang, W. Wei, Y. Sun, *Catal. Today* 147 (2009) 133-138.
- [21] A. Morschbacker, *J. Macromol. Sci., Polym. Rev.* 49 (2009) 79-84.

- [22] C. Angelici, B. M. Weckhuysen, P. C. A. Bruijninx, *ChemSusChem* 6 (2013) 1595–1614.
- [23] V. M. Thomas, A. Kwong, *Energy Policy* 29 (2001) 1133-1143.
- [24] L. Siwale, L. Kristo'f, T. Adam, A. Bereczky, A. Penninger, M. Mbarawa, K. Andrei, *J. Power Energy* 1 (2013) 77-83.
- [25] C. Lamy, S. Rousseau, E. M. Belgsir, C. Coutanceau, J.-M. Le'ger, *Electrochim. Acta* 49 (2004) 3901-3908.
- [26] M. Devarapalli, H. K. Atiyeh, *Biofuel Res. J.* 7 (2015) 268-280.
- [27] F. W. Bai, W. A. Anderson, M. Moo-Young, *Biotechnol. Adv.* 26 (2008) 89-105.
- [28] Y. Nakagawa, N. Tajima, K. Hirao, *J. Comput. Chem.* 21 (2000) 1292-1304.
- [29] Nexant Inc., Report: NREL/SR-510-39947,  
<http://www.nrel.gov/docs/fy06osti/39947.pdf> (last accessed August 31, 2018).
- [30] P. Ellgen, M. Bhasin (1976) US-4096164.
- [31] J. Yu, D. Mao, L. Han, Q. Guo, G. Lu, *J. Ind. Eng. Chem.* 19 (2013) 806-812.
- [32] W. Mao, J. Su, Z. Zhang, X. Xu, W. Dai, D. Fu, J. Xu, X. Zhou, Y. Han, *Chem. Eng. Sci.* 135 (2015) 312-322.
- [33] R. Stevens (1986) US-4752622.
- [34] R. Stevens, M. Conway (1986) US-4752623.
- [35] Y. Liu, K. Murata, M. Inaba, *React. Kinet., Mech. Catal.* 113 (2014) 187-200.
- [36] P. E. Boahene, V. R. Surisetty, R. Sammynaiken, A. K. Dalai, *Top. Catal.* 57 (2014) 538–549.
- [37] M. Xiang, D. Li, W. Li, B. Zhong, Y. Sun, *Catal. Commun.* 8 (2007) 88-90.
- [38] K. J. Smith, R. Anderson, *Can. J. Chem. Eng.* 61 (1983) 40–45.
- [39] J. Anton, J. Nebel, H. Song, C. Froese, P. Weide, H. Ruland, M. Muhler, S. Kaluza, *Appl. Catal., A* 505 (2015) 326-333.
- [40] J. Schro, U. Arnold, J. Abeln, M. Do, *Chem. Eng. Technol.* 87 (2015) 1760-1770.
- [41] Y. Liu, K. Murata, M. Inaba, I. Takahara, K. Okabe, *J. Jpn. Pet. Inst.* 53 (2010) 153-159.
- [42] R. Xu, W. Wei, W. Li, T. Hu, Y. Sun, *J. Mol. Catal. A: Chem.* 234 (2005) 75-83.

- [43] Y. Wu, H. Xie, S. Tian, N. Tsubaki, Y. Han, Y. Tan, *J. Mol. Catal. A: Chem.* 396 (2015) 254–260.
- [44] J. J. Spivey, A. Egbebi, *Chem. Soc. Rev.* 36 (2007) 1514–1528.
- [45] Y. Pei, S. Jian, Y. Chen, C. Wang, *RSC Adv.* 5 (2015) 76330-76336.
- [46] W. Gao, Y. Zhao, J. Liu, Q. Huang, S. He, C. Li, J. Zhao, M. Wei, *Catal. Sci. Technol.* 3 (2013) 1324-1332.
- [47] A. Cao, G. Liu, L. Wang, J. Liu, Y. Yue, L. Zhang, Y. Liu, *J. Mater. Sci.* 51 (2016) 5216-5231.
- [48] R. Khalid Karim, R. Asad Khan (2014) US-2014/0142206 A1.
- [49] T. Niu, G. L. Liu, Y. Chen, J. Yang, J. Wu, Y. Cao, Y. Liu, *Appl. Surf. Sci.* 364 (2016) 388-399.
- [50] Q. Zhang, J. Kang, Y. Wang, *ChemCatChem* 2 (2010) 1030-1058.
- [51] H. Dong, M. Xie, J. Xu, M. Li, L. Peng, X. Guo, W. Ding, *Chem. Commun.* 47 (2011) 4019-4021.
- [52] F. G. Dwyer, W. E. Garwood (Mobil Oil Corp) (1984) US-4463101 A.
- [53] M. J. Desmond, M. A. Pepera (Standard Oil Co Ohio) (1985) EP-154063 A1.
- [54] J. A. Rabo, P. K. Coughlin (Union Carbide Corp) (1987) US-4652538 A.
- [55] Y. Zamani, A. N. Pour, K. J. Jozani, J. Y. Mehr (Research Institute of Petroleum Industry) (2006) EP-1657290 A1.
- [56] C. Baerlocher, L. B. McCusker, D. H. Olson (2007) *Atlas of Zeolite Framework Types*, 6th. Ed., Elsevier, Amsterdam.
- [57] L. Gucci, I. Kiricsi, *Appl. Catal. A: Gen.* 186 (1999) 375-394.
- [58] A. Martínez, C. López, *Appl. Catal. A: Gen.* 294 (2005) 251-259.
- [59] F. G. Botes, W. Böhringer, *Appl. Catal. A: Gen.* 267 (2004) 217-225.
- [60] M. R. Goldwasser, F. Navas, M. J. Pérez Zurita, M. L. Cubeiro, E. Lujano, C. Franco, F. González Jiménez, E. Jaimes, D. Moronta, *Appl. Catal. A: Gen.* 100 (1993) 85-95.
- [61] N. G. Gallegos, A. M. Alvarez, M. V. Cagnoli, J. F. Bengoa, L. A. Cano, R. C. Mercader, S. G. Marchetti, *Catal. Today* 107-108 (2005) 355-361.
- [62] L. A. Vytnova, E. I. Bogolepova, A. N. Shuikin, V. I. Kurkin, E. V. Marchevskaya, G. A. Kliger, *Pet. Chem.* 46 (2006) 324-331.

- [63] G. Valenti, R. Rampazzo, S. Bonacchi, L. Petrizza, M. Marcaccio, M. Montalti, L. Prodi, F. Paolucci, *J. Am. Chem. Soc.* 138 (2016) 15935-15942.
- [64] R.-A. Mitran, D. Berger, C. Munteanu, C. Matei, *J. Phys. Chem. C* 119 (2015) 15177-15184.
- [65] D. Zhao, J. Feng, Q. Huo, N. Melosh, G.H. Fredrickson, B.F. Chmelka, G.D. Stucky, *Science*. 279 (1998) 548-552.
- [66] N. Tsubaki, Y. Yoneyama, K. Michiki, K. Fujimoto, *Catal. Commun.* 4 (2003) 108-111.
- [67] X.H. Li, M.F. Luo, K. Asami, *Catal. Today* 89 (2004) 439-446.
- [68] A. Martínez, J. Rollán, M.A. Arribas, H.S. Cerqueira, A.F. Costa, E.F. S.-Aguiar, *J. Catal.* 249 (2007) 162-173.
- [69] T. Degnan, Jr., *Top. Catal.* 13 (2000) 349-356.
- [70] H. Jahangiri, J. Bennett, P. Mahjoubi, K. Wilson, S. Gu, *Catal. Sci. Technol.* 4 (2014) 2210-2229.
- [71] N. Shimoda, K. Faungnawakij, R. Kikuchi, K. Eguchi, *Appl. Catal. A* 378 (2010) 234-242.
- [72] Y.-P. Li, T.-J. Wang, C.-Z. Wu, H.-B. Li, X.-X. Qin, N. Tsubaki, *Fuel Process. Technol.* 91 (2010) 388-393.
- [73] J. Li, Y. Tan, Q. Zhang, Y. Han, *Fuel* 89 (2010) 3510-3516.
- [74] D.-K. Lee, D.-S. Kim, T.-H. Kim, Y.-K. Lee, S.-E. Jeong, N.T. Le, M.-J. Cho, S.D. Henam, *Catal. Today* 154 (2010) 237-243.
- [75] S.-H. Kang, J.W. Bae, K.-J. Woo, P.S.S. Prasad, K.-W. Jun, *Fuel Process. Technol.* 91 (2010) 399-403.
- [76] M.A. McDonald, D.A. Storm, M. Boudart, *J. Catal.* (1986) 386-400.
- [77] S. Bessell, *Appl. Catal. A* 96 (1993) 253-268.
- [78] S. Bessell, *Appl. Catal. A* 126 (1995) 235-244.
- [79] S. Abelló, A. Bonilla, J. Pérez-Ramírez, *Appl. Catal. A* 364 (2009) 191-198.
- [80] B. Louis, F. Ocampo, H.S. Yun, J.P. Tessonier, M.M. Pereira, *Chem. Eng. J.* 161 (2010) 397-402.
- [81] S. Sartipi, K. Parashar, M.J. Valero-Romero, V.P. Santos, B. van der Linden, M. Makkee, F. Kapteijn, J. Gascon, *J. Catal.* 305 (2013) 179-190.

- [82] Y. Liu, J. Luo, M. Girleanu, O. Ersen, C. Pham-Huu, C. Meny, *J. Catal.* 318 (2014) 179-192.
- [83] C. Xing, G. Yang, M. Wu, R. Yang, L. Tan, P. Zhu, Q. Wei, J. Li, J. Mao, Y. Yoneyama, N. Tsubaki, *Fuel* 148 (2015) 48-57.
- [84] H. Zhang, X. Dong, G. Lin, X. Liang, H. Li, *Chem. Commun.* (2005) 5094-5096.
- [85] X. Dong, X. Liang, H. Li, G. Lin, P. Zhang, H. Zhang, *Catal. Today*, 147 (2009) 158-165.
- [86] Y. Pei, Y. Ding, H. Zhu, J. Zang, X. Song, W. Dong, T. Wang, Y. Lu, *Catal. Lett.* 144 (2014) 1433-1442.
- [87] Y. Pei, Y. Ding, H. Zhu, H. Du, *Chin. J. Catal.* 36 (2015) 355-361.
- [88] J. Wang, P. A. Chernavskii, Y. Wang, A. Y. Khodakov, *Fuel* 103 (2013) 1111-1122.
- [89] J. Hee, K. H. Reddy, J. Sun, E. Yang, *Appl. Catal., A* 480 (2014) 128-133.
- [90] G. Liu, T. Niu, D. Pan, F. Liu, Y. Liu, *Appl. Catal., A* 483 (2014) 10-18.
- [91] G. Liu, Y. Geng, D. Pan, Y. Zhang, T. Niu, Y. Liu, *Fuel Process. Technol.* 128 (2014) 289-296.
- [92] S. Yeon, D. Shin, N. Nho, K. Shin, C. Jin, S. Nam, *Korean J. Chem. Eng.* 30 (2013) 864-870.

## Chapter 2

### Experimental section

UNIVERSITAT ROVIRA I VIRGILI

CATALYTIC CONVERSION OF SYNGAS TO ALCOHOLS AND HYDROCARBONS OVER TRANSITION METAL-BASED  
MICRO/MESOPOROUS CATALYSTS

Jordi Plana Pallejà

In this chapter the characterization techniques applied along the thesis project are described. The reaction system used in the different experiments is also presented. The preparation methods of the different catalysts, as well as the different reaction conditions for each section, will be described in their respective chapters.

## 2.1. Characterization techniques

The following characterization techniques were used to characterize fresh, calcined, H<sub>2</sub>-activated, and used catalysts:

- Inductively coupled plasma-optical emission spectroscopy (ICP-OES).
- X-ray diffraction (XRD).
- N<sub>2</sub> adsorption
- Transmission electron microscopy (TEM).
- Diffuse Reflectance Fourier Transform Infrared Spectroscopy (DRIFTS).
- H<sub>2</sub>-Temperature programmed reduction (H<sub>2</sub>-TPR).

### 2.1.1. Inductively Coupled Plasma-Optical Emission Spectroscopy

The chemical composition of the materials was analyzed by inductively coupled plasma-optical emission spectroscopy (ICP-OES). This equipment has two parts: the ICP and the optical spectrometer. The ICP generates a stable ionized plasma of Ar gas, where the nebulized sample is introduced. The resulting ions emit radiation at characteristic wavelengths for each element. This radiation is detected in the optical chamber, where the intensity of each wavelength is measured. The intensity of each element is compared to known concentrations of each element, and their concentration can be interpolated from the resulting calibration lines.

Before analysis by ICP, the solid samples had to be dissolved. The procedure was adapted to the characteristics of each material:

- Iron-containing materials were dissolved in a 1% solution of HNO<sub>3</sub>.
- Zeolite samples were digested in 50 mL of 1% H<sub>2</sub>SO<sub>4</sub> and 1% HF mixture in a Berghof microwave oven at 200°C.
- SBA-15 samples were digested in 50 mL of 1% H<sub>2</sub>SO<sub>4</sub> and 1% HF mixture in a Berghof microwave oven at 200°C.

Concentration of the resulting solutions was adjusted by dilution with milliQ-grade water, and their chemical composition was analyzed by ICP in a Spectro Arcos 165 spectrophotometer.

### 2.1.2. X-Ray Diffraction

X-ray diffraction (XRD) was used to identify the crystalline phases present in the fresh, calcined, and used catalysts, and to estimate their crystallite sizes. Crystallite size was estimated using the Debye-Scherrer equation [1,2]:

$$d = \frac{K \cdot \lambda}{b \cdot \cos\theta} \quad (2.1)$$

Where  $d$  corresponds to crystallite size,  $K$  is a constant value,  $\lambda$  is the X-ray wavelength,  $\theta$  is the incident Bragg diffraction angle in radians, and  $b$  is the corrected full width at half maximum (FWHM) of the peak, which is calculated with the following equation 2.2, where  $B$  is the observed FWHM of the peak, and  $\beta$  is the instrumental broadening [3]:

$$b = \sqrt{(B^2 - \beta^2)} \quad (2.2)$$

In this work, X-ray diffractograms were acquired by a Siemens EM-10110BU D5000 diffractometer in the Servei de Recursos Científics i Tècnics of the

Universitat Rovira i Virgili. Cu-K $\alpha$  radiation was obtained from a copper X-ray tube operated at 40 kV and 30 mA.

The angular 2 $\theta$  diffraction range was between 5 and 70° for the iron-based catalyst, with an angular step of 0.05° at 3 s per step.

The angular 2 $\theta$  diffraction range was between 5 and 40° for zeolite samples, with an angular step of 0.05° at 3 s per step.

### 2.1.3. N<sub>2</sub> Adsorption

Physisorption with N<sub>2</sub> is a common method to evaluate the specific surface area of porous materials. N<sub>2</sub> adsorption was performed at -196°C in a Quantachrome Quadrasorb-SI gas-adsorption analyzer. Before measurement, samples were outgassed under vacuum at 300°C for 10 h.

The Brunauer-Emmett-Teller (BET) method is used to evaluate total surface area according to equation 2.3, where  $p$  is the equilibrium pressure of adsorbed gas,  $p^0$  is the saturation vapour pressure at the adsorption temperature,  $p/p^0$  is the relative pressure,  $v$  is the volume of the adsorbed gas at relative pressure  $p/p^0$ ,  $v_m$  is the volume of the gas adsorbed when a monolayer is formed, and  $c$  is a constant (exponentially related to the energy of monolayer adsorption). [4]

$$\frac{p}{v \cdot (p^0 - p)} = \frac{1}{v_m \cdot c} + \frac{(c-1)}{v_m \cdot c} \cdot \frac{p}{p^0} \quad (2.3)$$

Specific BET surface area ( $S_{BET}$ ) is obtained from equations 2.4 and 2.5, where  $\sigma_m$  is the area of the molecular cross-section,  $n_m$  is the moles of gas adsorbed in a monolayer,  $N_A$  is the Avogadro number,  $\rho$  is the density of N<sub>2</sub>,  $M_m$  is the molecular mass of the adsorbate, and  $m$  is the mass of the adsorbent [5],

$$S_{BET} = \frac{\sigma_m \cdot n_m \cdot N_A}{m} \quad (2.4)$$

$$n_m = \frac{V_m \cdot \rho}{M_m} \quad (2.5)$$

Mesopore size distribution was obtained using the method of Barret, Joyner and Halenda (BJH) [6], and the t-plot method was used to discriminate between micro- and mesoporosity [7].

#### **2.1.4. Transmission Electron Microscopy**

The fresh and used samples were analyzed by transmission electron microscopy (TEM), which was performed in a JEOL JEM-1011 transmission electron microscope operated at 100 kV with point-to-point resolution of 0.2 nm. A few droplets of sample suspended in acetone were deposited on carbon-coated copper grids followed by evaporation at ambient conditions.

#### **2.1.5. Diffuse Reflectance Fourier Transform Infrared Spectroscopy**

DRIFTS (diffuse reflectance Fourier transform infrared spectroscopy) is a characterization technique useful to analyze the amount of acidic types present on the surface of a catalyst, as well as their type. Fourier transform infrared spectroscopy was carried out at 200°C in a Vertex 7 spectrometer from Bruker using a diffuse reflectance (DRIFTS) accessory equipped with a Praying Mantis high-temperature reaction chamber (Harrick), ZnSe windows, and a MCT detector. The sample holder was filled with powdered catalyst samples (~3 mg) mixed with KBr, and carefully leveled off to reduce reflections of the sample surface and to ensure reproducible results. The sample was pretreated in N<sub>2</sub> (5 Nml/min) at 400°C for 60 min, using a heating ramp of 10°C/min. Spectra were recorded in the range 1800-4000 cm<sup>-1</sup> by co-addition of 64 scans and a nominal resolution of 4 cm<sup>-1</sup>.

#### **2.1.6. H<sub>2</sub>-Temperature Programmed Reduction**

H<sub>2</sub>-Temperature programmed reduction (TPR) is a method used to evaluate the reduction efficiency of oxidized catalysts. A U-tube is filled with the catalyst sample, which is then pretreated to reaction conditions, and finally analyzed

using H<sub>2</sub> to completely reduce the metal oxides contained within. The variation in H<sub>2</sub> concentration in the gas is quantified using a thermal conductivity detector.

Zeolite-supported catalysts were measured in a ChemBet Pulsar TPR/TPD unit equipped with a thermal conductivity detector. Samples of ca. 50 mg of the oxides obtained by calcination of the precursors at 400°C were loaded in the U-quartz microreactor, pretreated in air (20 NmL/min) at 300°C for 1 h, and subsequently cooled to 50°C in the same atmosphere. The analysis was carried out in a mixture of 5 vol.% H<sub>2</sub> in N<sub>2</sub> (20 NmL/min), ramping the temperature from 50 to 900°C at 10°C/min. SBA-15 supported catalysts were measured in a Micromeritics Autochem HP 2950 unit equipped with a thermal conductivity detector, using the same analysis conditions as the zeolite-supported catalysts.

## 2.2. Catalyst preparation

### 2.2.1. Fe/ZSM-5 catalysts

FTS catalysts were prepared by coprecipitation at constant pH. Aqueous solutions of the metal nitrates (Fe(NO<sub>3</sub>)<sub>3</sub>·9H<sub>2</sub>O, Cu(NO<sub>3</sub>)<sub>2</sub>·3H<sub>2</sub>O, Mg(NO<sub>3</sub>)<sub>2</sub>·6H<sub>2</sub>O, Ca(NO<sub>3</sub>)<sub>2</sub>·4H<sub>2</sub>O, KNO<sub>3</sub>, 1 M of each) and the precipitating agent (Na<sub>2</sub>CO<sub>3</sub>, 4 wt.%) were simultaneously fed into a polypropylene vessel with a 905 Titrande automated titrator (Metrohm AG) equipped with two 800 Dosino<sup>®</sup> dosing systems. The pH during precipitation in the stirred reactor vessel was maintained at a constant value of 8. After the addition of the appropriate ratio of reactants, the slurry was aged at 60°C for 1 h under vigorous stirring. The precipitate obtained was filtered and washed thoroughly with deionized water and dried overnight at 80°C to yield the catalyst precursor (Fe-P). This sample was calcined in static air at 300°C for 4 h using a heating rate of 5°C/min (labeled as Fe). The addition of copper was intended to facilitate the reduction of iron oxides [8], while potassium enhances the surface basicity and the production of olefins [9]. The addition of magnesium increases the BET surface area of the catalyst and

leads to the formation of relatively smaller  $\alpha$ -Fe<sub>2</sub>O<sub>3</sub> crystallites in the catalysts, facilitating the reduction and carburization [10].

Fe-zeolite bifunctional catalysts were prepared by physically mixing the Fe oxide with the same amount of a commercially ZSM-5 zeolite: Z40 (CBV 8014, Zeolyst International) and Z240 (Süd Chemie AG). Prior to any treatment, the as-received powders were calcined in static air at 550°C for 6 h at 5°C/min. Zeolites were subjected to alkaline treatments to create mesoporosity, following the procedure reported elsewhere [11,12]. Briefly, a 0.2 M NaOH aqueous solution was stirred at 500 rpm and heated at 65°C, after which the zeolite was added (3.3 g of zeolite per 100 mL of alkaline solution), and maintained for 30 min. Afterwards, the zeolite suspension was cooled down in an ice-water mixture, and centrifuged. The resulting solid was washed with distilled water until pH neutral and dried at 100°C. The solids were separated into two portions. The first ones were directly calcined in static air following the program described for the commercial zeolites, while the second portions were brought into the ammonium form via three successive exchanges in 0.1 M NH<sub>4</sub>NO<sub>3</sub> aqueous solution (1 g of zeolite per 100 mL of solution) and calcined in static air. All bifunctional catalysts were ground in the 100-300  $\mu$ m particle size. Along the manuscript, the alkali-treated samples are generally identified by the code Zx-AT and Zx-AT-H, where x refers to the Si/Al ratio according to the manufacturer, AT refers to the alkali-treated zeolites, and H identifies the alkali-treated samples subjected to ulterior Na<sup>+</sup> exchange.

### 2.2.2. SBA-15/FeCoCu catalysts

Catalysts were prepared by impregnation of mesoporous silica SBA-15 (Glantreo Ltd.) in a rotary evaporator at 65°C with an ethanol solution containing adequate amounts of the nitrate salts of each metal (Fe, Co and Cu). After evaporation of ethanol, the resulting products were further dried at 100°C overnight, heated at 5°C/min until 400°C and calcined under air at this temperature for 6 hours. The catalysts were labeled FeCoCu X/Y/Z, where X, Y

and Z refer to the mass percent of iron, cobalt and copper, respectively. Catalysts doped with Na and K were prepared by a second impregnation of the FeCoCu calcined catalyst, using salts of sodium ( $\text{NaNO}_3$ ) and potassium ( $\text{KNO}_3$ ). Doped catalysts were named FeCoCu-Na, and FeCoCu-K, and contained 1% wt. of their respective doping agent. Used catalysts had the added suffix “-U”.

## 2.3. Catalytic reaction system

### 2.3.1. FTS reaction system

The activity and selectivity of the catalysts were tested in a fully automated laboratory-scale fixed-bed catalytic reactor (Microactivity Reference, PID Eng&Tech, Spain).

Experiments using zeolite catalysts were conducted using 1.0 g of Fe catalyst and 1.0 g of zeolite, sieved to 100-300  $\mu\text{m}$ , and mixed with 500 mg of quartz chips sieved to the same particle size. A blank experiment was also performed by mixing the Fe base catalyst (1 g) with quartz chips (1.5 g) as reference. The catalysts were loaded into the reactor tube and heated at  $10^\circ\text{C}/\text{min}$  to  $300^\circ\text{C}$  under  $\text{N}_2$  (20  $\text{NmL}/\text{min}$ ), and reduced with syngas ( $\text{H}_2/\text{CO}$  molar ratio = 2) at the same temperature and 10 bar while starting to monitor product formation. The reaction was prolonged for 48 h at constant conditions of T and P using a weight-hourly space velocity (WHSV) of  $0.05 \text{ mol}_{\text{CO}}/\text{g}_{\text{cat}}\cdot\text{h}$ . The reactor effluent passed through a cold trap kept at  $2^\circ\text{C}$  and 10 bar to collect all liquid products and waxes if present.

The composition of the gaseous products (permanent gases and light hydrocarbons) was determined with an inline 3-channel gas microchromatograph equipped with a TCD detector (490 microGC, Agilent Technologies). The sensitivity of the detector to each analyzed compound (response factor) was determined periodically by their calibration against standards of certified gas mixtures using  $\text{N}_2$  as internal standard.



**Figure 2.1.** Catalytic reaction system.

Liquid products collected at low temperature during the FT tests with zeolite catalysts were analyzed in a two-dimensional GCxGC system coupled to a mass spectrometer (Agilent 7890A), equipped with a flame ionization detector (FID) and mass spectrometry (MSD 5975C) using a differential flow modulator. The system consisted in two columns, a 30 m non-polar column (DB-5MS) and a 5 m polar column (HP-INNOWAX), giving rise to the orthogonal two-dimensional

separation. The modulator isolates the eluent of the first column into a large number of adjacent small fractions, which are reinjected into the second column, resulting in a fast separation on this column (1.5 s). Detector signals were monitored with Agilent Chemstation software (Agilent). Data were converted with the GC-Image software (Zoex) for data processing. This technique has been considered to be superior to one-dimensional gas chromatography to analyze the selectivity of the catalyst since it elucidates compounds with similar boiling points but different functionality, which tend to co-elute [13]. Besides, minor compounds present in low concentrations in the Fischer-Tropsch sample matrices can be separated, detected and quantified. This technique has been very useful to determine differences between all products obtained herein.

Figure 2.2 exemplifies a typical two-dimensional contour plot of the liquid products obtained with the FeZ240-AT bifunctional catalyst. As a general trend the products had a wide range of elution times in the polar column (Y-axis), which correspond to linear or branched paraffinic compounds at the bottom, whereas minor products located at the top are aromatics.

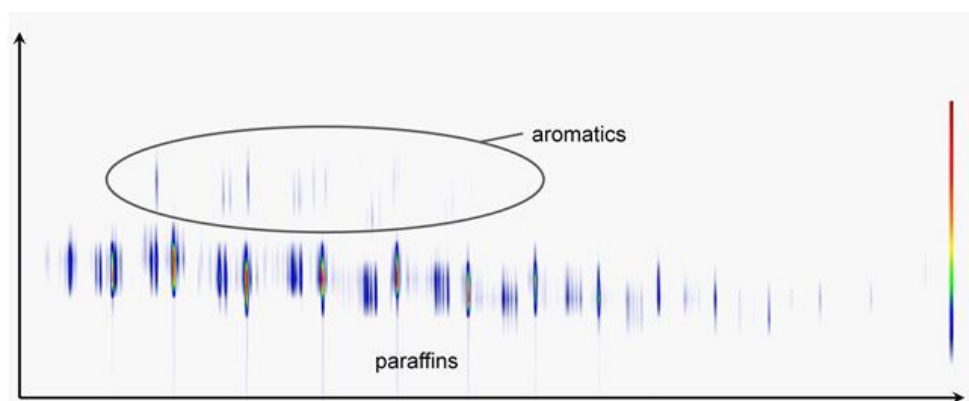


**Figure 2.2.** Contour plot of the analysis of the FTS liquid products by GCxGC/MS over the FeZ240-AT catalyst. Horizontal axis is retention time in the DB-5MS column (proportional to the carbon number of the product), while the vertical axis is retention time in the Innovax column (proportional to the polarity of the product).

### 2.3.2. HAS reaction system

The activity and selectivity of the catalysts were tested in a fully automated laboratory-scale fixed-bed catalytic reactor (Microactivity Reference, PID Eng&Tech, Spain).

Experiments using SBA-15 catalysts were conducted using 300 mg of catalyst particles sieved to 100-300  $\mu\text{m}$ . Due to the low bulk density of SBA-15 (0.067g/cm<sup>3</sup>), the catalysts were loaded inside the reactor undiluted above a bed of quartz wool, heated at 10°C/min to 300°C under N<sub>2</sub> (20.0 NmL/min), and then reduced at the same temperature for 3 h by adding 20.0 NmL/min of H<sub>2</sub>. Preliminary reaction tests showed a lack of catalytic activity at temperatures below 280°C and pressures below 25 bar. Therefore, all catalysts were screened at 300°C and 30 bar. Reaction tests were conducted during 24 h at a H<sub>2</sub>/CO molar ratio of 2.00, a pressure of 30.0 bar(g) and a space velocity (WHSV) of 0.30 mol<sub>CO</sub>/(g<sub>cat</sub>·h). A constant flow rate of 5.00 NmL/min of N<sub>2</sub> was also added to the feed gas as internal standard for the GC analysis of the product gas. The product stream was cooled down to 10°C in a high-pressure gas-liquid separator.

The liquid products collected in the HAS tests using SBA-15 were measured and analyzed offline using a gas chromatograph (Agilent 6850 Network GC System) equipped with a FID detector. A CP-Wax 57 CB capillary column was used, and the instrument was calibrated routinely with certified standards containing C<sub>1</sub> to C<sub>7</sub> alcohols (Agilent Technologies Certified Reference Material 18801-60700A). Analysis of the liquid samples was performed by triplicate.

### 2.4. Conversion, selectivity, and mass balance

Carbon balance and global mass balance during the FT and HAS experiments were above 95% in all the reported experiments, indicating that there were no major losses of products during the experiments and that most products were accounted for.

Carbon monoxide conversion ( $X_{CO}$ ) and selectivity to the different products ( $S_j$ ) were calculated according to equations (2.6) and (2.7), where  $F_{CO,0}$  is the feed molar flow rate of CO,  $F_j$  is the molar flow rate of product  $j$  at the reactor outlet, and  $n_j$  is the number of carbon atoms in compound  $j$ . Hydrocarbon and alcohol chain growth probability ( $\alpha$ ) was calculated using the Anderson-Schulz-Flory (ASF) model. Equation (2.8) shows the ASF distribution equation in terms of selectivity [14]. Reported uncertainties for all quantities represent confidence intervals at a 95% probability level, unless otherwise stated. Preliminary tests using similar catalysts showed good reproducibility of catalytic activity.

$$X = \frac{F_{CO,0} - F_{CO}}{F_{CO,0}} \quad (2.6)$$

$$S_j = \frac{F_j \cdot n_j}{F_{CO,0} - F_{CO}} \quad (2.7)$$

$$S_j = n_j (1 - \alpha)^2 \alpha^{n_j - 1} \quad (2.8)$$

## 2.5. Bibliography

- [1] A. Patterson, *Phys. Rev.* (1939) 978-982.
- [2] J.W. Niemantsverdriet, *Spectroscopy in catalysis: an introduction*, John Wiley & Sons; 2007.
- [3] L. Alexander, H.P. Klug, *J. Appl. Phys.* (1950) 137-142.
- [4] S. Brunauer, P.H. Emmett, E. Teller, *J. Am. Chem. Soc.* 60 (1938) 309-319.
- [5] M. Thommes, K. Kaneko, A.V. Neimark, J.P. Olivier, F. Rodriguez-Reinoso, J. Rouquerol, et al, *Pure Appl. Chem.* (2015) 1051-1069.
- [6] E.P. Barret, L.G. Joyner, P.H. Halenda, *J. Am. Chem. Soc.* 73 (1951) 373-380.
- [7] B.C. Lippens, J.H.d. Boer, *J. Catal.* 4 (1965) 319-323.
- [8] Y. Yoneyama, J.J. He, Y. Morii, S. Azuma, N. Tsubaki, *Catal. Today* 104 (2005) 37-40.
- [9] M.V. Cagnoli, N.G. Gallegos, A.M. Alvarez, J.F. Bengoa, A.A. Yeramian, M. Schmal, S.G. Marchetti, *Appl. Catal. A* 230 (2002) 169-176.
- [10] J. Yang, Y. Sun, Y. Tang, Y. Liu, H. Wang, L. Tian, H. Wang, Z. Zhang, H. Xiang, Y. Li, *J. Mol. Catal. A: Chem.* 245 (2006) 26-36.
- [11] J.C. Groen, S. Abelló, L.A. Villaescusa, J. Pérez-Ramírez, *Microp. Mesoporous Mater.* 114 (2008) 93-102.
- [12] D. Verboekend, T.C. Keller, M. Milina, R. Hauert, J. Pérez-Ramírez, *Chem. Mater.* 25 (2013) 1947-1959.
- [13] T. Grobler, M. Claeys, E.v. Steen, M.J. Janse van Vuuren, *Catal. Commun.* 10 (2009) 1674-1680.
- [14] D. Förtsch, K. Pabst, E. Groß-Hardt, *Chem. Eng. J.* (2015) 333-346.

## Chapter 3

# Fischer-Tropsch Synthesis: Influence of zeolite acidity and mesoporosity

UNIVERSITAT ROVIRA I VIRGILI

CATALYTIC CONVERSION OF SYNGAS TO ALCOHOLS AND HYDROCARBONS OVER TRANSITION METAL-BASED  
MICRO/MESOPOROUS CATALYSTS

Jordi Plana Pallejà

In this chapter the effect of zeolite acidity and mesoporosity development in bifunctional Fe/ZSM-5-based catalysts has been investigated. Since the desilication method used to create mesoporosity is prone to alter acidic properties in the zeolite, changes in product selectivity were systematically evaluated over non-acidic hierarchical Fe/ZSM-5 catalysts. To check effects specific for the zeolite, a comparison with a blank experiment containing no zeolite was also performed. A detailed study of the composition of liquid products has been fulfilled with the use of comprehensive two-dimensional gas chromatography mass spectroscopy (GCxGC/MS).

### 3.1. Characterization of the catalysts

The metallic catalyst, containing 39% wt. Fe, 2% wt. Cu, and 59% wt. Mg, had molar Fe/Cu and Fe/Mg ratios of 16.7 and 0.82, which closely matched the nominal ratios of 20 and 0.67, respectively. Concerning commercial zeolites, their bulk molar Si/Al ratio was 38.9 for Z40 and 224 for Z240. The amount of alkaline metals (Na and K) was also analyzed for the various catalysts. No samples contained potassium above the detection limit. Both non-treated catalysts (Z40 and Z240) contained amounts sodium below the detection limit. In the case of sodic zeolites, Z40-Na and Z240-Na contained 2.75% wt. and 1.11% wt., respectively. Alkaline treated zeolites (Z40-AT and Z240-AT) also had sodium below the limit of detection. These results indicate that sodium was correctly introduced in the sodic catalysts, and that it was removed successfully from the alkaline treated ones.

Figure 3.1 shows the XRD patterns of the coprecipitated material (Fe-P), and its product after calcination. The as-prepared sample displayed a low-crystallinity pattern ascribed to the presence of iron-copper hydroxide species. The solid calcined at 300°C showed characteristic reflections of the magnetite Fe<sub>3</sub>O<sub>4</sub> structure (75-1609 ICDD pattern). No diffraction lines associated with any other iron oxide were detected. The characteristic X-ray diffraction pattern of the MFI structure was also confirmed in all commercial ZSM-5 samples,

evidencing the typical high crystallinity of this structure, regardless of their Si/Al molar ratio. Alkaline-treated zeolites without (Zx-AT) or with subsequent ion exchange (Zx-AT-H) retained their crystalline structure, although gave less intense signals in the diffractogram. This change is due to the silicon extraction process occurring during alkaline treatment [5].

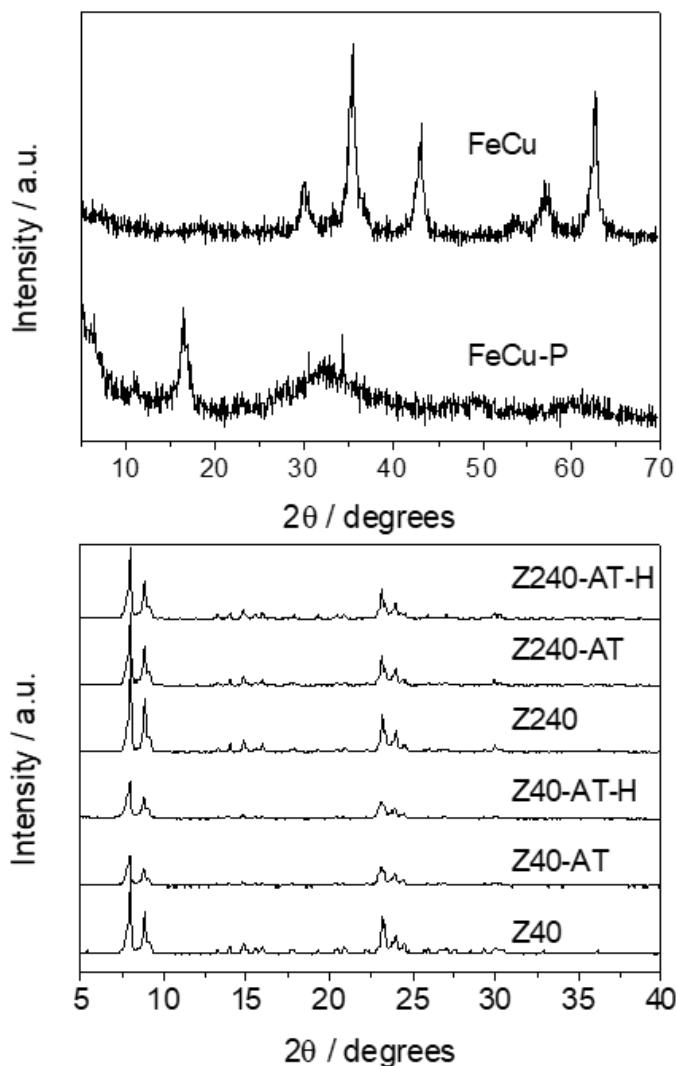


**Figure 3.1.** XRD patterns of the Fe-P precursor and the Fe catalyst (top), and MFI zeolites (bottom).

**Table 3.1:** Chemical composition and textural properties of the FTS catalyst and the commercial and alkaline-treated zeolites.

Sample	$V_{\text{micro}}$ (ml/g)	$V_{\text{pore}}$ (ml/g)	$S_{\text{micro}}$ (m <sup>2</sup> /g)	$S_{\text{meso}}$ (m <sup>2</sup> /g)	$S_{\text{BET}}$ (m <sup>2</sup> /g)
Fe-P	-	0.321	-	-	151.9
Fe	-	0.330	-	-	144.9
Z40	0.165	0.272	383.9	73.3	457.2
Z40-AT	0.117	0.437	277.1	98.5	375.6
Z40-AT-H	0.080	0.611	208.5	281.6	490.1
Z240	0.147	0.271	313.1	57.3	370.4
Z240-AT	0.140	0.445	301.8	84.7	386.5
Z240-AT-H	0.130	0.485	307.8	128.8	436.6

The main physico-chemical properties of both the Fe-based catalyst and the treated zeolites are summarized in Table 3.1. The N<sub>2</sub> adsorption isotherms at -196°C of the Fe catalyst and its precursor in Figure 3.2 exhibit a type IIb isotherm with H3 hysteresis, which are characteristic of mesoporous materials with slit-shaped pores between aggregates of particles with fiber-like morphology. The BET surface area (ca. 150 m<sup>2</sup>/g) and pore volume (0.3 mL/g) of the iron catalyst and its precursor were very similar, indicating that calcination did not exert any important effect on the porosity of the derived oxide.

The N<sub>2</sub> isotherms of the commercial zeolites exhibited the IUPAC type I behavior with a high uptake at low relative pressure, confirming their microporous character (Figure 3.2). Both commercial zeolite samples showed typical BET surface areas (370-460 m<sup>2</sup>/g) irrespective of the Si/Al ratio. The micropore volume ( $V_{\text{micro}}$ ) (0.15-0.17 mL/g) was also characteristic of the MFI framework. The mesopore surface area ( $S_{\text{meso}}$ ) (55-75 m<sup>2</sup>/g) responded to the crystal external surface, surface roughness of the crystals and the intercrystalline porosity derived from the aggregation of nanocrystals of less than 1 μm.

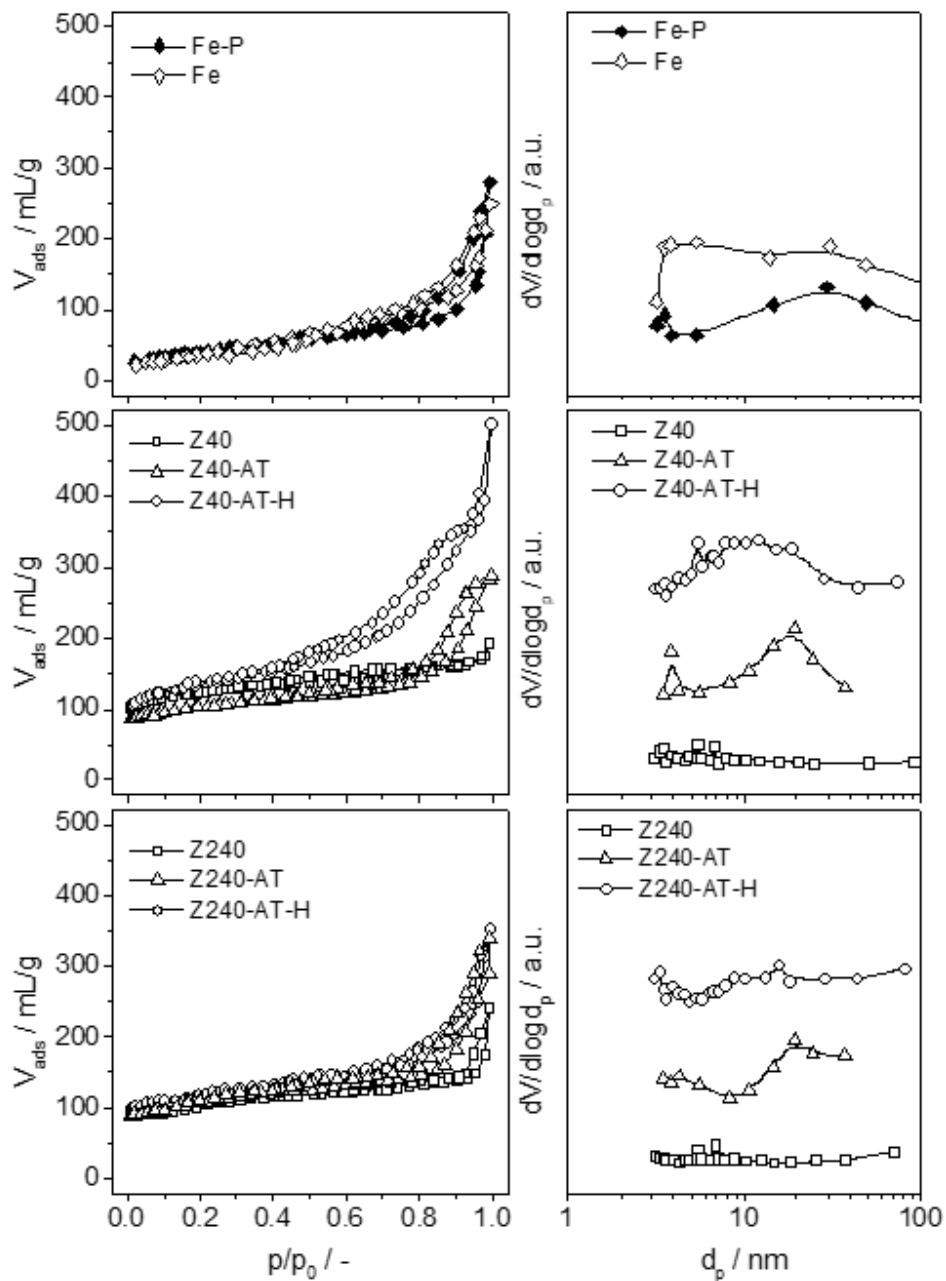


**Figure 3.2.**  $N_2$  adsorption isotherms (left) and BJH adsorption pore size distributions (right) of the Fe catalyst and the native and treated zeolites.

Absence of hysteresis in the isotherm indicates that the high values of  $S_{\text{meso}}$  are caused by external surface area rather than intracrystalline mesoporosity.

The two commercial zeolites were subjected to alkaline treatment in 0.2 M NaOH at 65°C for 30 min (Zx-AT in Table 3.1), which are the optimal conditions for MFI zeolites [6]. The  $N_2$  isotherms of Z40-AT and Z40-AT-H were similar, and characteristic of hierarchical porous zeolites combining micro- and mesoporosity. They displayed an enhanced uptake at intermediate and high pressures (0.4-0.8) with H3 hysteresis. The largely parallel progression of the adsorption and desorption branches of the hysteresis loops, and the absence of a forced closure of the desorption branch at  $p/p_0 \sim 0.45$ , give indication of the presence of accessible mesopores connected to the outer surface. The  $N_2$  isotherms of Z240-AT and Z240-AT-H showed adsorption at relative pressures above 0.7, indicating the formation of larger pores. The degree of silicon extraction and mesoporosity development were lower in Z240-AT compared to Z40-AT, as expected for the higher framework Si/Al ratio [6]. Indeed, the mesopore surface area in Z240-AT-H was twice that of its parent sample (129  $m^2/g$  vs 57  $m^2/g$ ). The increase of mesopore surface area was from 73  $m^2/g$  in Z40 to 282  $m^2/g$  in Z40-AT-H. In parallel, the total pore volume of the treated materials increased at the expense of a reduction in the micropore volume. Alkali-treated materials without final ion exchange (samples Z40-AT, and Z240-AT) displayed intermediate  $S_{\text{meso}}$  and  $V_{\text{micro}}$  values, probably due to some degree of blockage by Na cations inside the porous structures.

Development of mesoporosity was also confirmed by the BJH adsorption pore size distributions (Figure 3.2, right), showing the formation of mesopores centered around 20 nm in Z40-AT, and 10 nm in Z40-AT-H. The blockage by  $Na^+$  ions in the pore channels of the alkaline-treated sample is responsible for the shift in PSD to higher values (pores centered at 20 nm). A much broader pore size distribution was found on Z240-AT and Z240-AT-H, in agreement with the lower degree of mesoporosity attained over the Z240 sample.

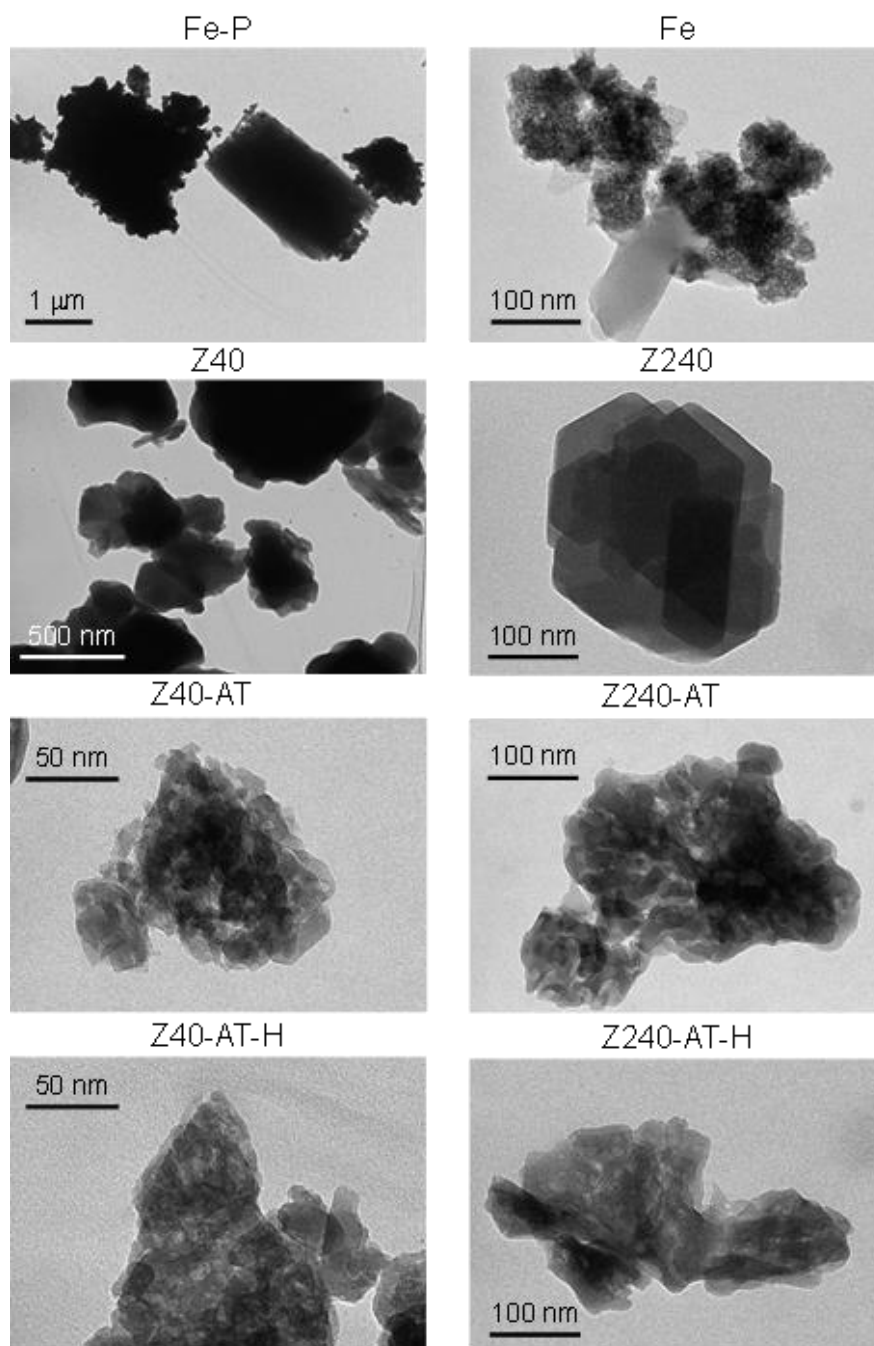


**Figure 3.3.** Transmission electron micrographs of the Fe catalyst and the native and treated zeolites.

This broadening is likely consequence of the formation of larger pores (>20 nm), which because of the diminishing surface to volume ratio at larger diameters make pore volume to grow faster than pore surface. Desilication of the zeolite to a Si/Al ratio of 25 to 50 has been considered to be the optimal range for silicon extraction while preserving acidity [6]. Excessive Si dissolution occurs in Z240-AT leading to larger pores, as evidenced in this sample and its corresponding ion-exchanged zeolite (Z240-AT-H). As expected, the desilication produced by NaOH treatment led to a decreased Si/Al ratio from 39 to 24 in Z40 and from 224 to 66 in Z240. The original crystallinity of the zeolites was not altered based on X-ray diffraction (Figure 3.1, right).

Transmission electron microscopy (TEM) in Figure 3.3 shows the presence of perforated crystals in Z40-AT and Z40-AT-H compared to the dense appearance of the microporous Z40 sample. A similar behavior was observed in the Z240-AT and Z240-AT-H samples, together with a more damaged structure than in Z240, which exhibited well-defined crystals.

Infrared spectroscopy in the OH-stretching region was carried out at 200°C after treating the samples at 400°C in N<sub>2</sub>, to qualitatively evaluate the acidity of the calcined and alkaline-treated zeolites. As shown in Figure 3.4, the zeolite samples show characteristic absorption bands at 3740 cm<sup>-1</sup>, 3660 cm<sup>-1</sup>, and 3600 cm<sup>-1</sup>, assigned to terminal silanol groups (Si-OH) on the external surface, hydroxyl groups connected to extra-framework Al species (EFAL, Lewis acidity), and bridging hydroxyl groups associated with Brønsted acidity, respectively [7,8]. A priori, it is expected that the number of Brønsted sites increases with increasing the Al content, that is, when decreasing the Si/Al ratio [9]. This correlation was verified when the Si/Al ratio increased from 40 to 240, showing a qualitative decrease in intensity of the band at 3600 cm<sup>-1</sup>. This latter absorption band completely vanished after alkaline treatment in both zeolites, due to the ion exchange with Na<sup>+</sup>. The spectrum of alkaline-treated samples treated by ion exchange in NH<sub>4</sub>NO<sub>3</sub> and calcined subsequently (Z40-AT-H and Z240-AT-H)

showed a recovery of their Brønsted sites, albeit with a lower intensity compared to the non-treated samples, in agreement with the loss of micropore volume. A progressive development of isolated silanol groups (band at  $3740\text{ cm}^{-1}$ ) was visible in the same samples, due to the formation of intracrystalline mesoporosity [4]; a slight increase in the amount of Lewis acid sites was discerned in alkaline-treated samples compared to non-treated zeolites.

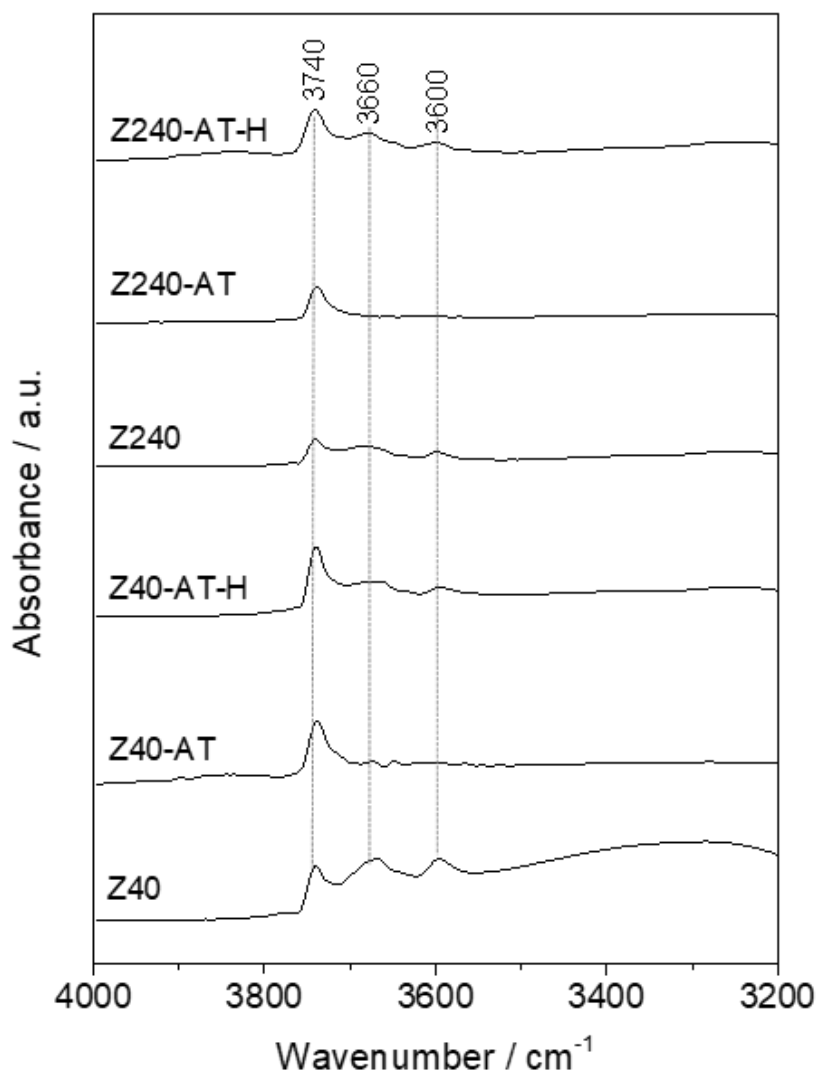


**Figure 3.4.** FTIR spectra in the OH-stretching region of the native and treated zeolites.

## 3.2. Fischer-Tropsch performance

### 3.2.1. Influence of Si/Al ratio of the untreated zeolite

An initial CO conversion of about 85% was found over the base Fe catalyst, which diminished to about 75% after 48 hours (Figure 3.5), thus showing a moderate deactivation during this period. After the addition of the zeolites, no influence of the Si/Al ratio on CO conversion was observed. In fact, the initial CO conversion was around 90% when using the FeZ40 catalyst, with a similar decay than in the Fe base catalyst, and only 75% with FeZ240. Despite its lower initial activity, the latter catalyst exhibited a more stable behavior upon time on stream.

Selectivity to main products is shown in Table 3.2. CO<sub>2</sub> selectivity was very similar in all cases, ca. 70%, indicating that the addition of zeolite was not affecting the WGS reaction, in which iron is known to be an active catalyst [10]. Due to the large amount of CO<sub>2</sub>, selectivity results in the following figures were expressed as selectivity to hydrocarbons (without CO<sub>2</sub>). Most of the paraffins quantified in Table 3.2 are related to branched compounds (i.e. iso-paraffins).

**Table 3.2:** Mass selectivity and olefin to paraffin ratio of the Fe catalyst alone and mixed with commercial and alkaline-treated zeolites.

Catalyst	Selectivity / -				O/P ratio
	CO <sub>2</sub>	Paraffin	Olefin	Aromatic	
Fe	$7.03 \cdot 10^{-1}$	$2.71 \cdot 10^{-1}$	$1.94 \cdot 10^{-2}$	$6.60 \cdot 10^{-3}$	$7.16 \cdot 10^{-2}$
FeZ40	$6.98 \cdot 10^{-1}$	$1.69 \cdot 10^{-1}$	$2.77 \cdot 10^{-2}$	$1.05 \cdot 10^{-1}$	$1.64 \cdot 10^{-1}$
FeZ40-AT	$6.92 \cdot 10^{-1}$	$2.73 \cdot 10^{-1}$	$3.50 \cdot 10^{-2}$	0.00	$1.28 \cdot 10^{-1}$
FeZ40-AT-H	$6.95 \cdot 10^{-1}$	$1.87 \cdot 10^{-1}$	$3.41 \cdot 10^{-2}$	$8.39 \cdot 10^{-2}$	$1.82 \cdot 10^{-1}$
FeZ240	$6.77 \cdot 10^{-1}$	$1.88 \cdot 10^{-1}$	$2.65 \cdot 10^{-2}$	$1.09 \cdot 10^{-1}$	$1.41 \cdot 10^{-1}$
FeZ240-AT	$6.91 \cdot 10^{-1}$	$2.66 \cdot 10^{-1}$	$4.30 \cdot 10^{-2}$	0.00	$1.62 \cdot 10^{-1}$
FeZ240-AT-H	$7.11 \cdot 10^{-1}$	$1.62 \cdot 10^{-1}$	$2.87 \cdot 10^{-2}$	$9.83 \cdot 10^{-2}$	$1.77 \cdot 10^{-1}$

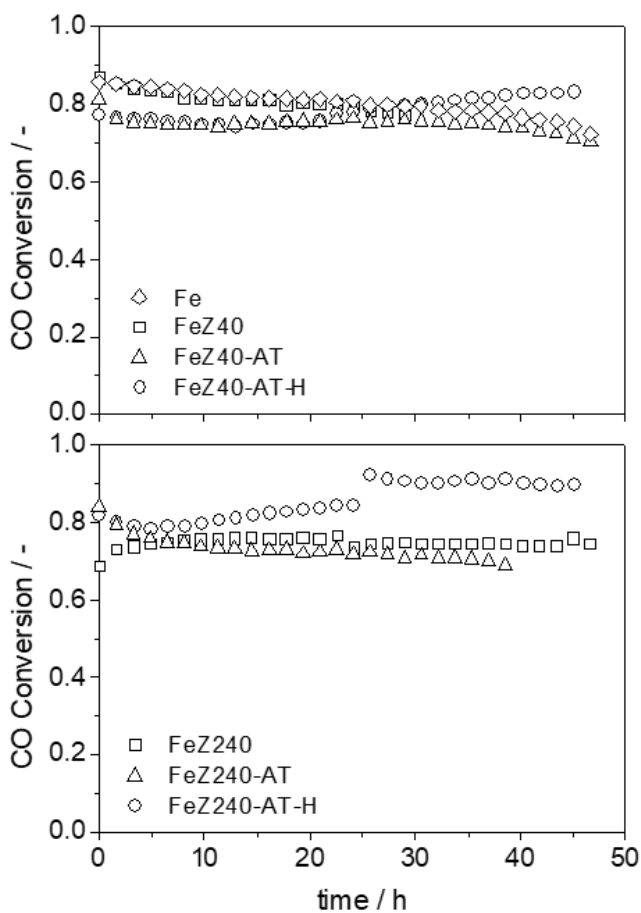


**Figure 3.5.** CO conversion vs. time during FTS over the Fe catalyst and mixed with the different zeolites. Reaction conditions:  $H_2/CO$  ratio = 2,  $T = 300^\circ C$ ,  $WHSV = 0.05 \text{ mol}_{CO}/(\text{g}_{cat}\cdot h)$ , and  $P = 10 \text{ bar}$ .

The Fe base catalyst exhibited a high selectivity towards paraffins in the range  $C_1$ - $C_{20}$  (Figure 3.6), with a very low olefin-to-paraffin ratio, and practically no aromatics. Addition of the commercial zeolites led to important differences in product selectivity, i.e., the selectivity to aromatics increased from 1% (in the base Fe catalyst) to ca. 10% concomitantly to decreased paraffin selectivity in

FeZ40 and FeZ240. The selectivity to C<sub>2</sub>-C<sub>4</sub> was similar (ca. 25%) for both bifunctional catalysts, while the selectivity in the range C<sub>5</sub>-C<sub>12</sub> (typical of gasoline) increased from 30% in the base Fe catalyst to 49% in FeZ240, showing a progressive increase with the Si/Al ratio (Figure 3.7). FeZ40 and FeZ240 showed practically no differences in products selectivity (17% and 19% for paraffins, and 10% and 11% for aromatics, respectively). Although these results seem to show subtle differences between catalysts, the general differences observed can be explained in terms of Brønsted acidity offered by the zeolites with different Si/Al ratio, as zeolites with higher Al content have higher amount of Brønsted acid sites [9,11]. As previously observed in Figure 3.4, the amount of acidic sites in Z40 is slightly higher than in Z240, thus facilitating the formation of aromatic products, especially, towards more complex structures in the most acidic catalysts, as shown below.

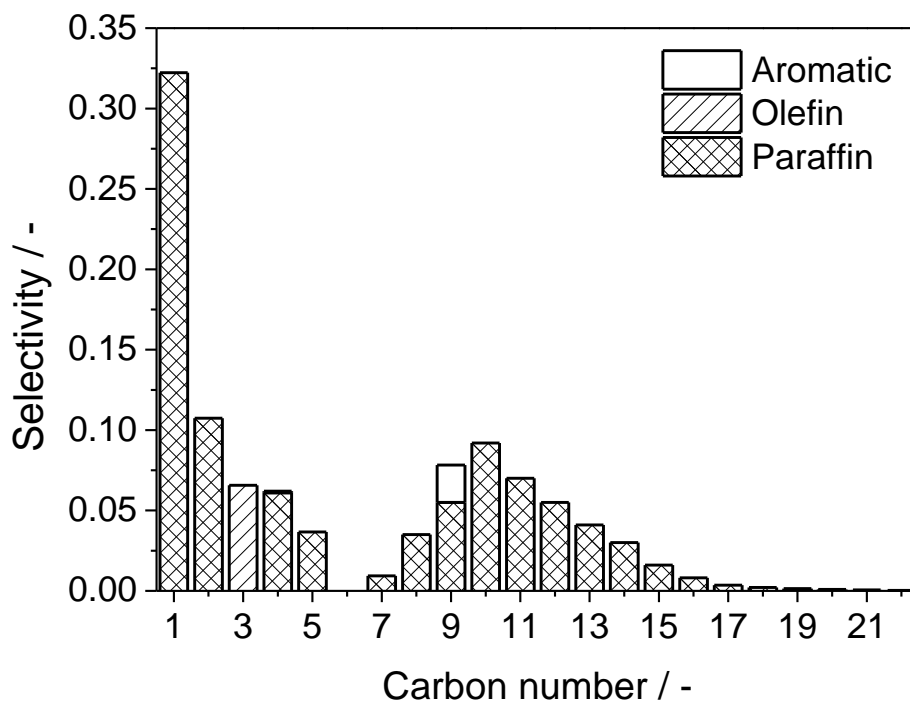
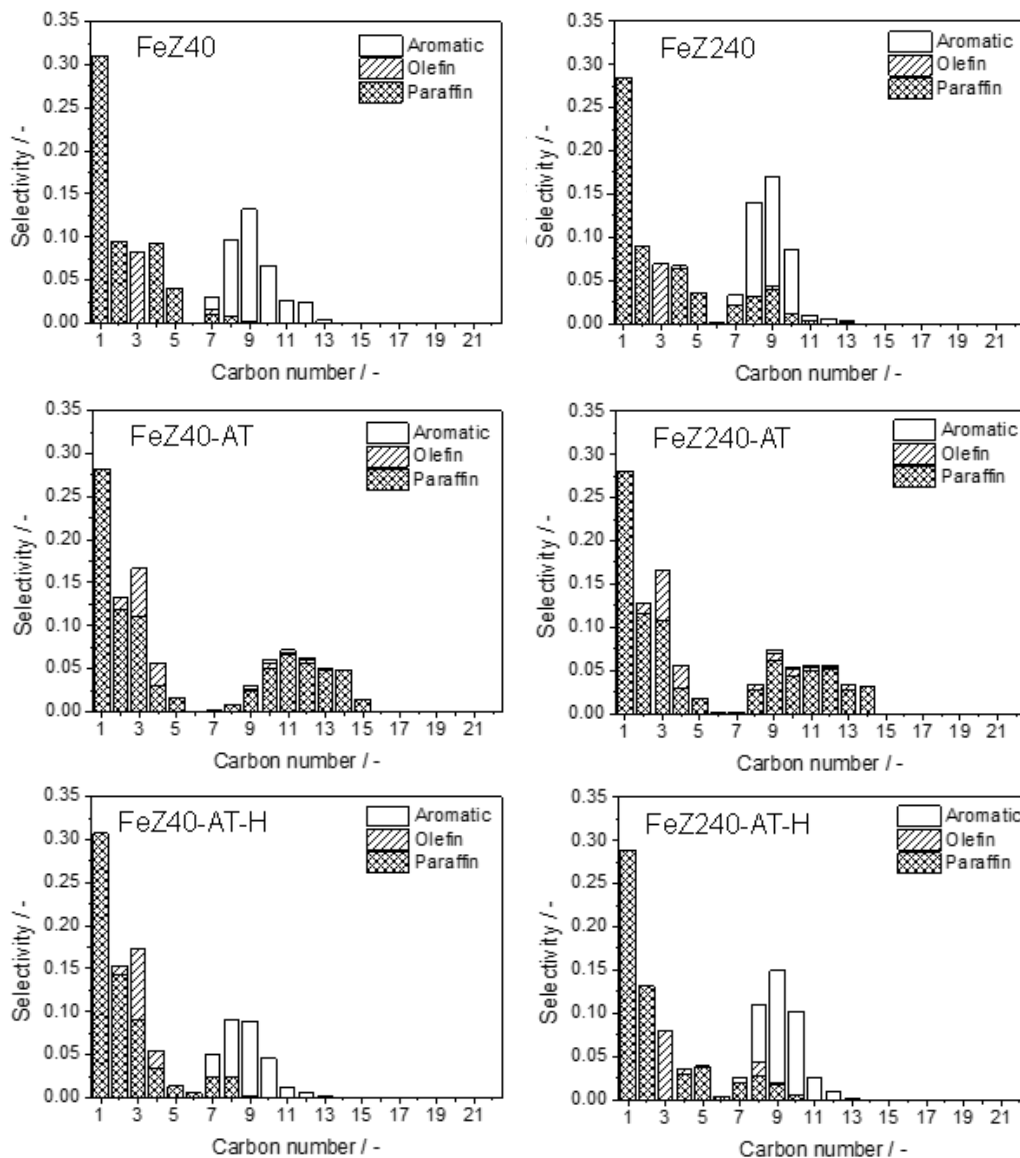


Figure 3.6. FTS product mass distribution over the Fe catalyst.



**Figure 3.7.** FT product mass distribution over the different Fe-based bifunctional catalysts.

Most aromatic products were comprised in the C<sub>7</sub>-C<sub>12</sub> range and were composed of branched benzenes (alkylbenzenes). The increased acidity in Z40

over Z240 led to the production of heavier aromatics, even reaching molecules with 14 carbons (i.e. branched naphthalenes). The percentage of lighter aromatics (7-10 carbons) increased in the opposite sense, that is, from Z40 to Z240. Less  $A_8$ – $A_{10}$  and more  $A_{11+}$  compounds were formed in FeZ40 compared to FeZ240. This may imply that aromatization occurs in the Brønsted acid sites located inside the micropores (with diffusion constraints), which are poisoned upon reaction favoring the formation of heavier aromatics at the external acid sites. In contrast, the less acidic character of the FeZ240 catalyst induces the slightly higher formation of  $A_8$ – $A_{10}$  products without suffering changes in activity along the 48 h time on stream.

These results confirm not only that the zeolite acidity is responsible for cracking of heavy hydrocarbons, and the formation of aromatics by oligomerization, cyclization, and dehydrogenation of primary short olefins produced over the Fe catalyst [12,13], but also that the degree of acidity induces noticeable differences in the distribution of aromatic products. In agreement with previous literature [14], our results also show that this transformation is motivated by a change in the ASF distribution, which decreases the  $C_{12+}$  selectivity. The presence of acidic sites in the zeolites promotes cracking and isomerization reactions, and also, a higher degree of aromatization in Fe-based bifunctional catalysts. Also, the increment in acidic sites in FeZ40, with low Si/Al ratio, led to the formation of more complex aromatic structures ( $>C_{11+}$ ).

### 3.2.2. Influence of mesoporosity

Primary hydrocarbons formed on active sites of a FTS are able to migrate into the zeolite micropores, where the above-mentioned processes occur. However, the products formed must diffuse out of the micropores of the zeolite, and this may partially lead to overcracking towards lighter hydrocarbons [15]. In order to overcome this issue, desilication treatments were performed over selected zeolites to evaluate the effect of mesoporosity generation on the performance of Fe/hierarchical zeolites. The main effect of alkaline treatment is the extraction

of framework silicon leading to an interconnected network of micropores and mesopores (and extensive surface area). Without subsequent ion exchange with  $\text{NH}_4\text{NO}_3$ , the hierarchical zeolite remained in the sodic form, and therefore, no Brønsted sites were present. In this work we have evaluated the effect of mesoporosity development by measuring the catalytic performance using zeolites with or without  $\text{Na}^+$  exchange. A priori, the presence of  $\text{Na}^+$  in the alkaline-treated zeolites was expected to provide a similar FTS performance than with the Fe base catalyst, if only acidity is considered. However, the effect of enhancement in mesoporous surface area was investigated to evaluate possible changes in product distribution when no  $\text{Na}^+$  exchange was performed.

Figure 3.5 shows CO conversion vs. time on stream for the alkaline-treated samples with (FeZx-AT-H) or without (FeZx-AT) subsequent ion exchange. The activity of both FeZ40-AT and FeZ240-AT was slightly lower than their parent counterparts, thus indicating that the blockage of pores by  $\text{Na}^+$  was in fact reducing the diffusion of reactants and products along the porous structure. On the contrary, both FeZ40-AT-H and FeZ240-AT-H displayed an increased CO conversion, especially in the latter catalyst, which is even slightly increased along the reaction. This can be explained by the fact that the presence of mesopores favored the transport of bulky products, thus avoiding deactivation by blocking and coke formation.

Concerning product selectivity, results are shown in Figure 3.7. Products with  $>\text{C}_{15}$  obtained with the bifunctional catalysts were found in trace amount below the quantification limit of the instrument and were not considered. Selectivity in FeZ40-AT and FeZ240-AT was substantially and qualitatively different from that obtained over FeZ40 and FeZ240. The results are quantified in Figure 3.7 and summarized in Table 3.2. Most of the products were paraffins and only a very small increase in the amount of olefins was detected, especially in the range  $\text{C}_2\text{-C}_4$ , over both alkali-treated materials. In fact, these results are quite similar to those of the product distribution of the Fe catalyst alone (Figure 3.7), with minor

differences: slightly lower selectivity to methane, formation of minor amount of olefins, and absence of products above  $C_{14}$  in the bifunctional catalysts (at least being quantifiable). This suggests that virtually no secondary reactions (hydrocracking, oligomerization, cyclization, etc.) occurred when using the non-acidic bifunctional catalysts (FeZ40-AT and FeZ240-AT), but in contraposition, the presence of mesopores limited the size of the paraffins formed up to  $C_{14}$ .

Both FeZ40-AT and FeZ240-AT exhibited similar product distribution (Figure 3.8). Therefore, the effect of mesoporosity development in alkaline-treated zeolites (without  $Na^+$  exchange, which do not retain their Brønsted acidity) is somewhat affecting the catalytic performance in these bifunctional catalysts, as even without acidic sites seemed to change the ASF product distribution.

As expected from the recovery of Brønsted acid sites (Figure 3.4), the use of the acidic zeolites, FeZ40-AT-H, and FeZ240-AT-H led to a high  $C_5$ - $C_{12}$  selectivity again with respect to the Na-containing catalysts, due to cracking of heavy FT products over the acid sites. In parallel, the selectivity to  $C_{13+}$  was practically negligible, irrespective of the presence of mesopores in the alkaline-treated and ion exchanged samples. The selectivity to methane was practically not affected upon alkaline treatment of the zeolites. Compared with untreated bifunctional catalysts, both FeZ40-AT-H and FeZ240-AT-H showed a decreased selectivity to the  $C_5$ - $C_{12}$  fraction, concomitantly to the slight increase in the  $C_2$ - $C_4$  carbon range (Figure 3.7). The amount of aromatics marginally decreased in FeZ40-AT-H at the expenses of a slight increment in  $C_2$ - $C_4$  paraffins (Table 3.2). These results are better summarized in Figure 3.8, where products are grouped into typical cuts according to the number of carbons. Not only the acidity of this material still favored cracking and isomerization, but also the better accessibility of the mesopores induced the formation of lighter compounds. In the case of FeZ240-AT-H, the alkaline treatment followed by ion exchange seemed to produce no significant effects, as the total amount of aromatics was practically equivalent to that in FeZ240. However, less acidic bifunctional catalysts (i.e. FeZ240 and

FeZ240-AT-H) were more selective towards the gasoline-range products with respect to bifunctional catalysts with low Si/Al ratio zeolites.

These results suggest that the presence of mesoporosity and acidity of these zeolites play a key role in modifying the gasoline-range selectivity. As previously reported, alkaline treatment and subsequent  $\text{NH}_4\text{NO}_3$  ion exchange (followed by calcination) should lead to a partial recovery of the strong Brønsted acidity [16]. Following this, the increase in mesoporosity while keeping a certain level of acidity (similar or slightly below to that of the non-treated zeolites) seemed to somewhat hinder selectivity towards  $\text{C}_5\text{-C}_{12}$  hydrocarbons; that is, the preserved acidity promotes cracking, aromatization, etc., and the presence of mesopores helps reaching the active acid sites with less diffusional constraints.

In summary, developing mesoporosity provided a better accessibility of the acidic active sites for cracking and aromatization, although for the gasoline-range objective in FTS, this effect is partially detrimental. The Brønsted acidity, which is beneficial for cracking and aromatization reactions, was valuable to enhance the  $\text{C}_5\text{-C}_{12}$  hydrocarbon range. However, the generation of small mesopores produced a slight increase in the  $\text{C}_2\text{-C}_4$  fractions due to overcracking of heavy molecules in the acid sites. This effect was more pronounced for lower Si/Al ratios. Herein, the best performance towards gasoline products was achieved using a zeolite-containing bifunctional catalyst with higher Si/Al ratio (and intrinsic lower acidity), without direct influence on the presence of mesopores. In this direction, the typical benefits achieved by hierarchical zeolites (possessing both micro and mesoporosity and preserved acidity) in a large number of heterogeneously catalyzed reactions [17] need to be optimized for each specific application and, more particularly, to the product/s of interest when complex reactions like FTS are concerned.

## Fischer-Tropsch Synthesis: influence of zeolite acidity and mesoporosity

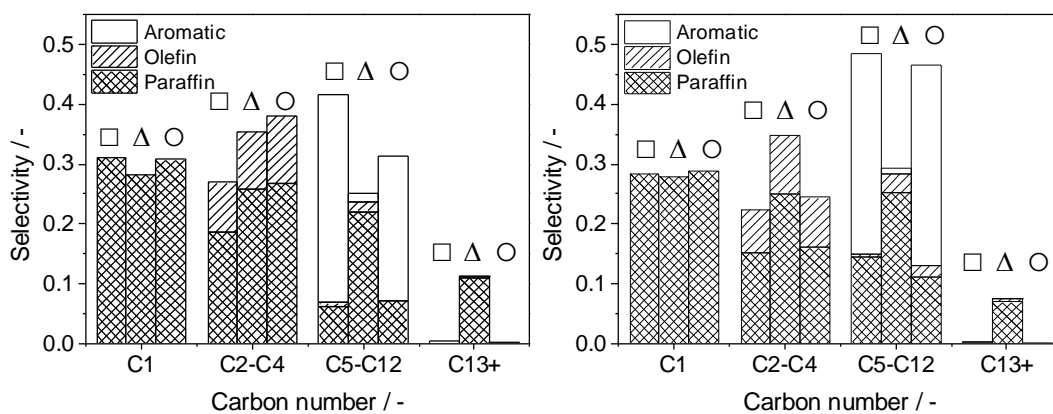


**Figure 3.8.** Mass selectivity towards paraffins, olefins or aromatics over the different bifunctional catalysts. In each carbon number group, left graph: FeZ40 ( $\square$ ), FeZ40-AT ( $\triangle$ ), FeZ40-AT-H ( $\circ$ ); right graph: FeZ240 ( $\square$ ), FeZ240-AT ( $\triangle$ ), and FeZ240-AT-H ( $\circ$ ).

### 3.3. Bibliography

- [1] S. Abelló, A. Bonilla, J. Pérez-Ramírez, *Appl. Catal. A* 364 (2009) 191-198.
- [2] J.C. Groen, L.A.A. Peffer, J.A. Moulijn, J. Pérez-Ramírez, *Chem. Eur. J.* 11 (2005) 4983-4994.
- [3] A. Zecchina, S. Bordiga, G. Spoto, D. Scarano, G. Petrini, G. Leofanti, M. Padovan, *J. Chem. Soc. Faraday Trans.* 88 (1992) 2959-2969.
- [4] I. Kiricsi, C. Flego, G. Pazzuconi, W.O. Parker, R. Millini, C. Perego, G. Bellussi, *J. Phys. Chem.* 98 (1994) 4627-4634.
- [5] A. Martínez, C. López, *Appl. Catal. A* 294 (2005) 251-259.
- [6] J.C. Groen, S. Abelló, L.A. Villaescusa, J. Pérez-Ramírez, *Microp. Mesoporous Mater.* 114 (2008) 93-102.
- [7] S. Li, S. Krishnamoorthy, A. Li, G.D. Meitzner, E. Iglesia, *J. Catal.* 206 (2002) 202-217.
- [8] F.G. Botes, W. Böhringer, *Appl. Catal. A* 267 (2004) 217-225.
- [9] J. He, Z. Liu, Y. Yoneyama, N. Nishiyama, N. Tsubaki, *Chem. Eur. J.* 12 (2006) 8296-8304.
- [10] Q. Zhang, J. Kang, Y. Wang, *ChemCatChem* 2 (2010) 1030-1058.
- [11] K. Cheng, L. Zhang, J. Kang, X. Peng, Q. Zhang, Y. Wang, *Chem.–Eur. J.* 21 (2015) 1928-1937.
- [12] J. Kang, K. Cheng, L. Zhang, Q. Zhang, J. Ding, W. Hua, Y. Lou, Q. Zhai, Y. Wang, *Angew. Chem., Int. Ed.* 50 (2011) 5200-5203.
- [13] D. Verboekend, T.C. Keller, M. Milina, R. Hauert, J. Pérez-Ramírez, *Chem. Mater.* 25 (2013) 1947-1959.
- [14] J. Pérez-Ramírez, S. Mitchell, D. Verboekend, M. Milina, N.-L. Michels, F. Krumeich, N. Marti, M. Erdmann, *ChemCatChem* 3 (2011) 1731-1734.

## Chapter 4

# Higher Alcohol Synthesis: Effect of metal load and reaction conditions

UNIVERSITAT ROVIRA I VIRGILI

CATALYTIC CONVERSION OF SYNGAS TO ALCOHOLS AND HYDROCARBONS OVER TRANSITION METAL-BASED  
MICRO/MESOPOROUS CATALYSTS

Jordi Plana Pallejà

In this chapter, Fe, Co, and Cu metallic catalysts, supported on mesoporous silica SBA-15, have been synthesized and their activity and selectivity to the formation of higher alcohols investigated. In the first part of the chapter, bi- and trimetallic combinations of supported Fe, Co and Cu catalysts have been produced to investigate the combined effects of their active components towards higher alcohols synthesis. The second part of the chapter shows a variety of ternary catalysts with differing proportions between the three metals, in order to find the ternary catalyst with the best yield of higher alcohols. The third and final part of this chapter subjects the most performing catalyst from the second part of the chapter to further tests, with varying reaction conditions in order to evaluate their effect on conversion and selectivity towards higher alcohols synthesis. Additionally, doping with alkaline metals (K and Na) was also performed on the best catalyst to evaluate its effect on catalyst activity and its selectivity to alcohol formation.

## **4.1. Catalyst composition: binary vs ternary catalysts**

### **4.1.1. Characterization of fresh catalysts**

Table 4.1 shows the metallic load of the binary and ternary catalysts, determined by inductively coupled plasma optical emission spectrometry (ICP-OES). The real metallic charge of the different catalysts was slightly lower than its nominal value. However, the ratios among metals corresponded to the intended values. This indicates that the impregnation method used for the preparation of the catalysts was effective to entrap the metals inside the porous structure of the support.

Table 4.2 shows the textural properties (BET area, micro- and mesoporosity) of the binary and ternary catalysts. Nitrogen adsorption-desorption isotherms show that all samples followed type-IV isotherms with H1 type hysteresis, which is typical of mesoporous materials with cylindrical mesostructures. Commercial SBA-15 had a surface area of over 700 m<sup>2</sup>/g, which decreased to 400-650 m<sup>2</sup>/g

after impregnation with the metals, regardless of the metal content. Micropore volume was reduced to 25-50% of that of commercial SBA-15 (from 0.102 ml/g to 0.050-0.080 ml/g). In all cases the average pore size was between 6-9 nm.

**Table 4.1.** Metallic charge of the catalysts.

SBA-15 FeCoCu	Fe (wt. %)	Co (wt. %)	Cu (wt. %)
9/9/9	8.1	8.3	8.9
0/9/9	0.0	8.7	9.3
0/9/18	0.0	8.2	18.3
0/18/9	0.0	16.9	8.7
9/0/9	7.6	0.0	8.4
18/0/9	15.2	0.0	8.5
9/0/18	7.8	0.0	17.4
9/9/0	7.7	7.7	0.0

Figure 4.1 shows the reduction profiles of the calcined materials. These profiles are complex, as all three metals had reduction peaks at the same ranges (200-400°C). FeCoCu 9/9/0 had a small peak at 394°C, with a wide shoulder that corresponded to the reduction of Fe<sub>2</sub>O<sub>3</sub> and Co<sub>3</sub>O<sub>4</sub> oxides to their metallic state.

FeCoCu 9/0/9 and FeCoCu 18/0/9 displayed a peak centered at 237°C, caused by the reduction of CuO and the partial reduction of Fe<sub>2</sub>O<sub>3</sub> to Fe<sub>3</sub>O<sub>4</sub>, and small peaks from 350°C to 650°C that showed the complete reduction of Fe. FeCoCu 9/0/18 displayed a peak at 268°C, which encompassed the reduction of CuO and the partial reduction of Fe<sub>2</sub>O<sub>3</sub> to Fe<sub>3</sub>O<sub>4</sub>.

FeCoCu 0/9/9 and FeCoCu 0/9/18 had two defined peaks at ca. 284°C and ca. 319°C, which corresponded to the reduction of CuO and Co<sub>3</sub>O<sub>4</sub> to their metal phases, respectively. Catalyst FeCoCu 0/18/9 had wider peaks due to the excess of Cu, with a first peak at 250°C, followed by a wide peak finishing at 350°C.

**Table 4.2.** Textural properties of the binary and ternary catalysts.

FeCoCu	$V_{\text{micro}}$ (ml/g)	$V_{\text{pore}}$ (ml/g)	$S_{\text{micro}}$ (m <sup>2</sup> /g)	$S_{\text{meso}}$ (m <sup>2</sup> /g)	$S_{\text{BET}}$ (m <sup>2</sup> /g)
SBA-15	0.102	0.835	235	489	724
9/9/9	0.052	0.482	116	290	406
0/9/9	0.074	0.820	164	494	658
0/9/18	0.063	0.590	142	349	491
0/18/9	0.054	0.521	121	295	416
9/0/9	0.085	0.619	196	361	557
18/0/9	0.079	0.555	182	318	500
9/0/18	0.063	0.572	141	354	496

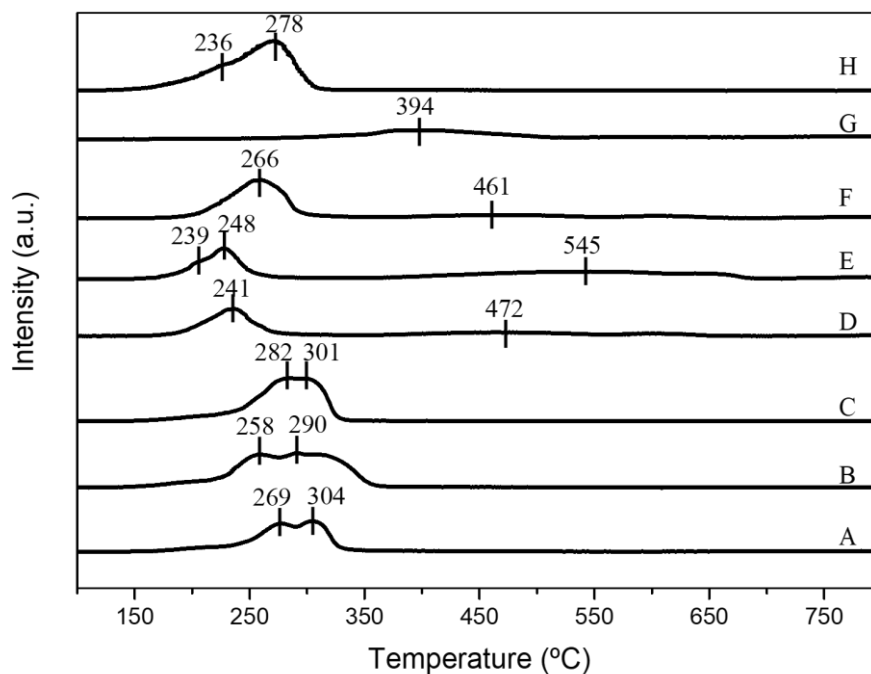


**Figure 4.1.** TPR- $H_2$  profiles of the FeCoCu catalysts. A: 0/9/9, B: 0/18/9, C: 0/9/18, D: 9/0/9, E: 18/0/9, F: 9/0/18, G: 9/9/0, H: 9/9/9.

The ternary catalyst FeCoCu 9/9/9 had a wide peak centered at 273°C, with shoulders at 245 and 311°C, caused by the reduction of CuO to Cu, Fe<sub>2</sub>O<sub>3</sub> to Fe<sub>3</sub>O<sub>4</sub> and Co<sub>3</sub>O<sub>4</sub> to Co [1], whereas the wide peak between 350-550°C corresponded to the reduction of Fe<sub>3</sub>O<sub>4</sub> to metallic iron via FeO [2, 3].

Figure 4.2 shows the X-ray diffractograms of the calcined catalysts, which had low crystallinity. In fact, FeCoCu 0/9/9, FeCoCu 9/0/9, FeCoCu 18/0/9 and FeCoCu 9/9/0 showed no crystalline phases. FeCoCu 0/18/9 and FeCoCu 0/9/18 had peaks corresponding to Cu<sub>x</sub>Co<sub>3-x</sub>O<sub>4</sub> spinels. FeCoCu 0/9/18 and FeCoCu 9/0/18 showed peaks of CuO, due to their higher content in copper. Ternary catalyst FeCoCu 9/9/9 showed the presence of crystalline Cu<sub>x</sub>Co<sub>3-x</sub>O<sub>4</sub> spinels.

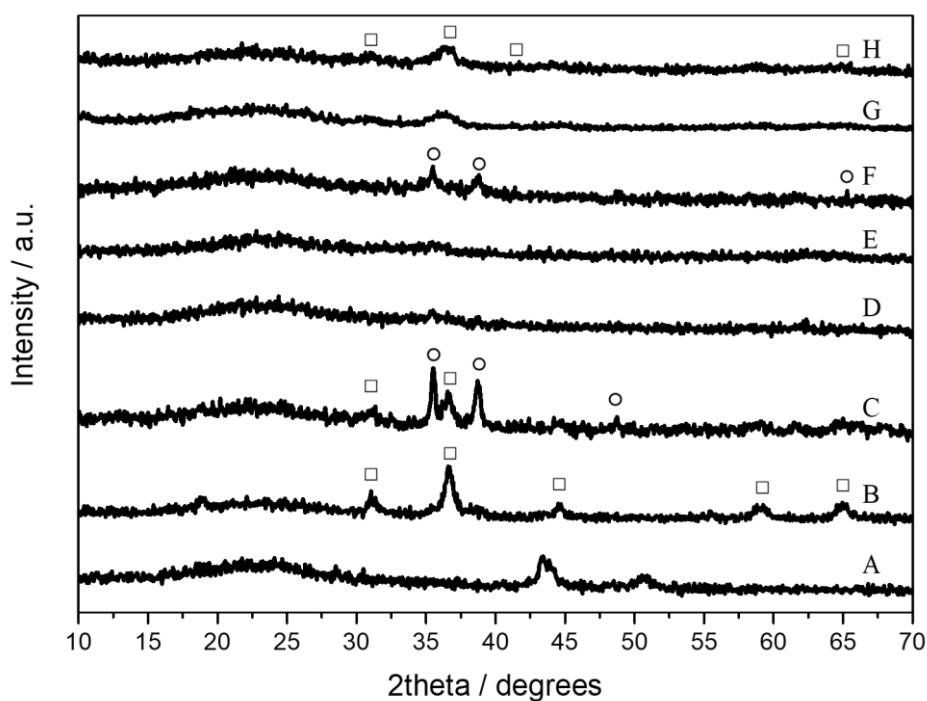


**Figure 4.2.** XRD of calcined catalysts. A: FeCoCu 0/9/9, B: FeCoCu 0/18/9, C: FeCoCu 0/9/18, D: FeCoCu 9/0/9, E: FeCoCu 18/0/9, F: FeCoCu 9/0/18, G: FeCoCu 9/9/0, H: FeCoCu 9/9/9. □: Cu<sub>x</sub> Co<sub>3-x</sub> O<sub>4</sub>, ○: CuO.

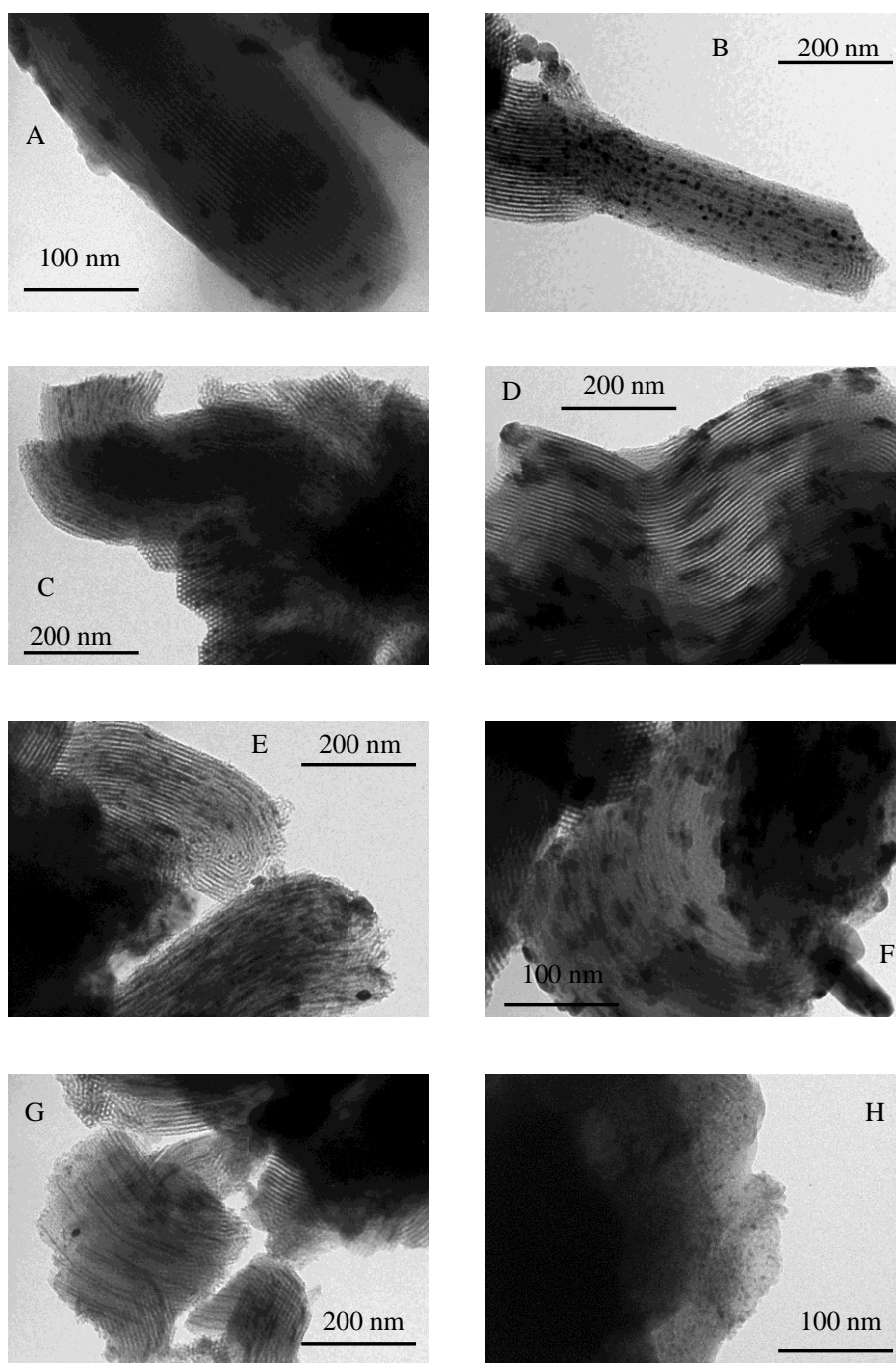


**Figure 4.3.** TEM images of the binary and ternary FeCoCu catalysts. A: 9/0/9, B: 18/0/9, C: 9/0/18, D: 0/9/9, E: 0/18/9, F: 0/9/18, G: 9/9/0, H: 9/9/9.

TEM imaging of the catalysts in Figure 4.3 shows that SBA-15 had uniform channels 9 nm wide, with enclosed metallic particles. Catalysts without cobalt (FeCoCu 9/0/9, 18/0/9, and 9/0/18) displayed small, regular particles 8-9 nm wide. In contrast, catalysts without iron (FeCoCu 0/9/9, 0/18/9, and 0/9/18) formed bigger aggregates, with diameters over 50 nm that embraced several SBA-15 channels. FeCoCu 9/9/0 showed the formation of metallic filaments inside the channels, which could be over 200 nm long. Ternary catalyst FeCoCu 9/9/9 showed small particles of 8-9 nm included inside the channels.

#### 4.1.2. Catalyst screening

All catalysts exhibited stable conversion after 24 hours of time on stream. The products obtained were hydrocarbons up to pentane in the gas stream and alcohols up to heptane dissolved in water.

FeCoCu 0/9/9 and FeCoCu 0/9/18 were found to be almost inactive, while FeCoCu 0/18/9 showed high conversion (30%), with a high selectivity towards hydrocarbons (72%) and CO<sub>2</sub> (16%). These results suggested that, in catalysts lacking iron, higher amounts of cobalt with respect to copper were necessary to obtain an active catalyst. FeCoCu 9/0/9, 18/0/9 and 9/0/18 gave similar CO conversions (between 21% and 27%). FeCoCu 9/0/9 produced the lowest amount of CO<sub>2</sub> and the highest yield of hydrocarbons (16% and 63%, respectively), and the highest selectivity towards alcohols (14%). FeCoCu 18/0/9 produced higher amounts of C<sub>2+</sub> hydrocarbons (42%) and the highest values of CO conversion (27%) but exhibited the worst performance towards alcohols selectivity (10%). FeCoCu 9/0/18 had moderate conversion (23%), as well as the highest selectivity towards CO<sub>2</sub> (22%). These results indicated that a higher iron content promoted CO conversion and improved selectivity towards hydrocarbons, but decreased selectivity towards alcohols.

FeCoCu 9/9/0 had a CO conversion of 20%, with high selectivity towards hydrocarbons (71%), as well as low selectivity towards CO<sub>2</sub>. This indicated that

the presence of cobalt in the catalyst decreased the activity of the WGS reaction. The ternary catalyst FeCoCu 9/9/9 gave moderate levels of conversion (15%) and showed intermediate WGS activity, but had the highest selectivity towards alcohols (16%). This showed the improved effect the combination of the three metals had on the reaction products pointing to the ratio between the three metals to be a key to improve conversion and selectivity towards alcohols.

The distribution of hydrocarbon products according to their carbon number is shown in Figure 4.5. All catalysts showed methane to be the main product, since it contained most of the carbon present in the hydrocarbon fraction. Catalysts without Co (FeCoCu 9/0/9, FeCoCu 18/0/9, and FeCoCu 9/0/18) had better selectivity to higher hydrocarbons, specially propane and pentane. This indicates that cobalt favored the production of methane, while iron favored growing of the hydrocarbon chains, thus resulting in heavier products.

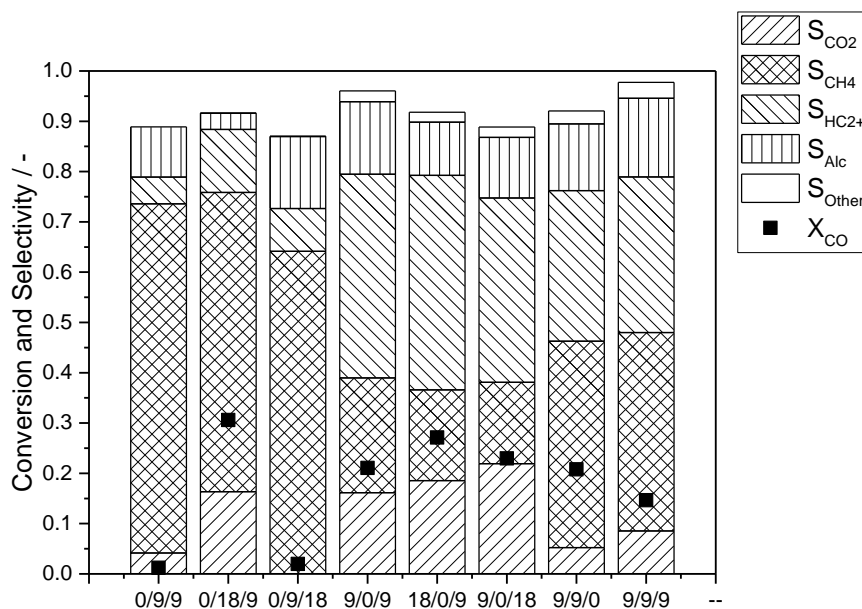


**Figure 4.4.** Conversion and selectivity of binary and ternary catalysts after 24 h of reaction. Reaction conditions: 30 bar, 300°C, 0.3 molCO/gcat-h, H<sub>2</sub>/CO = 2.

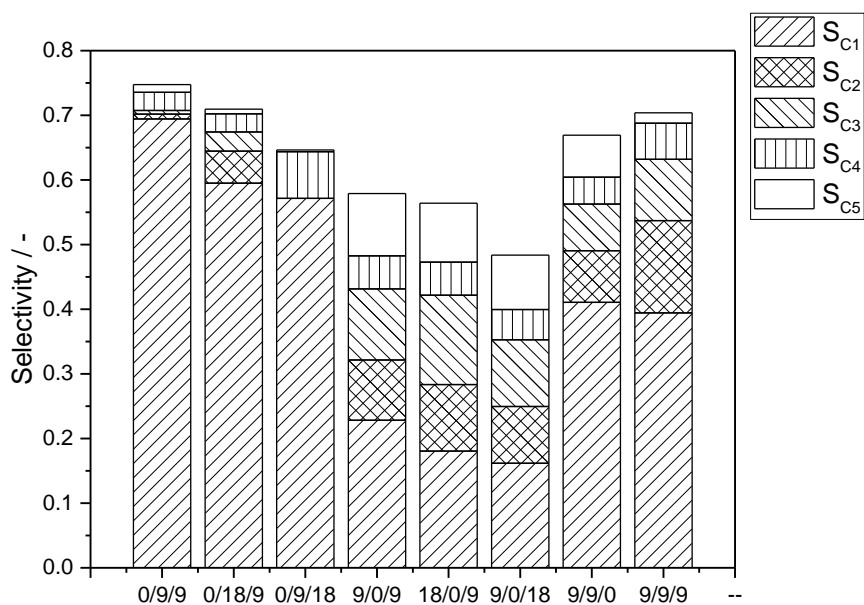


**Figure 4.5.** Selectivity towards hydrocarbons of the different catalysts.

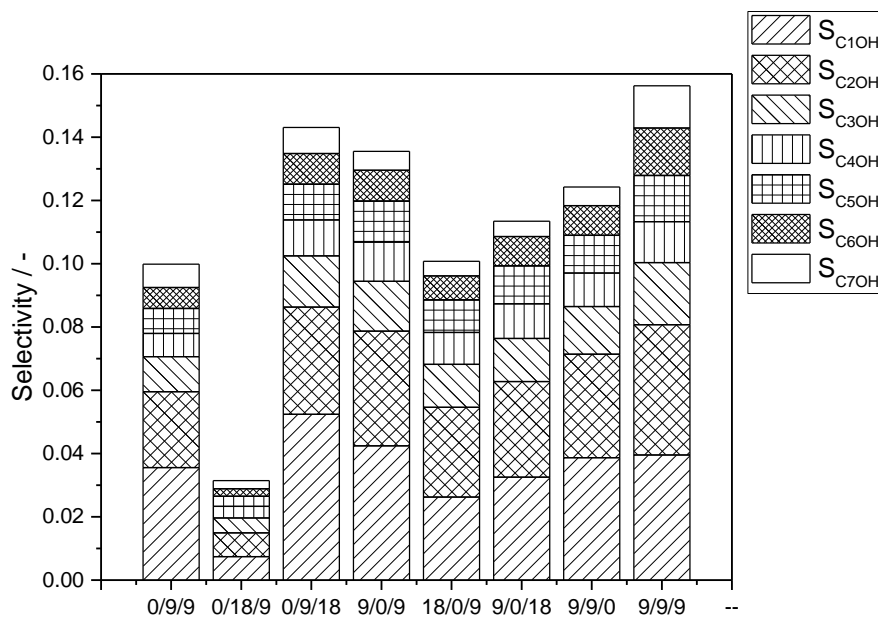


**Figure 4.6.** Selectivity towards alcohols of the different catalysts.

Regarding selectivity towards specific alcohols, methanol was the main alcohol produced in all binary catalysts, and the amount of higher alcohols tended to decrease with chain length. The ternary catalyst (FeCoCu 9/9/9) displayed a slightly higher selectivity towards ethanol instead of methanol (25% of methanol and 26% of ethanol), suggesting that the combination of the three metals provided the dual active sites required to promote the synthesis of higher alcohols. The combination of the three metals had a synergistic effect. FTS metals induced the dissociative insertion of CO to form surface alkyl-groups (C-C chain growth) and hydrogenation, and Cu promoted the associative insertion of CO and subsequent alcohol formation. Additionally, Co hindered the capacity of Fe to catalyze the WGS reaction, thus reducing the amount of CO<sub>2</sub>, while Cu improved the selectivity towards alcohols instead of hydrocarbons. This resulted in an improved distribution of products in the ternary system compared to the binary catalysts.

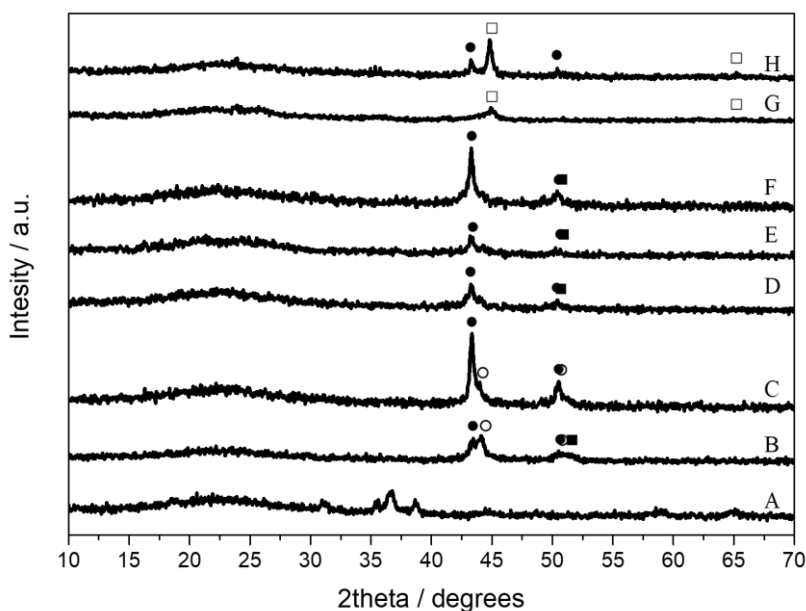


**Figure 4.7.** X-ray diffractograms of the used catalysts. A: 0/9/9, B: 0/18/9, C: 0/9/18, D: 9/0/9, E: 18/0/9, F: 9/0/18, G: 9/9/0, H: 9/9/9. □: CoFe, ○: Co, ●: Cu, ■: C.

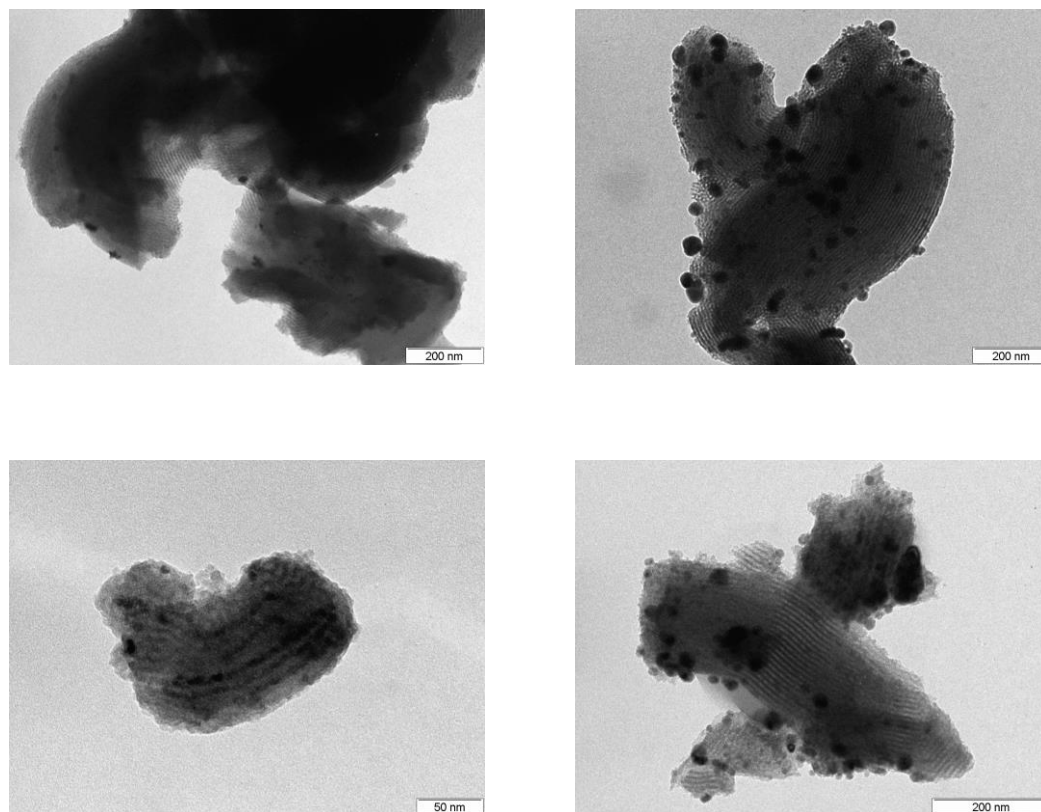


**Figure 4.8.** TEM images of used catalysts. A: FeCoCu 0/9/9-U, B: FeCoCu 9/0/9-U, C: FeCoCu 9/9/0-U, and D: FeCoCu 9/9/9-U.

#### 4.1.3. Characterization of used catalysts

Used catalysts were characterized after reaction, in order to assess potential changes in their morphology and structure. X-ray diffraction was performed to the used catalysts, as shown in Figure 4.7.

All materials had low crystallinity and exhibited reduction of the different oxides to their respective metals (Co and Cu). These changes could be attributed to the reduction with H<sub>2</sub> that was performed before reaction. Some materials also showed peaks corresponding to graphitic carbon deposited on the porous structure.

The TEM images of selected used catalysts are shown in Figure 4.8. The formation of larger aggregates of metal particles can be observed. These metallic clusters could range from 20 nm to over 80 nm wide and might be caused by the degradation of the catalyst by sintering over time.

## 4.2. Ternary catalysts: effect of metal loading

### 4.2.1. Characterization of fresh catalysts

The elemental composition of the synthesized materials was determined by ICP-OES. Table 4.3 shows that metal loads were slightly lower than their nominal values, but the ratios among the three metals were close to the target values.

Analysis of the textural properties of the calcined materials showed that all of them had a type-IV  $N_2$  adsorption-desorption isotherm and type-H1 hysteresis, which is a typical feature of mesoporous materials with cylindrical mesostructures.

As show in Table 4.3, commercial SBA-15 had a surface area of 724  $m^2/g$ , which diminished to ca. 400-500  $m^2/g$  after impregnation, regardless of the metal content. Micropore volume decreased from 0.102 mL/g in commercial SBA-15 to ca. 0.050-0.080 mL/g in the impregnated and calcined materials, due to the incorporation of metallic species in the SBA-15 pores. In all cases, the average pore size was between 6 and 9 nm.

Figure 4.9 shows the X-ray diffractograms of the catalysts after reduction with  $H_2$  at 300°C for 2 h. Characteristic peaks corresponding to the reduced metallic phases of iron and copper were observed in all materials, due to their reduction from metal oxides during the activation process. Metal oxides may remain eventually, although in a non-crystalline phase or not detected by XRD due to the relatively low crystallinity of the samples. FeCoCu 9/18/9 also showed crystalline phases corresponding to reduced Co, albeit at very low crystallinity. The average crystallite size of Fe was similar in all catalysts, with values ranging

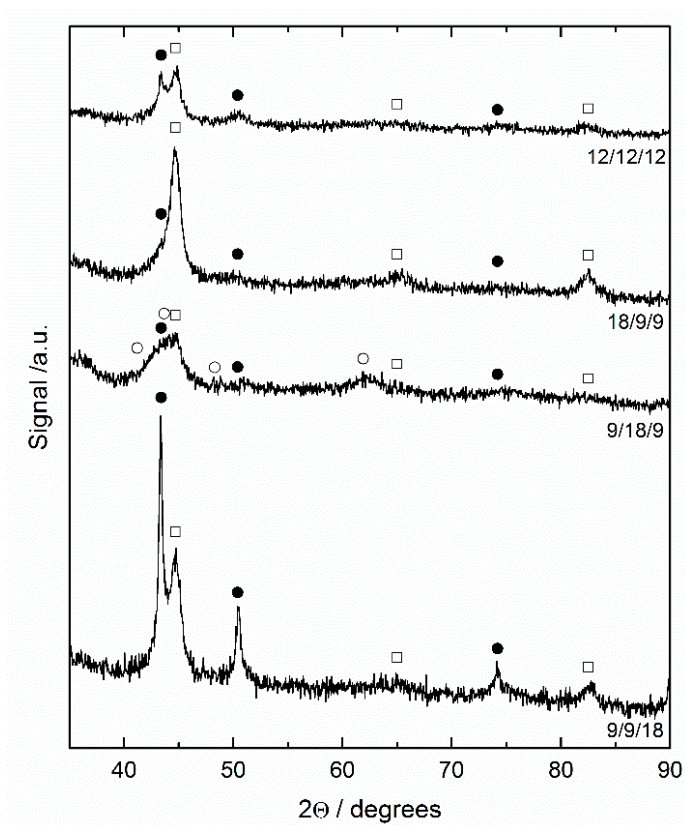
from 5.0 to 5.4 nm. Concerning Cu, narrower diffraction lines were observed in sample FeCoCu 9/9/18, in agreement with its higher average crystallite size of 14.2 nm. The other samples showed a regular trend with sizes in the range of 3.2 to 3.4 nm. This implies that higher Cu contents induced sintering upon reduction, and therefore, larger Cu<sup>0</sup> particles. The Co average crystallite size was not determined as was not easily discerned from the XRD background.

**Table 4.3.** Textural properties, metallic load, and H<sub>2</sub> consumption of the calcined FeCoCu catalysts and SBA-15.

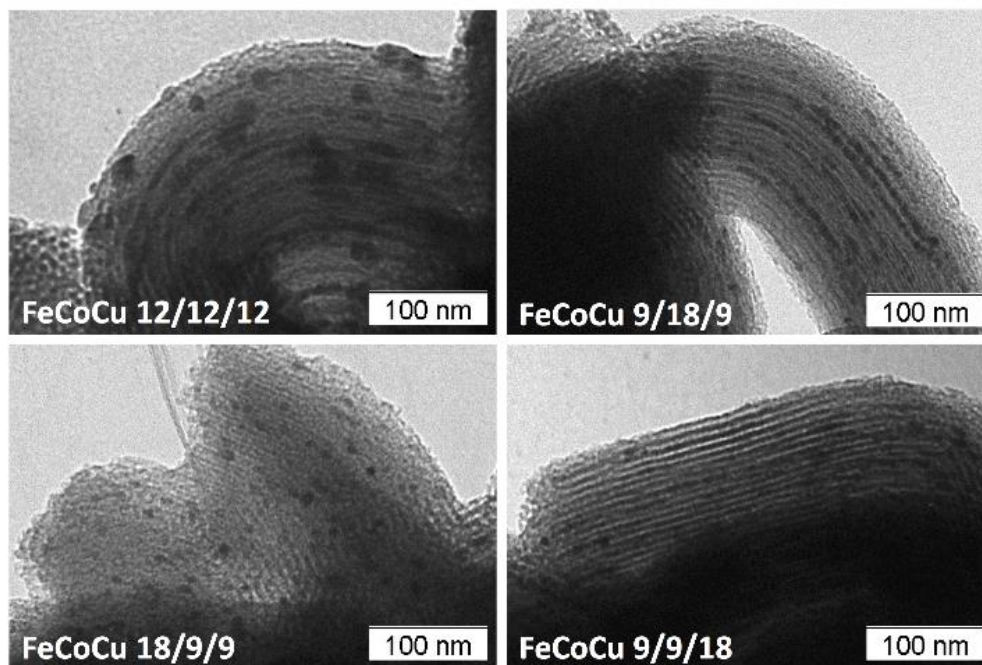
	SBA-15	FeCoCu 12/12/12	FeCoCu 18/9/9	FeCoCu 9/18/9	FeCoCu 9/9/18
V <sub>micro</sub> (mL/g)	0.102	0.076	0.059	0.073	0.066
V <sub>pore</sub> (mL/g)	0.835	0.576	0.494	0.567	0.577
S <sub>micro</sub> (m <sup>2</sup> /g)	235	176	135	168	150
S <sub>meso</sub> (m <sup>2</sup> /g)	489	324	299	335	346
S <sub>BET</sub> (m <sup>2</sup> /g)	724	500	434	503	496
Fe (%)	-	9.30	14.7	7.60	8.30
Co (%)	-	10.6	7.50	16.5	8.40
Cu (%)	-	11.6	8.00	8.20	18.9
H <sub>2</sub> cons. (mmol <sub>H2</sub> /g <sub>metal</sub> )	-	146	129	132	134
Ratio of H <sub>2</sub> consumption	-	0.83	0.69	0.75	0.82

Figure 4.10 shows TEM images of the calcined catalysts. The morphology of the SBA-15 support, which consisted in long and regular channels with 9 nm of internal diameter, could be clearly observed in all catalysts. Metal aggregates dispersed in the SBA-15 support were observed in all cases, but they varied in size and morphology depending on the combination of individual metal loads used to prepare the catalyst. Figure 4.11 shows the size distribution of the metal oxide particles in the fresh catalysts. FeCoCu 12/12/12 catalyst showed the

formation of metal aggregates of 14-19 nm distributed mainly on the outer walls of the SBA-15 particles, combined with small aggregates of 7-9 nm inside the SBA-15 channels. Using an excess of iron at a 36% total nominal metal load (FeCoCu 18/9/9) produced metal particulates of ca. 7-9 nm in diameter with an even distribution inside the channels of the SBA-15. No larger particles or aggregation of the small particles inside the channels were noticed. Large aggregates were not observed when Co was used in excess (FeCoCu 9/18/9), but the small metal particles inside the channels formed filiform structures like those in the FeCoCu 12/12/12 catalyst. On the contrary, an excess of Cu (FeCoCu 9/9/18) gave a structure where regular aggregates with sizes ranging from ca. 5 to 10 nm in diameter were formed inside the SBA-15 channels.



**Figure 4.9.** XRD of activated catalysts. Crystalline phases: (□) Fe, (●) Cu, (○) Co.



*Figure 4.10. TEM images of the calcined catalysts.*

The decrease in surface area reported in Table 4.3 could be related to the morphology of the deposited metal particles. As a general trend, the catalysts where only small and well distributed metal particles were present had the larger reduction in surface area and pore volume, which pointed to a larger fraction SBA-15 channels being partially blocked by the metal particles. In the catalysts where metal particles formed filiform structures or large clusters, lower channel blockage did occur because the metal tended to accumulate in fewer channels and was less dispersed throughout the porous structure.

Catalysts had consistent properties and did not exhibit significant variations in composition and textural characteristics between batches. Figure 4.12 shows the temperature-programmed reduction (TPR) profiles of the calcined materials. A relatively complex reduction pattern was observed because the three metals tended to reduce along the same temperature interval (180-300°C). Reduction

of CuO to Cu, Fe<sub>2</sub>O<sub>3</sub> to Fe<sub>3</sub>O<sub>4</sub> and Co<sub>3</sub>O<sub>4</sub> to Co, occurred between ca. 180°C and 225°C, which resulted in overlapped peaks and, in some cases, merged peaks. The wider peaks ranging from ca. 225°C to 500°C corresponded to the consecutive reduction of Fe<sub>3</sub>O<sub>4</sub> to FeO and then to metallic Fe [3].

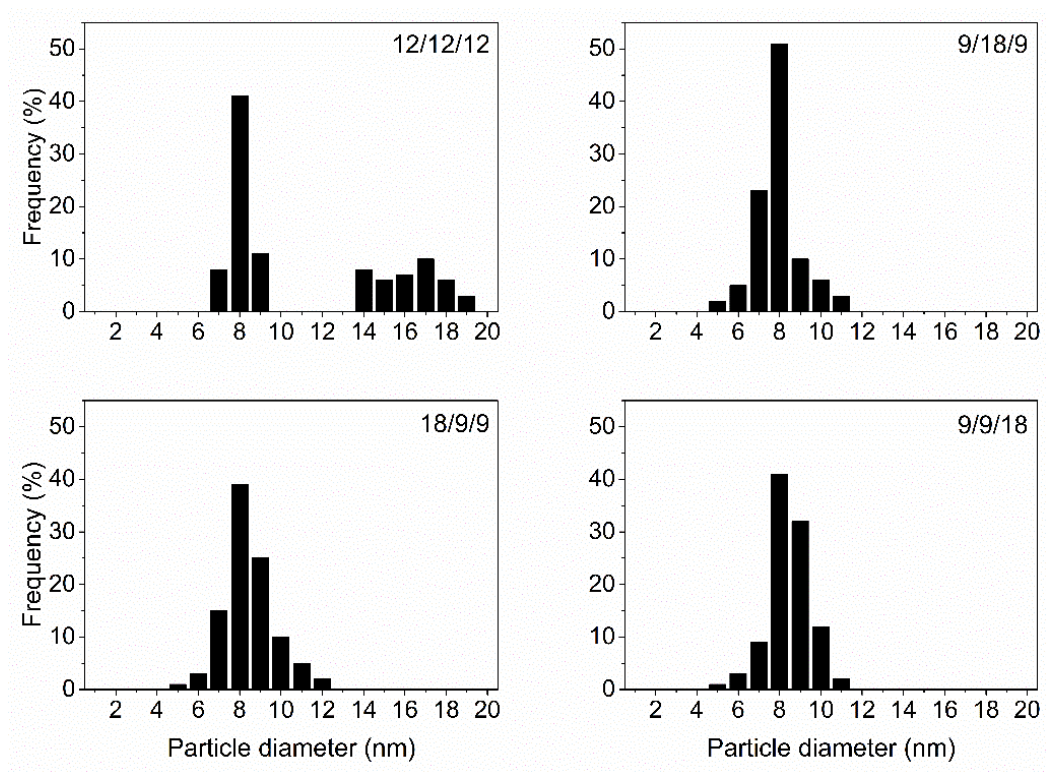


**Figure 4.11.** Distribution of particle sizes of the metal aggregates present in the calcined catalysts.

FeCoCu 12/12/12 gave overlapping peaks at ca. 199 and 210°C, attributed to the reduction of CuO to Cu, Fe<sub>2</sub>O<sub>3</sub> to Fe<sub>3</sub>O<sub>4</sub> and Co<sub>3</sub>O<sub>4</sub> to Co [1]. The wide shoulder from 225 to 450°C corresponded to the consecutive reduction of Fe<sub>3</sub>O<sub>4</sub> to FeO, and finally to metallic Fe [4]. The latter appeared to be hindered in this material when compared to other catalysts, which was probably related to the presence of the bigger metal aggregates. Adding an excess of iron (FeCoCu

18/9/9) caused the peak associated with the reduction of  $\text{Fe}_2\text{O}_3$  to  $\text{Fe}_3\text{O}_4$  to shift to ca.  $184^\circ\text{C}$ , while the peak at  $210^\circ\text{C}$  attributed to the reduction of  $\text{CuO}$  to  $\text{Cu}$  decreased in relative intensity. It may also be observed that the peak at the highest temperature shifted to  $301^\circ\text{C}$  due to the smaller size of the metal particles. When  $\text{Co}$  was in excess (FeCoCu 9/18/9) a clear peak attributed to the reduction of  $\text{Co}^{3+}$  was observed at  $221^\circ\text{C}$ , and the peaks associated with iron shifted to lower temperatures due to less interaction between iron and the support. Finally, when  $\text{Cu}$  was in excess (FeCoCu 9/9/18), a wide peak centered at ca.  $183^\circ\text{C}$  corresponding to overlapped  $\text{Fe}_2\text{O}_3$  and  $\text{CuO}$  reductions was detected, with a small shoulder at ca.  $267^\circ\text{C}$  ( $\text{Fe}_3\text{O}_4$  reduction).

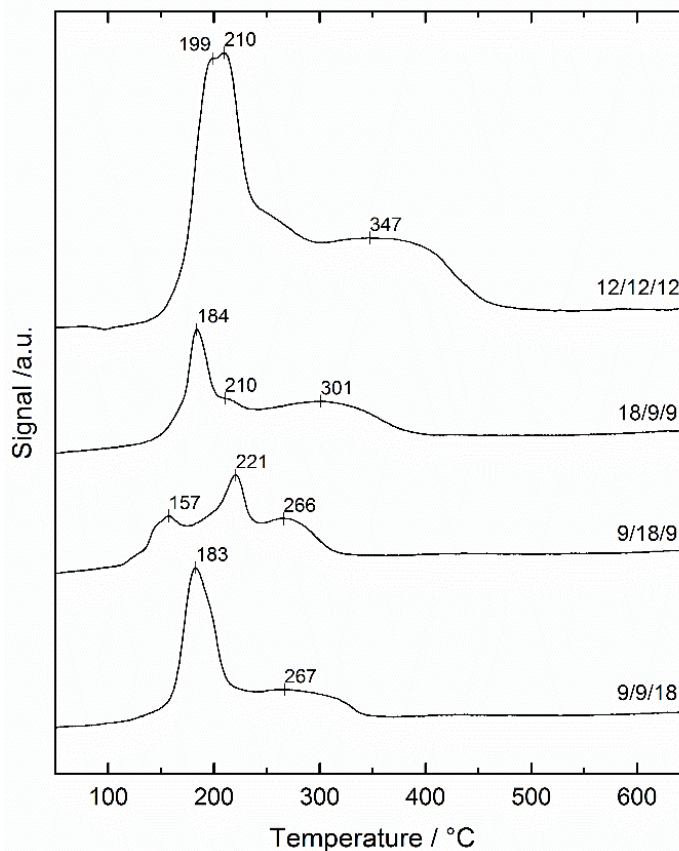


**Figure 4.12.**  $\text{H}_2$  temperature programmed reduction (TPR) profiles of the calcined materials.

Hydrogen consumption was calculated by integration of the TPR reduction profiles and it is reported in Table 4.3. Consumption ratio – the quotient between the actual H<sub>2</sub> consumption and the theoretical consumption for total reduction of the pure metal oxides of the three metals – was always below 1. This may be due to the formation of non-stoichiometric oxides upon calcination, but also indicates that a fraction of the metals probably remained oxidized. In fact, the discrepancy in H<sub>2</sub> consumption was more pronounced in the catalyst with excess of iron, which points to a fraction of this metal remaining in Fe<sub>x</sub>O<sub>y</sub> oxidized forms without being completely reduced to metallic Fe.

#### 4.2.2. Catalyst activity

Figure 4.13 shows the conversion of carbon monoxide and the overall selectivity towards carbon dioxide, hydrocarbons and oxygenated compounds. Carbon balance was better than 95% in all cases. Conversion values varied between 13 and 22%, which was consistent with the reactor pressure and space velocity used in these experiments when compared to previous works in literature [5].

The FeCoCu 12/12/12 catalyst had moderate conversion (21%), low selectivity towards the formation of oxygenated products (11%) and low WGS activity (8.7% CO<sub>2</sub> selectivity). Changing the ratios between the three active metals while maintaining a constant nominal total metal load of 36% influenced activity and selectivity depending on the dominant metal. Using an excess of iron (FeCoCu 18/9/9) did not modify the conversion and selectivity of the catalyst significantly when compared to FeCoCu 12/12/12. It had a conversion of 22% and tended to promote the formation of alkanes (70%) over carbon dioxide (11%) and alcohols (13%), which were statistically equal to those of FeCoCu 12/12/12. When an excess of cobalt was used (FeCoCu 9/18/9) conversion (18%), hydrocarbon selectivity (72%) and carbon dioxide selectivity (7%) were statistically equivalent to those of the base catalyst (FeCoCu 12/12/12), but a significantly higher selectivity to alcohols of 18% was obtained. The catalyst containing an excess of

Cu (FeCoCu 9/9/18) had lower conversion (13%) than the other three materials and a selectivity to oxygenates of 22%, which was significantly higher than FeCoCu 12/12/12 and Fe/Co/Cu 18/9/9. This may be attributed to the role of Cu as promoter of the associative adsorption of CO, its insertion, and the dissociative chemisorption of H<sub>2</sub>, which leads to the formation of alcohols and oxygenated products.

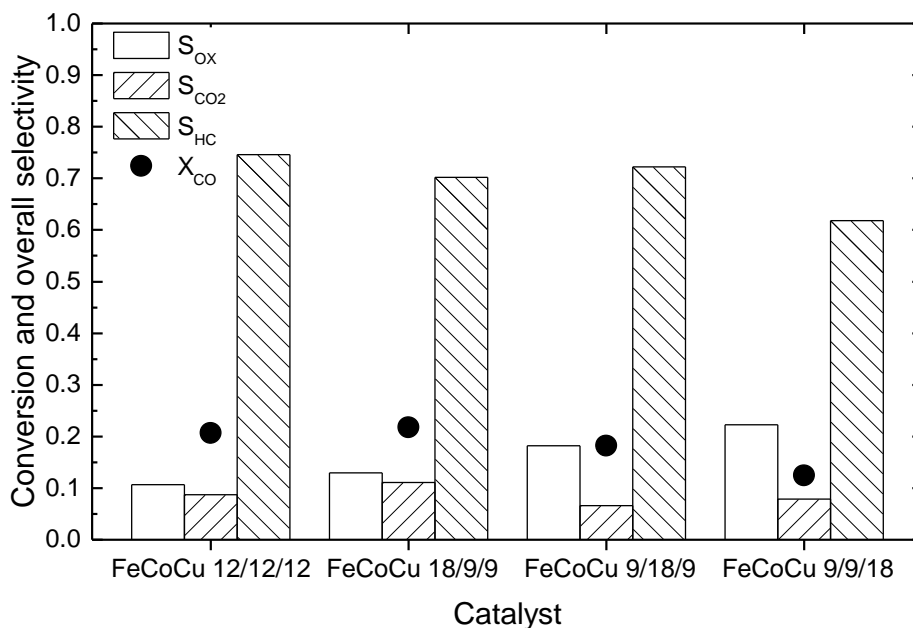


**Figure 4.13.** Conversion and selectivity of ternary catalysts after 24 hours of reaction (30 bar, 300°C, WHSV = 0.3 mol<sub>CO</sub>/g<sub>cat</sub>·h, H<sub>2</sub>/CO = 2).

Overall, conversion and selectivity towards the formation of oxygenated products were consistent with previous studies, although lower pressures were investigated herein. Guo et al. [6] studied the activity of ternary FeCoCu catalysts supported in attapulgite at 350°C and 55 bar using a feed gas with a CO/H<sub>2</sub> molar ratio of 2. Conversions from 65 to 70% were reported – mainly due to the enhanced activity at higher pressure and temperature – but moderate alcohol selectivity (from 6 to 12%) and high carbon dioxide formation (18 to 20%) were

reported. Sharma et al. [7] performed experiments at 28 bar and 300°C using binary FeCu catalysts doped with potassium. CO conversion was ca. 13% but the selectivity towards alcohols was only 2%. Higher alcohol selectivity (close to 40%) was reported for CoCuO-La catalysts at 30 bar and 330°C at 30% CO conversion [8], which was attributed to the effect of La as a promoter. This work on ternary catalysts shows moderate improvements over previous work using binary catalysts [9]. In comparison with binary catalysts, similar levels of conversion were achieved, but higher selectivity towards alcohols, and improved selectivity towards higher alcohols.

The distribution of individual alcohols and hydrocarbons grouped by carbon number is shown in Table 4.4. Methane was the dominant product in all the catalysts by far with a selectivity ranging from ca. 38 to 44% and it was accompanied by alkanes of up to 5 carbons. Larger hydrocarbons were neither detected in the product gas by the on-line gas chromatograph, nor in the aqueous liquid phase collected in the gas-liquid separator. No organic liquid phase was formed. However, the production of minor amounts of hydrocarbons larger than six carbons could not be ruled out entirely, even if they were not observed in our experimental setup. Oxygenated products comprised alcohols from methanol to n-heptanol, together with trace amounts of aldehydes. Selectivity to methanol and ethanol were similar, with values between ca. 2.3 to 6.2, depending on the catalyst.

The performance of the different catalysts was also assessed on the basis of the chain growth probabilities of the Anderson-Schultz-Flory (ASF) distribution of hydrocarbons ( $\alpha_{HC}$ ) and alcohols ( $\alpha_A$ ), which are shown in Figure 4.14. In all catalysts, higher values of alcohol chain growth probabilities were observed for alcohols larger than 4 carbons ( $\alpha_{A4+}$ ) than for alcohols with less than 4 carbons ( $\alpha_{A1-4}$ ), although this difference was less pronounced in catalyst FeCoCu 9/18/9. This agrees qualitatively with the tendency of Fe-based FT catalysts to present positive deviations in the chain grow probability at high carbon numbers [10].

Table 4.4. Selectivity ( $S_j$ ) to alcohols and hydrocarbons by carbon number

	FeCoCu 12/12/12	FeCoCu 18/9/9	FeCoCu 9/18/9	FeCoCu 9/9/18
<b>Alcohols</b>				
C <sub>1</sub>	$2.27 \cdot 10^{-2}$	$3.14 \cdot 10^{-2}$	$3.11 \cdot 10^{-2}$	$6.17 \cdot 10^{-2}$
C <sub>2</sub>	$2.37 \cdot 10^{-2}$	$2.93 \cdot 10^{-2}$	$4.03 \cdot 10^{-2}$	$5.03 \cdot 10^{-2}$
C <sub>3</sub>	$1.20 \cdot 10^{-2}$	$1.31 \cdot 10^{-2}$	$2.35 \cdot 10^{-2}$	$2.59 \cdot 10^{-2}$
C <sub>4</sub>	$8.21 \cdot 10^{-3}$	$8.22 \cdot 10^{-3}$	$1.62 \cdot 10^{-2}$	$1.62 \cdot 10^{-2}$
C <sub>5</sub>	$8.83 \cdot 10^{-3}$	$8.30 \cdot 10^{-3}$	$1.79 \cdot 10^{-2}$	$1.67 \cdot 10^{-2}$
C <sub>6</sub>	$6.50 \cdot 10^{-3}$	$7.82 \cdot 10^{-3}$	$1.31 \cdot 10^{-2}$	$1.51 \cdot 10^{-2}$
C <sub>7</sub>	$5.31 \cdot 10^{-3}$	$6.51 \cdot 10^{-3}$	$7.53 \cdot 10^{-3}$	$1.32 \cdot 10^{-2}$
<b>Hydrocarbons</b>				
C <sub>1</sub>	$4.36 \cdot 10^{-1}$	$3.78 \cdot 10^{-1}$	$3.88 \cdot 10^{-1}$	$4.23 \cdot 10^{-1}$
C <sub>2</sub>	$1.15 \cdot 10^{-1}$	$1.52 \cdot 10^{-1}$	$1.22 \cdot 10^{-1}$	$1.40 \cdot 10^{-1}$
C <sub>3</sub>	$8.60 \cdot 10^{-2}$	$1.07 \cdot 10^{-1}$	$1.08 \cdot 10^{-1}$	$9.01 \cdot 10^{-3}$
C <sub>4</sub>	$4.16 \cdot 10^{-2}$	$3.91 \cdot 10^{-2}$	$5.25 \cdot 10^{-2}$	$4.39 \cdot 10^{-2}$
C <sub>5</sub>	$6.72 \cdot 10^{-2}$	$2.63 \cdot 10^{-2}$	$5.17 \cdot 10^{-2}$	$1.94 \cdot 10^{-3}$

A few trends may be inferred from data in Table 4.4 and Figure 4.14 regarding the influence of catalyst composition. FeCoCu 12/12/12 had alcohol and hydrocarbon chain growth probabilities of 0.44 ( $\alpha_{A1-4}$ ) and 0.71 ( $\alpha_{A4+}$ ), and 0.42 ( $\alpha_{HC}$ ), respectively. An excess of cobalt (FeCoCu 9/18/9) had no significant influence on the hydrocarbon and alcohol chain growth probabilities. Using an excess of iron (FeCoCu 18/9/9) caused no discernible change in  $\alpha_{HC}$  and  $\alpha_{A1-4}$ , but  $\alpha_{A4+}$  (0.77) was significantly higher than for FeCoCu 12/12/12 and 9/18/9, thus improving selectivity to higher alcohols.

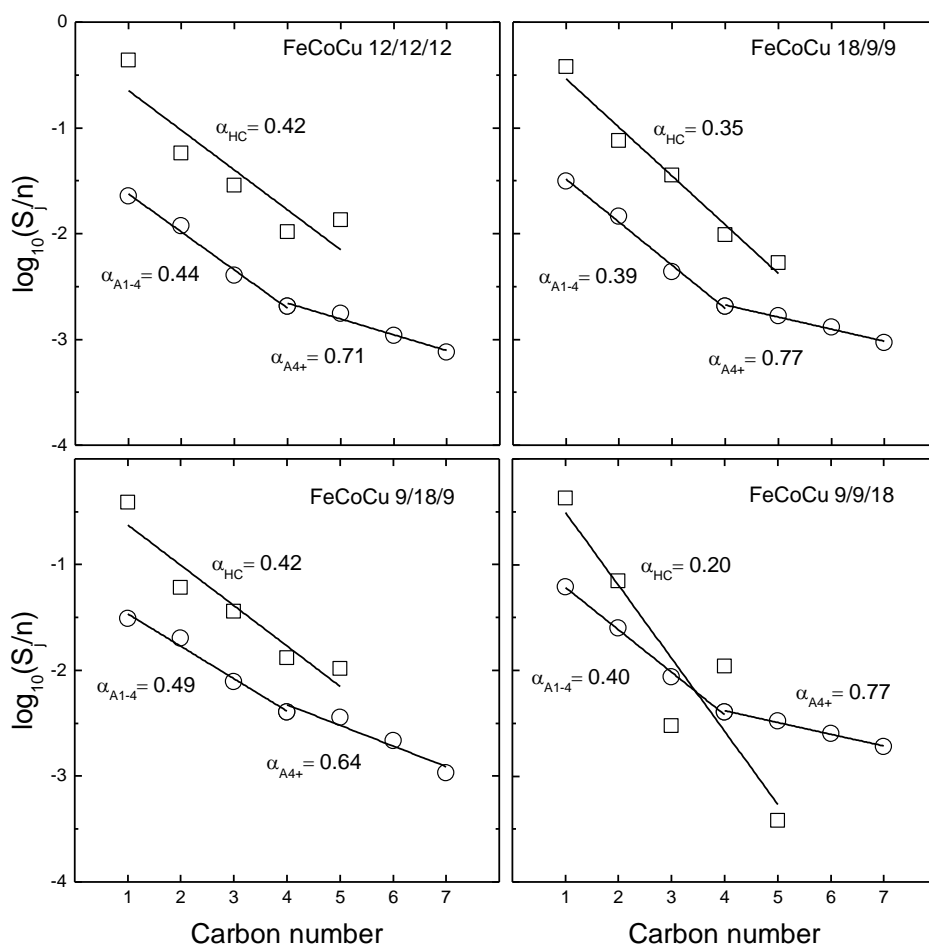


**Figure 4.14.** Comparison of ASF plots of the ternary catalysts after 24 hours of reaction (Same conditions than Figure 4.13. Hydrocarbons,  $\square$ ; Alcohols,  $\circ$ ).

Finally, using an excess of copper had an important effect on the catalyst behavior (FeCoCu 9/9/18), mainly by reducing the hydrocarbon growth probability to 0.20, which roughly is half the value observed in all the other catalysts. Although methane was still the main product, the excess of copper hindered the capacity of chain growth in hydrocarbons while maintaining the capacity of chain growth to higher alcohols at the same value than FeCoCu 18/9/9. The different chain growth probabilities in comparison with the other

catalysts tested indicate that FeCoCu 9/9/18 seems to promote CO insertion to retain C-O bonds for alcohol chain termination and to reduce direct H<sub>2</sub> insertion for hydrocarbon chain termination. Therefore, despite FeCoCu 9/9/18 was the less active catalyst (ca. 13% conversion), it had the better performance for alcohols synthesis (20% selectivity) and it also produced a relatively low amount of carbon dioxide.

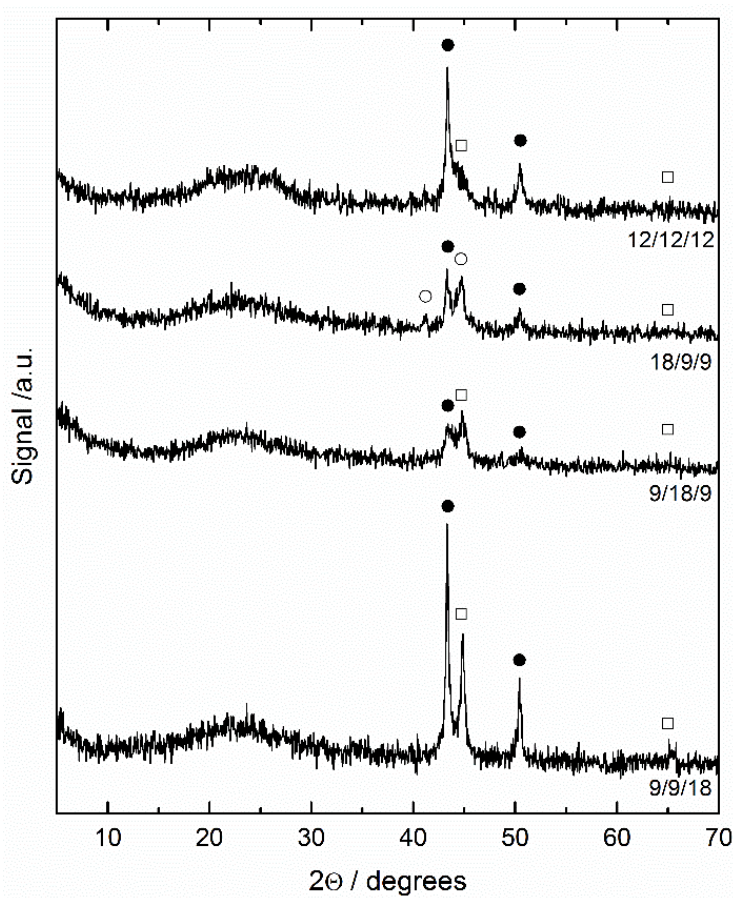


**Figure 4.15.** Diffractograms of the spent catalysts. Crystalline phases: (□) Fe, (●) Cu, (○) Fe<sub>5</sub>C<sub>2</sub>.

### 4.2.3. Characterization of the spent catalysts

Figure 4.15 shows X-ray diffraction patterns of the spent catalysts after 24 hours of reaction at 30 bar and 300°C. The two main peaks corresponded to metallic copper and iron. During the reaction, Fe and Cu remained in their metallic phases, with reduced levels of crystallinity, which may indicate a partial oxidation of the metals. Catalyst FeCoCu 18/9/9-U also showed the presence of iron carbide ( $\text{Fe}_5\text{C}_2$ ), which is considered an active center that produces hydrocarbons in FTS [11] together with metallic Cu, which is an active center for hydrocarbons and methanol production. The presence of iron carbide could only be appreciated in the sample with the highest iron content, but its presence in the other catalysts could not be discarded due to the low crystallinity of the  $\text{Fe}_5\text{C}_2$  phase. Regarding average crystallite sizes, Fe showed a slight increase from ca. 5 to 6.6-7.8 nm, while Cu raised its crystallite size from 3.2-4 to 11.0-13.4 nm. These results indicate that metal particles aggregated/sintered during the reaction. Catalyst FeCoCu 9/9/18-U showed the highest crystallinity for  $\alpha$ -Fe. FeCoCu 18/9/9-U and FeCoCu 9/18/9-U had lower presence of that phase due to the presence of iron carbide and the low-crystallinity of cobalt and iron when dispersed on the support. All used samples showed a characteristic peak centered at 22°, corresponding to carbon deposition.

Figure 4.16 shows the TEM images of the spent catalysts after 24 hours of reaction. Significant differences could be observed with respect to the activated catalysts. Most materials showed the presence of agglomerates of ca. 10-50 nm in diameter distributed outside the mesoporous structure of the SBA-15 support, which were probably caused by sintering of the metal particles during reaction. In fact, the filamentous aggregates that were observed inside the SBA-15 channels in the fresh samples of catalysts FeCoCu 12/12/12 and FeCoCu 9/18/9, disappeared completely after reaction. FeCoCu 12/12/12-U and FeCoCu 9/18/9-U still maintained small metal particles inside the channels, but it also showed the formation of larger aggregates of ca. 10-30 nm deposited on the outer

surface of the SBA-15 particles. Catalysts with good dispersion of small metal particles before reaction (FeCoCu 18/9/9 and FeCoCu 9/9/18) displayed different situations after use. In FeCoCu 18/9/9-U small particles were still distributed inside the channels, but a few larger aggregates were present on the outer surface of SBA-15. FeCoCu 9/9/18-U showed no aggregates although the particles deposited inside the SBA-15 structure appeared to be slightly larger than in the fresh catalyst. Overall, these observations were in agreement with the increased average crystallite size determined by XRD of the spent catalysts. Furthermore, spent catalysts had a 10% decrease in BET surface area, as well as a 50-60% decrease in micropore volume (not shown), which could be attributed to the effects of sintering and eventually coke deposition.

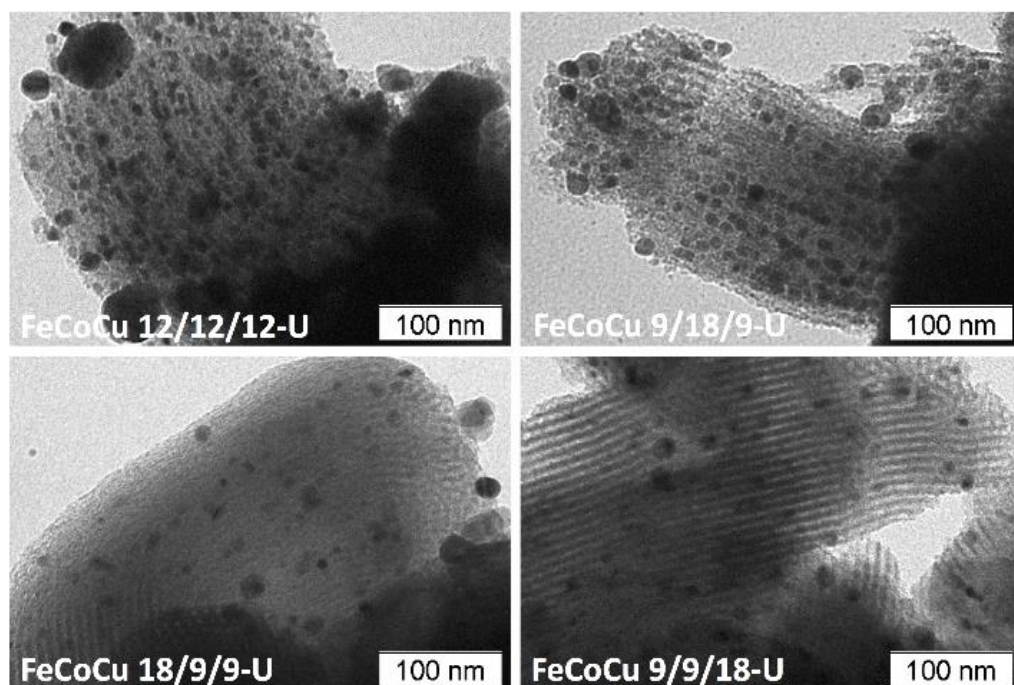
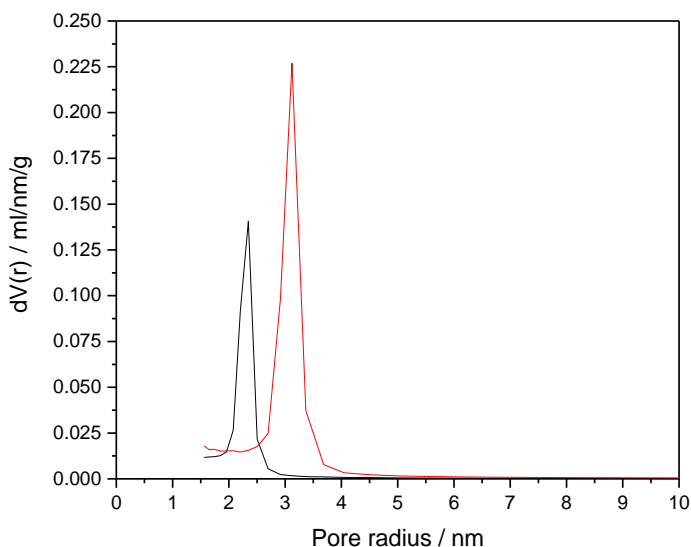


**Figure 4.16.** TEM images of the spent catalysts.

### 4.3. FeCoCu 9/9/18: influence of reaction conditions and alkaline doping.

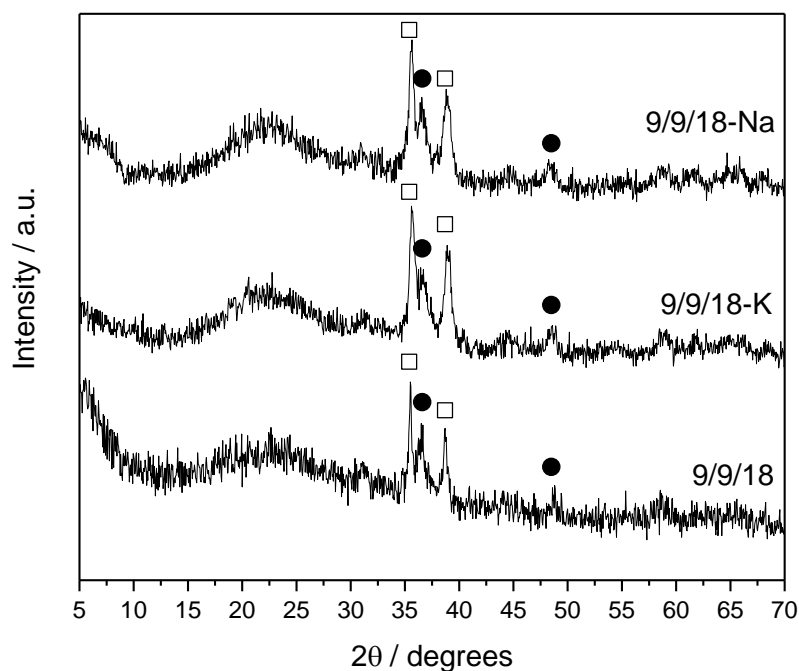
#### 4.3.1. Characterization of fresh catalysts

The metal load of the catalyst was determined by ICP-OES, and showed a content of 8.3 wt.% Fe, 8.4 wt.% Co, and 18.9 wt.% Cu, in accordance to the nominal load of the three metals. Doped catalysts showed a 1.1 wt.% of Na and 1.0 wt.% of K, respectively. This material showed type-H1 hysteresis, which corresponds to mesoporous materials with cylindrical mesostructures, as is SBA-15. The FeCoCu catalyst had a BET surface area of 496 m<sup>2</sup>/g, with a micropore volume of 0.066 ml/g, and a total pore volume of 0.577 ml/g. Figure 4.17 shows the average pore size distribution. Commercial SBA-15 had its maximum at a diameter of 6.75 nm, and FeCoCu catalysts had an average pore size of 4.56 nm. Comparing commercial SBA-15 with SBA-15 9/9/18, a pore volume reduction was observed, which can be attributed to the insertion of metallic nanoparticles inside the SBA-15 channels.



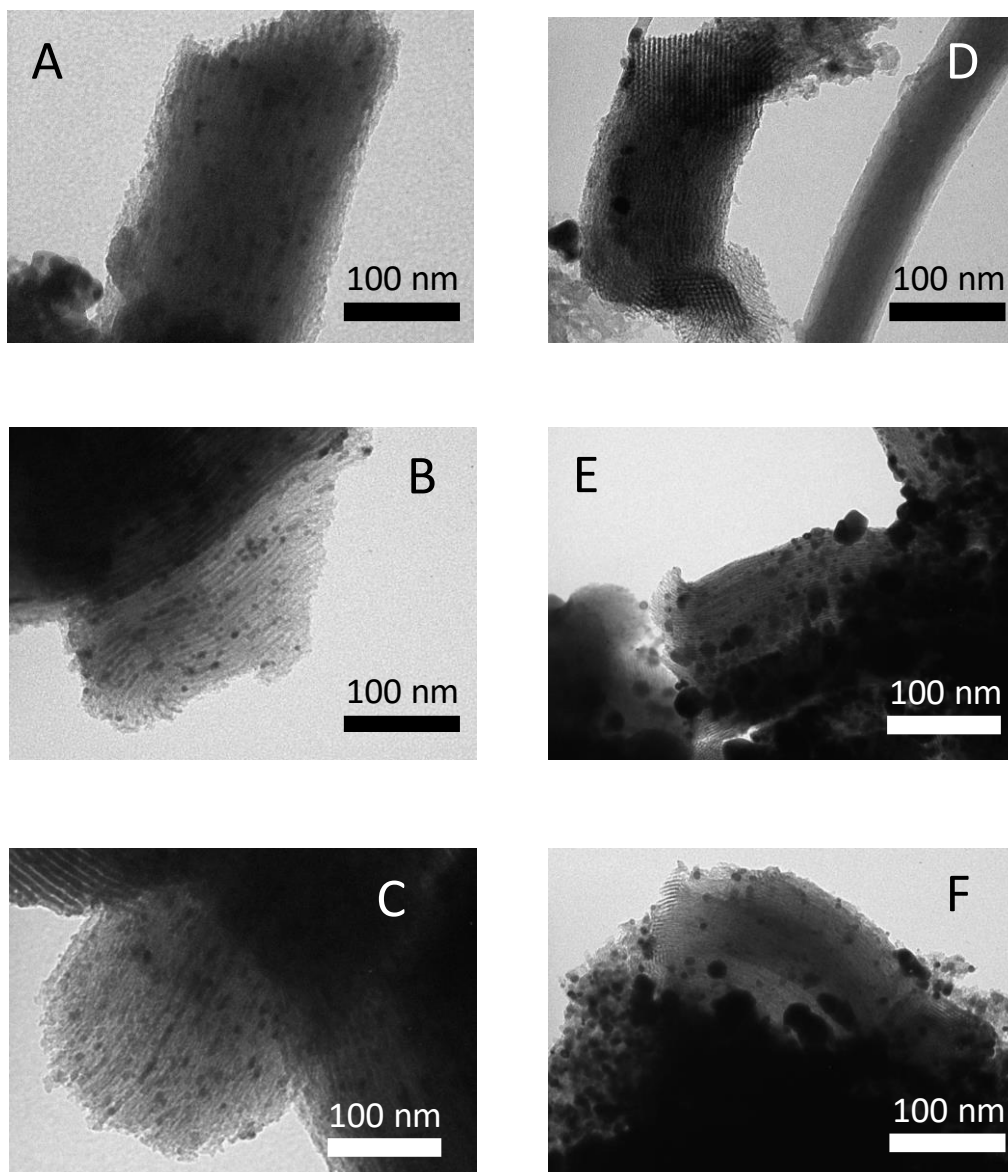
**Figure 4.17.** Pore size distribution of SBA-15 9/9/18. Red line: commercial SBA-15. Black line: SBA-15 9/9/18.

Figure 4.18 shows the X-ray diffractogram of the calcined catalysts. The diffractogram showed characteristic peaks for metallic Fe oxides and Cu oxides. Co oxides showed no crystalline phases. Average crystallite sizes for Fe and Cu were 7.8 nm and 12.3 nm, respectively. Due to its low crystallinity, Co crystallite size was too small to be measured. Doped catalysts did not display any additional peaks, which indicated that K and Na were in non-crystalline phases. Besides, no significant changes in crystallinity were observed upon impregnation with the alkaline salts.



**Figure 4.18.** XRD of calcined catalysts. Crystalline phases: (□) Fe, (●) Cu.

Figure 4.19 shows TEM imaging of the calcined and used catalysts. The morphology of SBA-15 could be observed, which consisted of long, regular channels of 9 nm of diameter. Metallic clusters of 7-9 nm of diameter were found inside the channels. K- and Na- doped catalysts showed the same structure, with small metallic clusters inside the SBA-15 channels.



**Figure 4.19.** TEM imaging of (A) fresh SBA-15 9/9/18, (B) fresh SBA-15 9/9/18-Na, (C) fresh SBA-15 9/9/18-K, (D) used SBA-15 9/9/18 after 96 h of reaction at 360°C, (E) used SBA-15 9/9/18-Na after 24 h of reaction at 300°C, (F) used SBA-15 9/9/18-K after 24 h of reaction at 360°C.

### 4.3.2. Influence of reaction conditions

#### Effect of temperature of reaction

Figures 4.20, 4.21, and table 4.5 report the values of conversion and selectivity for the different products using SBA-15 9/9/18 at 300°C, 330°C, and 360°C, for 96 h of reaction, as well as the ASF plots for hydrocarbons and alcohols. As it can be seen, after 24 hours of reaction at 300°C the catalyst had moderate activity (CO conversion of 14%), with low WGS selectivity (4%), high selectivity towards hydrocarbons (66%), and moderate selectivity towards alcohols (23%). After 48 hours of reaction, a slight decrease in activity was noticed (13%), with a slight decrease in hydrocarbon selectivity (64%), and a subsequent increase in alcohol selectivity (25%), as well as a slight increase in WGS activity (6%). These changes were amplified after 72 and 96 hours of reaction, with further catalyst deactivation (11% and 9% of CO conversion, respectively), and an increase in alcohol selectivity (28% and 30%, respectively), at the expense of hydrocarbon selectivity (62% and 56%, respectively).

Regarding product distribution, the main hydrocarbon produced was methane, with selectivity increasing over time from 47% to 53% (Table 4.5). Heavier hydrocarbons (from C<sub>2</sub> to C<sub>5</sub>) showed decreasing selectivity over time (from 19% to 3%). Methanol was the main alcohol produced (6% to 15%), followed by ethanol (5% to 8%), and those two alcohols comprised the majority of the increase in selectivity over time. These results suggest a deactivation of the Fe and Co active centers, which produced a decrease of catalyst activity, as well as an increase in the selectivity to lighter hydrocarbon. The Cu active center exhibited lower deactivation, which explained the increased selectivity towards the formation of alcohols.

### Higher Alcohol Synthesis: Effect of metal load and reaction conditions

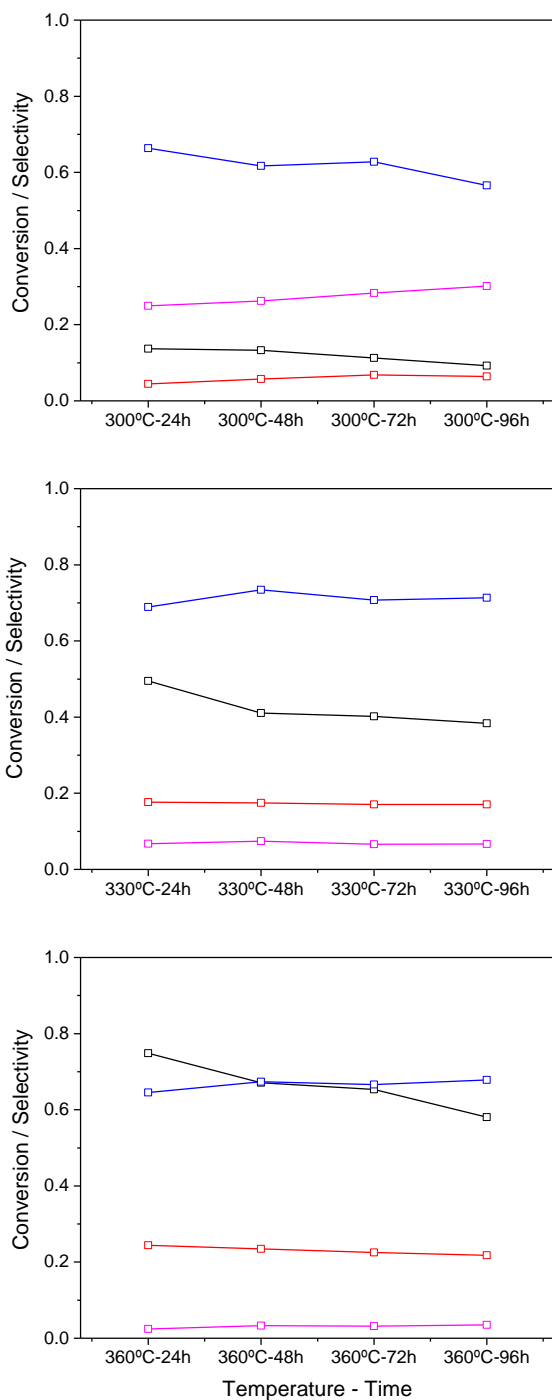


**Figure 4.20.** Conversion and selectivity at different temperatures at 24, 48, 72, and 96 h of reaction. Top: 300°C, middle: 330°C, bottom: 360°C. Black: CO conversion, red: CO<sub>2</sub> selectivity blue: HC selectivity, pink: alcohols selectivity.

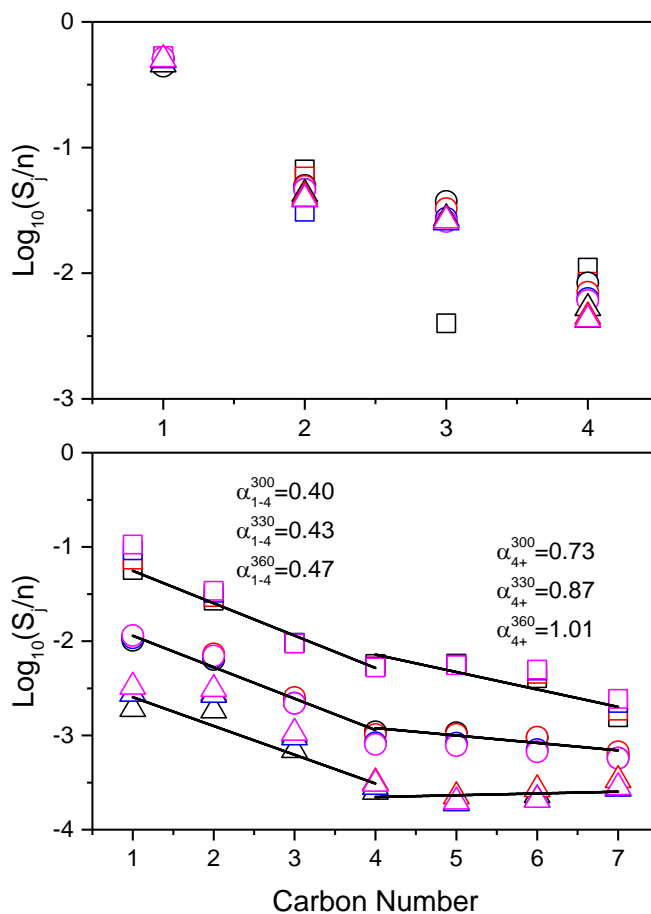


**Figure 4.21.** Chain propagation probability for hydrocarbons and alcohols at different temperatures of reaction. Top graph: hydrocarbons. Bottom graph: alcohols. Black: 24h; Red: 48h; Blue: 72h; Magenta: 96h. Square: 300°C; Circle: 330°C; Triangle: 360°C.

At 330°C there was a significant increase of conversion (50%) with increased selectivity towards CO<sub>2</sub> (18%) and hydrocarbons (69%), and decreased selectivity towards alcohols (5%). At this temperature, the deactivation effect of the catalyst was more pronounced since conversion descended to 38% after 96 hours of reaction, but without significant differences in global selectivity.

**Table 4.5.** Selectivity towards hydrocarbons and alcohols at different temperatures.

	300°C-24h	300°C-48h	300°C-72h	300°C-96h
C <sub>1</sub> HC	$4.73 \cdot 10^{-1}$	$4.66 \cdot 10^{-1}$	$5.33 \cdot 10^{-1}$	$5.34 \cdot 10^{-1}$
C <sub>2</sub> HC	$1.34 \cdot 10^{-1}$	$1.18 \cdot 10^{-1}$	$6.16 \cdot 10^{-2}$	0.00
C <sub>3</sub> HC	$1.20 \cdot 10^{-2}$	0.00	0.00	0.00
C <sub>4</sub> HC	$4.43 \cdot 10^{-2}$	$3.41 \cdot 10^{-2}$	$3.29 \cdot 10^{-2}$	$3.17 \cdot 10^{-2}$
C <sub>5</sub> HC	0.00	0.00	0.00	0.00
C <sub>1</sub> OH	$5.68 \cdot 10^{-2}$	$7.33 \cdot 10^{-2}$	$9.18 \cdot 10^{-2}$	$1.06 \cdot 10^{-1}$
C <sub>2</sub> OH	$5.36 \cdot 10^{-2}$	$5.86 \cdot 10^{-2}$	$6.51 \cdot 10^{-2}$	$6.85 \cdot 10^{-2}$
C <sub>3</sub> OH	$2.88 \cdot 10^{-2}$	$2.85 \cdot 10^{-2}$	$2.88 \cdot 10^{-2}$	$2.84 \cdot 10^{-2}$
C <sub>4</sub> OH	$2.29 \cdot 10^{-2}$	$2.16 \cdot 10^{-2}$	$2.14 \cdot 10^{-2}$	$2.10 \cdot 10^{-2}$
C <sub>5</sub> OH	$2.89 \cdot 10^{-2}$	$2.80 \cdot 10^{-2}$	$2.81 \cdot 10^{-2}$	$2.77 \cdot 10^{-2}$
C <sub>6</sub> OH	$2.43 \cdot 10^{-2}$	$2.70 \cdot 10^{-2}$	$2.92 \cdot 10^{-2}$	$2.99 \cdot 10^{-2}$
C <sub>7</sub> OH	$1.09 \cdot 10^{-2}$	$1.28 \cdot 10^{-2}$	$1.54 \cdot 10^{-2}$	$1.70 \cdot 10^{-2}$
	330°C-24h	330°C-48h	330°C-72h	330°C-96h
C <sub>1</sub> HC	$4.44 \cdot 10^{-1}$	$5.10 \cdot 10^{-1}$	$5.07 \cdot 10^{-1}$	$5.19 \cdot 10^{-1}$
C <sub>2</sub> HC	$1.00 \cdot 10^{-1}$	$9.84 \cdot 10^{-2}$	$9.30 \cdot 10^{-2}$	$9.28 \cdot 10^{-2}$
C <sub>3</sub> HC	$1.12 \cdot 10^{-1}$	$9.80 \cdot 10^{-2}$	$8.22 \cdot 10^{-2}$	$7.74 \cdot 10^{-2}$
C <sub>4</sub> HC	$3.34 \cdot 10^{-2}$	$2.82 \cdot 10^{-2}$	$2.51 \cdot 10^{-2}$	$2.42 \cdot 10^{-2}$
C <sub>5</sub> HC	0.00	0.00	0.00	0.00
C <sub>1</sub> OH	$1.02 \cdot 10^{-2}$	$1.13 \cdot 10^{-2}$	$1.08 \cdot 10^{-2}$	$1.15 \cdot 10^{-2}$
C <sub>2</sub> OH	$1.27 \cdot 10^{-2}$	$1.47 \cdot 10^{-2}$	$1.35 \cdot 10^{-2}$	$1.39 \cdot 10^{-2}$
C <sub>3</sub> OH	$7.12 \cdot 10^{-3}$	$7.58 \cdot 10^{-3}$	$6.60 \cdot 10^{-3}$	$6.57 \cdot 10^{-3}$
C <sub>4</sub> OH	$4.37 \cdot 10^{-3}$	$4.09 \cdot 10^{-3}$	$3.34 \cdot 10^{-3}$	$3.21 \cdot 10^{-3}$
C <sub>5</sub> OH	$5.33 \cdot 10^{-3}$	$5.13 \cdot 10^{-3}$	$4.14 \cdot 10^{-3}$	$3.90 \cdot 10^{-3}$
C <sub>6</sub> OH	$5.68 \cdot 10^{-3}$	$5.74 \cdot 10^{-3}$	$4.24 \cdot 10^{-3}$	$4.03 \cdot 10^{-3}$
C <sub>7</sub> OH	$4.34 \cdot 10^{-3}$	$4.69 \cdot 10^{-3}$	$4.03 \cdot 10^{-3}$	$4.01 \cdot 10^{-3}$

**Table 4.5 (contd.).** Selectivity towards hydrocarbons and alcohols at different temperatures.

	360°C-24h	360°C-48h	360°C-72h	360°C-96h
C <sub>1</sub> HC	$4.57 \cdot 10^{-1}$	$4.96 \cdot 10^{-1}$	$4.95 \cdot 10^{-1}$	$5.04 \cdot 10^{-1}$
C <sub>2</sub> HC	$8.53 \cdot 10^{-2}$	$8.10 \cdot 10^{-2}$	$7.75 \cdot 10^{-2}$	$7.80 \cdot 10^{-2}$
C <sub>3</sub> HC	$8.15 \cdot 10^{-2}$	$7.91 \cdot 10^{-2}$	$7.60 \cdot 10^{-2}$	$7.87 \cdot 10^{-2}$
C <sub>4</sub> HC	$2.11 \cdot 10^{-2}$	$1.81 \cdot 10^{-2}$	$1.70 \cdot 10^{-2}$	$1.72 \cdot 10^{-2}$
C <sub>5</sub> HC	0.00	0.00	0.00	0.00
C <sub>1</sub> OH	$1.90 \cdot 10^{-3}$	$2.76 \cdot 10^{-3}$	$2.76 \cdot 10^{-3}$	$3.28 \cdot 10^{-3}$
C <sub>2</sub> OH	$3.67 \cdot 10^{-3}$	$5.62 \cdot 10^{-3}$	$5.38 \cdot 10^{-3}$	$6.20 \cdot 10^{-3}$
C <sub>3</sub> OH	$2.09 \cdot 10^{-3}$	$3.06 \cdot 10^{-3}$	$2.85 \cdot 10^{-3}$	$3.19 \cdot 10^{-3}$
C <sub>4</sub> OH	$1.01 \cdot 10^{-3}$	$1.26 \cdot 10^{-3}$	$1.13 \cdot 10^{-3}$	$1.22 \cdot 10^{-3}$
C <sub>5</sub> OH	$9.74 \cdot 10^{-4}$	$1.12 \cdot 10^{-3}$	$9.51 \cdot 10^{-4}$	$9.90 \cdot 10^{-4}$
C <sub>6</sub> OH	$1.39 \cdot 10^{-3}$	$1.61 \cdot 10^{-3}$	$1.25 \cdot 10^{-3}$	$1.24 \cdot 10^{-3}$
C <sub>7</sub> OH	$1.92 \cdot 10^{-3}$	$2.34 \cdot 10^{-3}$	$1.90 \cdot 10^{-3}$	$1.97 \cdot 10^{-3}$

Regarding hydrocarbon product distribution, methane was the main product obtained (44% of selectivity after 24 hours of reaction), with an increase of its selectivity over time (up to 52% after 96 hours of reaction). The increased methane selectivity was achieved at the expense of a decreased selectivity towards heavier hydrocarbons (from 25% to 19%). These results indicated an increased activity of Fe and active sites, which resulted in increased WGS activity, and decreased activity of Cu, and a lower selectivity towards alcohols.

Results at 360°C were similar to those at 330°C, with an even greater CO conversion (75%), WGS activity (24%), and slightly lower hydrocarbon (65%) and alcohol selectivity (1%). This was in concordance with the experiments at 330°C, and points to an increased activity of Fe active sites and a decreased activity of Cu active sites. The deactivation effect was also more intense over

time, with a final conversion value of 58% but without significant changes in product distribution.

Work from Zhang et al. [12] using supported Fe catalysts showed a similar effect with the increase in temperature. In Zhang's tests when temperature was taken from 260°C to 300°C conversion increased from 83% to 90%. WGS activity grew as well since CO<sub>2</sub> selectivity increased from 65% to 72%. These results also showed that an increase in temperature results in increased catalytic activity over Fe sites. Work from Torres Galvis et al. [13] also showed a similar effect of temperature. Reactions at 340°C and 20 bar had high levels of CO conversion (over 75%), with low selectivity towards alcohols (below 10%).

Chain lengthening probability of alcohols was divided in two subsets: alcohols from 1 to 4 carbons and alcohols with 4 or more carbons. Their values at the different temperatures were similar over the entire time of reaction, with the average values for chain lengthening probability increasing with the increase of temperature. This effect was more pronounced in C4+ alcohols, with the highest values at 360°C. These results indicate that higher reaction temperatures result in more active Fe sites, thus leading to higher conversion values, higher WGS activity, and high selectivity towards hydrocarbons. The increase in temperature was not favorable for alcohol production and inhibited the activity of the Cu active centers.

### Effect of contact time

Figure 4.22 shows the results of the catalytic tests with the variation in contact time,  $\tau$ . This parameter was defined as the ratio between the mass of catalyst and the molar flow rate of carbon monoxide and is basically the inverse of the Weight Hourly Space Velocity (WHSV).

$$\tau \left[ \frac{h \text{ g}_{catalyst}}{mol_{CO}} \right] = \frac{m_{catalyst}}{F_{CO,0}} \quad (4.1)$$

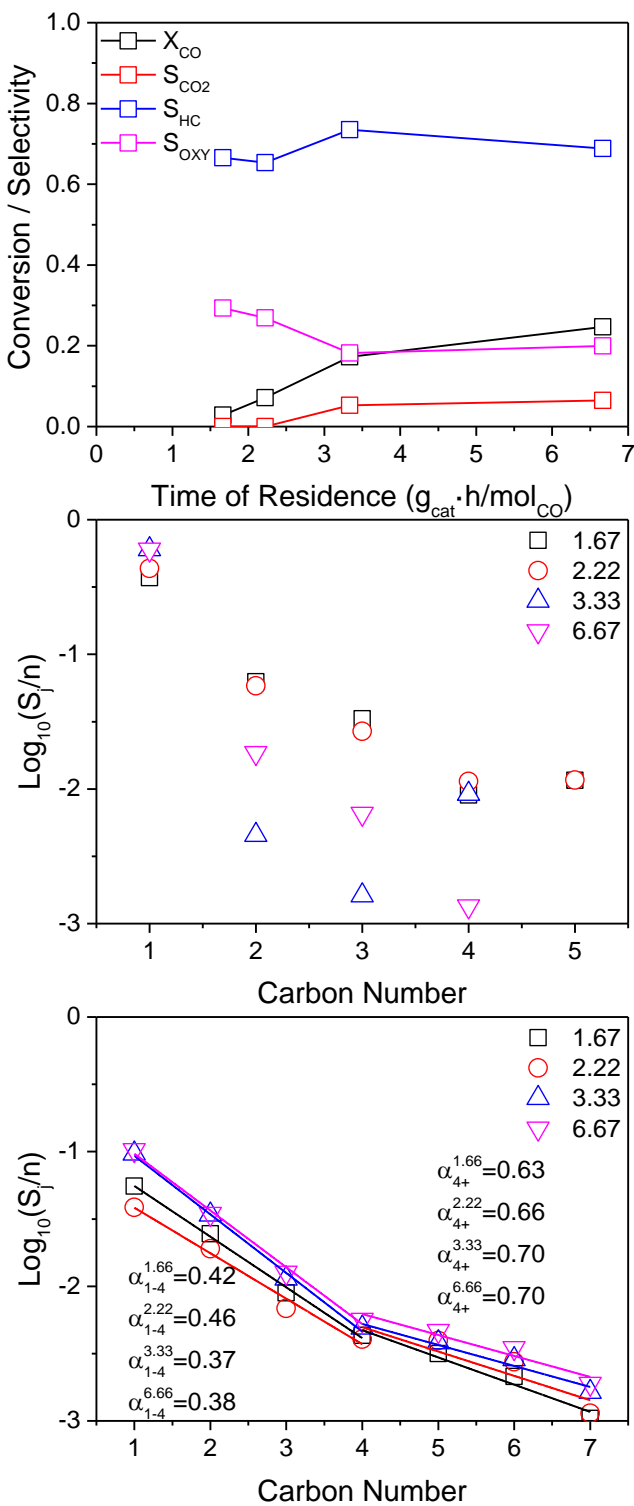


**Figure 4.22.** Conversion, selectivity, and chain growth probability at different contact times. Top graph: conversion and selectivity; middle graph: hydrocarbon chain growth probability; bottom graph: alcohol chain growth probability.

Higher Alcohol Synthesis: Effect of metal load and reaction conditions

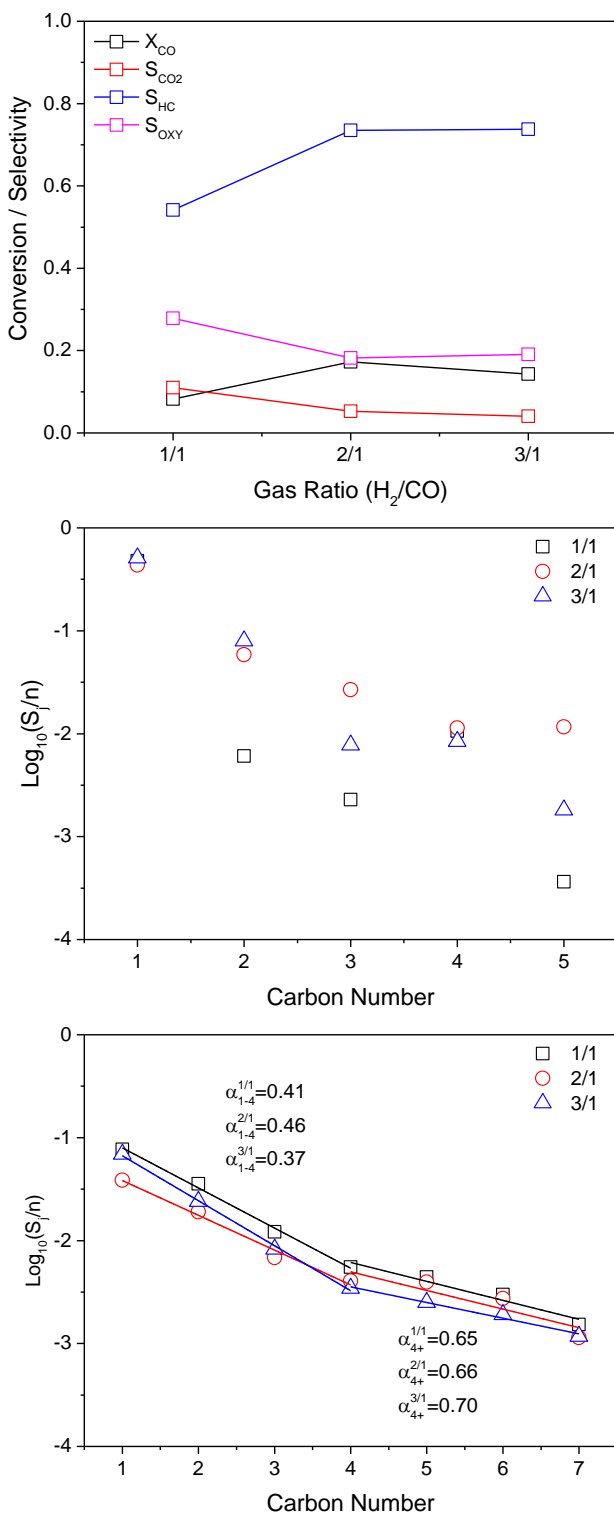


**Figure 4.23.** Conversion, selectivity, and chain growth probability at different gas ratios. Top graph: conversion and selectivity; middle graph: hydrocarbon chain growth probability; bottom graph: alcohol chain growth probability.

Increasing contact time had noticeable effects on CO conversion which increased steadily from 3% at  $1.67 \text{ g}_{\text{cat}}\cdot\text{h} / \text{mol}_{\text{CO}}$  to 25% at  $6.67 \text{ g}_{\text{cat}}\cdot\text{h} / \text{mol}_{\text{CO}}$ . Regarding hydrocarbon selectivity, there was a slight increase with increasing contact times (from 67% at  $1.67 \text{ g}_{\text{cat}}\cdot\text{h} / \text{mol}_{\text{CO}}$  to 69% at  $6.67 \text{ g}_{\text{cat}}\cdot\text{h} / \text{mol}_{\text{CO}}$ ), with a noticeable decrease in methane selectivity (from 60% at  $1.67 \text{ g}_{\text{cat}}\cdot\text{h} / \text{mol}_{\text{CO}}$  to 37% at  $6.67 \text{ g}_{\text{cat}}\cdot\text{h} / \text{mol}_{\text{CO}}$ ), and a corresponding increase in heavier hydrocarbons (from 7% at  $1.67 \text{ g}_{\text{cat}}\cdot\text{h} / \text{mol}_{\text{CO}}$  to 32% at  $6.67 \text{ g}_{\text{cat}}\cdot\text{h} / \text{mol}_{\text{CO}}$ ). There was no noticeable WGS activity at low contact times ( $1.67$  and  $2.22 \text{ g}_{\text{cat}}\cdot\text{h} / \text{mol}_{\text{CO}}$ ), with  $\text{CO}_2$  only appearing at higher contact times (5.3% at  $3.33 \text{ g}_{\text{cat}}\cdot\text{h} / \text{mol}_{\text{CO}}$  and 6.5% at  $6.67 \text{ g}_{\text{cat}}\cdot\text{h} / \text{mol}_{\text{CO}}$ ). Alcohol selectivity showed a moderate decrease with extended contact times (from 29% at  $1.67 \text{ g}_{\text{cat}}\cdot\text{h} / \text{mol}_{\text{CO}}$  to 18% at  $6.67 \text{ g}_{\text{cat}}\cdot\text{h} / \text{mol}_{\text{CO}}$ ). In all cases methanol and ethanol comprised the majority of produced alcohols. These results indicate that low contact times favor Cu activity, resulting in higher alcohol selectivity, albeit at low conversion values. Longer contact times show increased Fe activity, which results in higher conversion values, as well as the appearance of WGS activity.

Chain growth propagation showed a small decrease in growth probability with increased contact time for  $\text{C}_1\text{-C}_4$  alcohols, along with a slight increase in chain growth probability for  $\text{C}_{4+}$  alcohols at higher contact times. This indicates that heavier alcohols tended to form as the reacting mixture advanced through the catalyst bed, as they experienced more interaction with active sites.

### Effect of $\text{H}_2/\text{CO}$ feed ratio

Figure 4.23 and Table 4.6 show the results of the tests performed at different  $\text{H}_2/\text{CO}$  feed ratios. The reaction performed below stoichiometric ratio showed lower conversion values of around 8%, as well as higher WGS activity (11%), coupled with moderate hydrocarbon selectivity (54%), and higher alcohol selectivity (26%). In contrast, the test performed at a 3/1  $\text{H}_2/\text{CO}$  ratio showed results similar to those of the stoichiometric ratio: slightly lower CO conversion (14%), with similar values of hydrocarbon, alcohol and  $\text{CO}_2$  selectivity (74%, 19%,

and 4%, respectively). Regarding individual product selectivity, in all cases methane was the hydrocarbon with the highest selectivity, and methanol and ethanol the most produced alcohols. Regarding chain growth probability, stoichiometric ratio exhibited improved probability for alcohols between 1-4 C (0.46), whereas chain growth probability for 4-7 C alcohols was similar at all reaction conditions (0.65-0.70).

These results show that below stoichiometric conditions, CO conversion decreases, with an increase in alcohol selectivity. This indicates that Fe and Co active sites are hindered by the lack of H<sub>2</sub>, whereas Cu active sites remain more active. In contrast, an excess of H<sub>2</sub> does not show drastic changes in product selectivity and activity.

**Table 4.6.** Selectivity towards hydrocarbons and alcohols at different gas ratios.

Selectivity	1/1	2/1	3/1
Hydrocarbons			
C <sub>1</sub>	4.78·10 <sup>-1</sup>	4.34·10 <sup>-1</sup>	5.12·10 <sup>-1</sup>
C <sub>2</sub>	1.21·10 <sup>-2</sup>	1.17·10 <sup>-1</sup>	1.60·10 <sup>-1</sup>
C <sub>3</sub>	6.85·10 <sup>-3</sup>	8.03·10 <sup>-2</sup>	2.33·10 <sup>-2</sup>
C <sub>4</sub>	4.24·10 <sup>-2</sup>	4.55·10 <sup>-2</sup>	3.37·10 <sup>-2</sup>
C <sub>5</sub>	1.82·10 <sup>-3</sup>	5.82·10 <sup>-2</sup>	9.10·10 <sup>-3</sup>
Alcohols			
C <sub>1</sub> OH	7.69·10 <sup>-2</sup>	3.85·10 <sup>-2</sup>	6.92·10 <sup>-2</sup>
C <sub>2</sub> OH	7.14·10 <sup>-2</sup>	3.80·10 <sup>-2</sup>	4.80·10 <sup>-2</sup>
C <sub>3</sub> OH	3.65·10 <sup>-2</sup>	2.05·10 <sup>-2</sup>	2.48·10 <sup>-2</sup>
C <sub>4</sub> OH	2.21·10 <sup>-2</sup>	1.62·10 <sup>-2</sup>	1.38·10 <sup>-2</sup>
C <sub>5</sub> OH	2.20·10 <sup>-2</sup>	1.98·10 <sup>-2</sup>	1.26·10 <sup>-2</sup>
C <sub>6</sub> OH	1.79·10 <sup>-2</sup>	1.65·10 <sup>-2</sup>	1.15·10 <sup>-2</sup>
C <sub>7</sub> OH	1.07·10 <sup>-2</sup>	7.98·10 <sup>-3</sup>	8.22·10 <sup>-3</sup>

### 4.3.3. Alkaline doping

Alkaline doping was performed with 1% Na and 1% K added to the FeCoCu 9/9/18 catalyst. Figure 4.24 shows the results of the activity experiments. In both cases similar trends were observed: a decrease in CO conversion (10% and 6%, respectively), and a significant increase in CO<sub>2</sub> and alcohol selectivity (25% and 34% for K-doped catalyst), with the corresponding decrease in hydrocarbon selectivity (from 73% in undoped catalyst to 40% for 9/9/18-K). It is worth noting that in both doping tests, the alcohols with highest selectivity were ethanol, propanol and butanol, showing a shift towards higher alcohol production compared to the non-doped catalyst.

The chain growth probability for alcohols shows similar values of C<sub>2</sub>-C<sub>4</sub> alcohols, with a slight decrease in growth probability of C<sub>4+</sub> alcohols in the doped catalysts.

The effect of alkaline metals can be compared with the work of Ishida et al. [14], who studied Co catalysts doped with alkaline metals. The addition of 4% Na and K resulted in increased CO conversion (from 65% undoped to 76% and 83% with Na and K, respectively). CO<sub>2</sub> selectivity was greatly enhanced and there was a significant increase in alcohol selectivity, especially with Na (14.6%). This rise in selectivity was coupled with a decrease in hydrocarbon selectivity. The differing results in CO conversion can be attributed to the differences in catalyst composition, as well as reaction conditions (245°C and 60 bar in [21]).

Further tests were performed using FeCoCu-K at higher temperatures, as shown in figure 4.25. Higher reaction temperature produced an increase in conversion (up to 69% at 360°C), with even higher CO<sub>2</sub> selectivity (32%), as well as higher selectivity of heavier hydrocarbons and a reduced selectivity to alcohols (down to barely 3%). Temperature was also detrimental for alcohol chain growth, as shown by the reduced chain growth probabilities.

Higher Alcohol Synthesis: Effect of metal load and reaction conditions

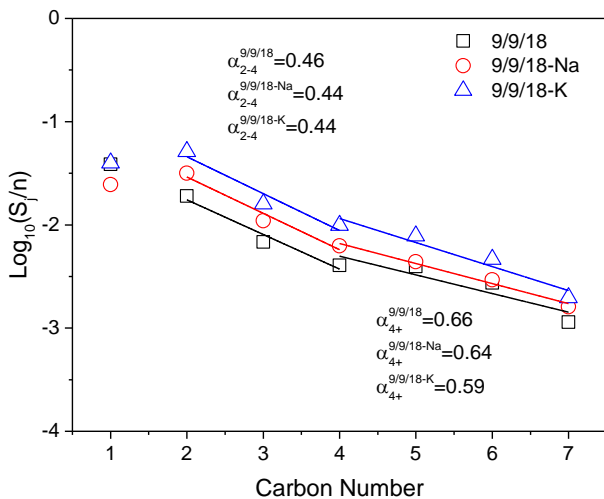
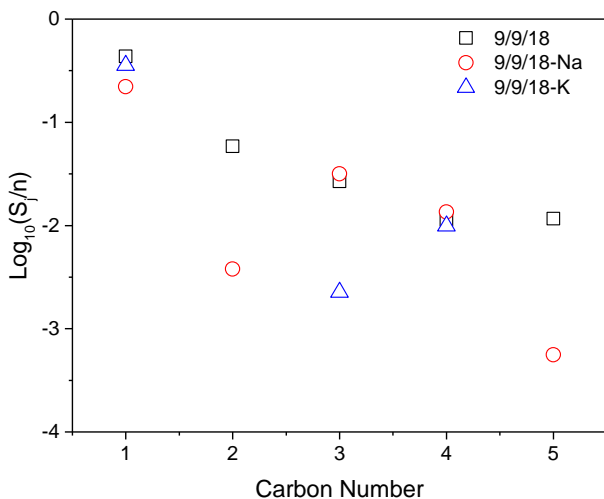
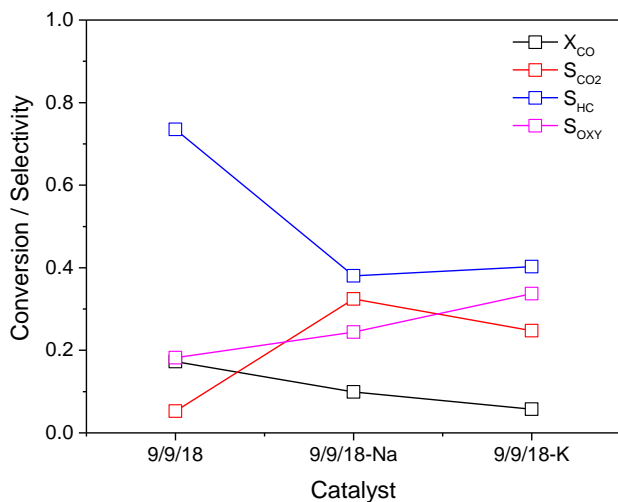


**Figure 4.24.** Effects of alkaline doping in conversion, selectivity, and chain growth probability. Top graph: conversion and selectivity; middle graph: hydrocarbon chain growth probability; bottom graph: alcohol chain growth probability.

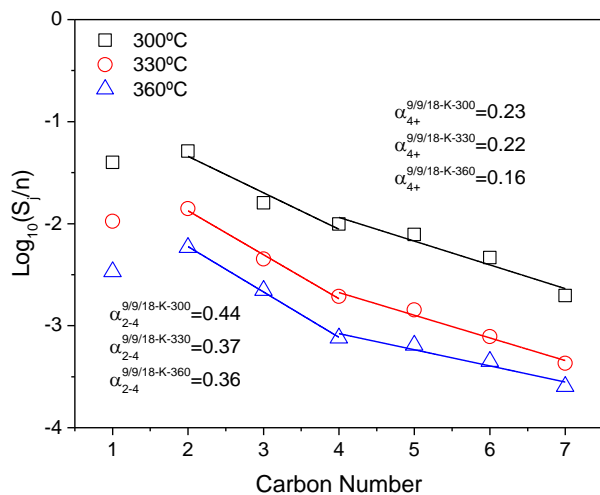
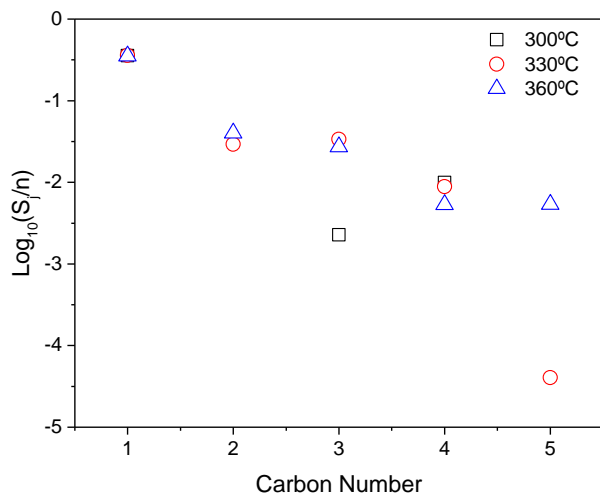
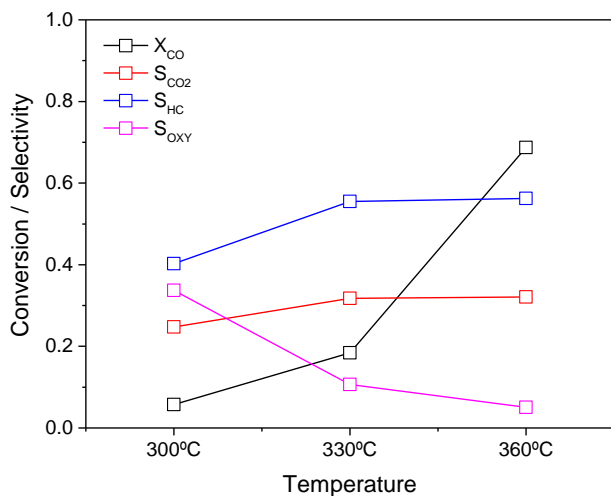


**Figure 4.25.** Effects of temperature in K-doped catalysts in conversion, selectivity, and chain growth probability. Top graph: conversion and selectivity; middle graph: hydrocarbon chain growth probability; bottom graph: alcohol chain growth probability

Overall, we may conclude that alkaline doping – especially with potassium – had positive effects on the formation of higher alcohols, although at the expense of a reduced activity of the catalyst. Increasing reaction temperature evidently increased the overall activity of the doped catalyst but only promoted carbon dioxide and hydrocarbons, while actually hindering the formation of alcohols.

#### 4.3.4. Characterization of spent catalysts

Figure 4.26 shows X-ray diffraction patterns of several samples of used catalysts. Undoped catalysts at 300°C had two main peaks corresponding to metallic Fe and Cu and showed that the active metals remained in metallic phase during the reaction. Concerning average crystallite sizes, there was a slight increase in Fe crystallites from 7.8 to 8.9 nm, and in Cu crystallites from 12.3 to 14.6 nm. Reactions performed at higher temperatures, longer reaction times, or with doped catalysts showed the disappearance of the metallic Fe peaks, which indicated a transformation of the active phases of iron during reaction into non-crystalline phases. Cu crystallite size was similar as that of the used undoped catalysts. The catalysts used at the highest temperature showed a remarkable increase in carbon deposition, as it is well appreciated from the wide peaks centered at 24-26° attributed to graphitic carbon. Overall, it may be concluded from the XRD data that temperature promotes sintering and carbon deposition while blocking alcohol synthesis.

Further evidence of the influence of temperature may be inferred from the TEM images of the used catalysts in Figure 4.19, where they are compared with the unused materials. An evident increase in the average size of the metallic clusters – up to 20-30 nm in diameter – is observed, as expected from the sintering process. Also, at the highest temperature a significant destruction of the SBA-15 support was appreciated, which lost the channeled structure, and caused the migration of the metals to the outer surface of the silica particles.

The used catalyst also showed changes in surface area and porosity, with a 12% decrease in BET surface area, as well as a 51% decrease in micropore volume, which can be attributed to the effects of metal sintering and coke deposition.

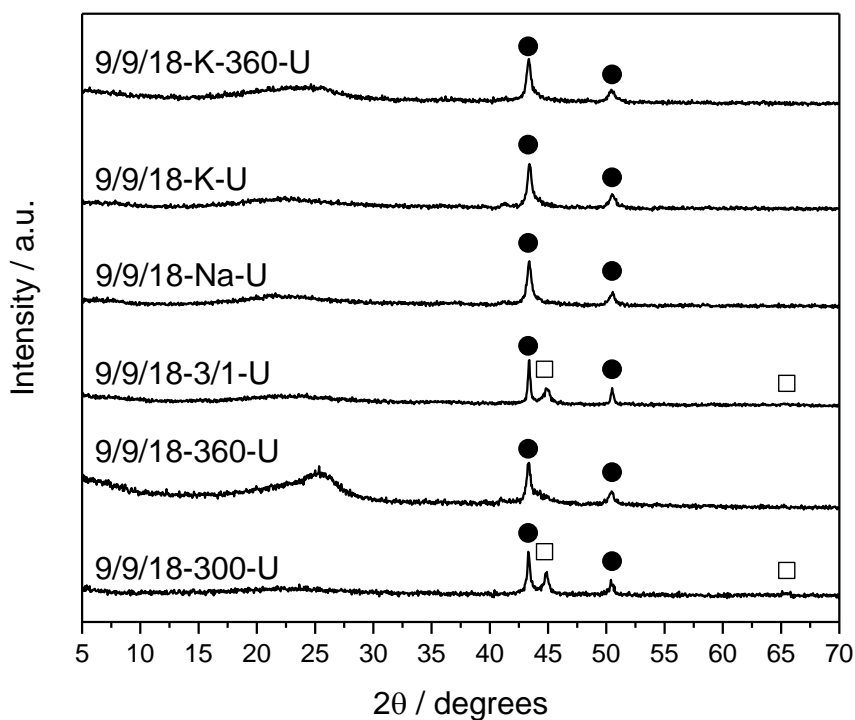


**Figure 4.26.** XRD of used catalysts. Crystalline phases: (□) Fe, (●) Cu.

#### 4.4. Bibliography

- [1] V. Abdelsayed, D. Shekhawat, J.A. Poston Jr., J.J. Spivey, *Catal. Today* 207 (2013) 65-73.
- [2] M. Ding, *Catal. Comm.* 28 (2012) 138-142.
- [3] Z.H. Bao, K. Xiao, X.Z. Qi, X.X. Wang, L.S. Zhong, K.G. Fang, M.G. Lin, Y.H. Sun, *J. Energy Chem.* 22 (2013) 107-113.
- [4] I. Boz, M. Sahibzada, I.S. Metcalfe, *Ind. Eng. Chem. Res.* 33 (1994) 2021-2028.
- [5] V.P. Santos, B. van der Linden, A. Chojecki, G. Budroni, S. Corthals, H. Shibata, G.R. Meima, F. Kapteijn, M. Makkee, J. Gascon, *ACS Catal.* 3 (2013) 1634-1637.
- [6] H. Guo, H. Zhang, F. Peng, H. Yang, L. Xiong, C. Wang, C. Huang, X. Chen, L. Ma, *App. Catal. A* 503 (2015) 51-61.
- [7] P. Sharma, T. Elder, L.H. Groom, J.J. Spivey, *Top. Catal.* 57 (2014) 526-537.
- [8] G. Liu, T. Niu, D. Pan, F. Liu, Y. Liu, *App. Catal. A* 483 (2014) 10-18.
- [9] J. Plana-Pallejà, C. Berruoco, D. Montané, S. Abelló, 25th European Biomass Conference and Exhibition Proceedings, ETA-Florence Renewable Energies, Florence, 2017, 1000-1004.
- [10] D. Förtsch, K. Pabst, E. Groß-Hardt, *Chem. Eng. J.* 138 (2015) 333-346.
- [11] M. Zhang, W. Zhang, W. Xie, Z. Qi, G. Wu, M. Lv, S. Sun, J. Bao, *J. Mol. Catal. A: Chem.* 395 (2014) 269-275.
- [12] X. Zhang, Y. Liu, G. Liu, K. Tao, Q. Jin, F. Meng, D. Wang, N. Tsubaki, *Fuel* 92 (2012) 122-129.
- [13] H.M. Torres Galvis, J.H. Bitter, C.B. Khare, M. Ruitenbeek, A.I. Dugulan, K.P.d. Jong, *Science* 335 (2012) 835-838.
- [14] T. Ishida, T. Yanigahara, X. Liu, X. Ohashi, A. Hamasaki, T. Honma, H. Oji, T. Yokohama, M. Tokunaga, *Appl. Catal. A Gen.* 458 (2013) 145-154.



## Chapter 5

### Concluding remarks

UNIVERSITAT ROVIRA I VIRGILI

CATALYTIC CONVERSION OF SYNGAS TO ALCOHOLS AND HYDROCARBONS OVER TRANSITION METAL-BASED  
MICRO/MESOPOROUS CATALYSTS

Jordi Plana Pallejà

## 5.1. Fischer-Tropsch Synthesis: Effect of zeolite acidity and mesoporosity

The conversion of syngas to hydrocarbons was carried out by using bifunctional catalysts comprising a physical mixture of a synthesized Fe catalyst and ZSM-5 zeolites with two different Si/Al ratios (different inherent acidity). Zeolites were also subjected to alkali treatment to develop a certain degree of hierarchical porosity, that is, the presence of micro- and meso-porosity.

The results confirm that the zeolite acidity is responsible for the cracking of heavy hydrocarbons and the formation of aromatic products through oligomerization, cyclization and dehydrogenation of primary short olefins. The Si/Al ratio induced changes in the composition of the aromatic products. The increment in acidic sites (low Si/Al ratios) induced the formation of more complex aromatic structures. A higher Si/Al ratio in the zeolite led to higher selectivity towards the gasoline-range products. The formation of mesopores in alkaline-treated zeolites exerted a variable behavior depending on the final acidity of the material; ion-exchanged zeolites, which virtually recovered the acidity of the fresh, untreated zeolites, produced a slight increase in C<sub>2</sub>-C<sub>4</sub> paraffins due to an improved access to the acidic sites through the mesopores, and consequently, to the overcracking of heavy molecules. However, the best performance towards gasoline-range hydrocarbons was accomplished with bifunctional catalysts with higher Si/Al ratios, irrespective of the presence of improved accessibility by mesopores. On the opposite side, Na<sup>+</sup> containing catalysts with no acidity behaved similarly to the iron base FTS catalyst, with most of the products in the paraffin range.

This demonstrates that the enhancement of accessibility does not always lead to better performance. In particular, the bifunctional iron/zeolite-based catalyst should exhibit weak acidity to reduce consecutive cracking and thus, to improve the selectivity to C<sub>5</sub>-C<sub>12</sub> gasoline-range hydrocarbons. Therefore, tuning both the acidity and mesoporosity of iron-based bifunctional catalysts is an essential

aspect to guide the FTS product distribution towards a specific hydrocarbon range.

## 5.2. Higher Alcohols Synthesis

The modified Fischer-Tropsch catalysts showed promising capability for the synthesis of higher alcohols. Each one of the active metals – Fe, Co and Cu – had a key role towards the production of the desired products. Fe had excellent activity towards CO conversion. Co reduced selectivity towards the WGS reaction with the subsequent decrease in CO<sub>2</sub> selectivity. Finally, Cu increased selectivity towards alcohols, as well as favored the formation of higher alcohols.

The combination of these three metals in FeCoCu 9/9/9 showed the best selectivity towards higher alcohols, albeit with moderate CO conversion. The synergistic effect of the three metals produced increased selectivity towards higher alcohols without compromising conversion, when compared to any of the binary catalysts. This prompted further investigation of the performance of the ternary FeCoCu catalysts, aiming at finding the best combination of metal loadings to optimize the yield of alcohols. A group of ternary FeCoCu catalysts supported on SBA-15 that contained a maximum total metal load of 36% had been prepared by impregnation, characterized and tested in the synthesis of alcohols. While in all experiments the main products were methane and larger hydrocarbons, conversion and selectivity to the different product groups – carbon dioxide, hydrocarbons and oxygenates – were influenced by the composition of the deposited metals. Iron favored conversion but promoted carbon dioxide formation by the water-gas shift (WGS) reaction and it also lowered the selectivity to alcohols. Cobalt increased the production of hydrocarbons and behaved similarly to iron concerning the selectivity to alcohols. Finally, copper favored methanol and increased the selectivity to long-chain alcohols, while hindering the production of hydrocarbons other than methane when it was in excess over Fe and Co.

Chain growth probabilities ( $\alpha$ ) were higher for alcohols with more than four carbons than for shorter alcohols, whereas in most catalysts growth probabilities for hydrocarbon were close to those of the short-chain alcohols. A notable exception was catalyst FeCoCu 9/9/18, that gave the best selectivity towards the formation of higher alcohols due to its lower hydrocarbon chain grow probability. It was also a catalyst that experienced low sintering and overall gave the best results for the production of higher alcohols. Further testing with varying reaction conditions could be used to determine the best working conditions to improve the yield of alcohols with SBA-15 9/9/18.

In the final section of this thesis, SB-15 9/9/18 was subjected to varying reaction conditions. Factors that increased conversion, such as higher temperature, resulted in an increased selectivity towards hydrocarbons, especially methane. This indicates that Fe is the active metal most sensitive to changes in reaction temperature. Temperature produced the most extreme changes in reaction results, and lower temperatures were necessary in order to facilitate a gain in alcohol selectivity. High contact time was also found to improve conversion while keeping selectivity towards alcohols. A stoichiometric gas ratio did show the best results towards alcohol production, with CO/H<sub>2</sub> feed ratios above or below the stoichiometric showing detrimental effects towards alcohol yield. Finally, alkaline doping did show improved selectivity towards higher alcohols at the expense of lower catalyst activity.

The previous considerations demonstrate that there is a narrow set of reaction conditions that favor the formation of alcohols.

### 5.3. Future work

At the conclusion of this thesis project several questions remain open, which could be addressed in future projects to improve the catalytic systems that had been developed so far:

- Acidity and zeolite porosity have been shown to have noticeable effects on FTS distribution of products. Further work could involve the use of different zeolites, to study the effect of the pore channel distribution and intrinsic acidity on product selectivity. Future research could also be focused on the aqueous fraction of the products, in order to evaluate the presence of water-soluble oxygenated products.
- Further investigation should evaluate the effect of higher-pressure (40-100 bar) on the activity of the FeCoCu/SBA-15 catalysts and their yield of alcohols. The use of different supports, such as non-mesoporous silica, alumina, or carbon nanotubes, would improve the understanding of the effect of the support in the synthesis of higher alcohols. Furthermore, the use of Cu combined with metals other than Fe or Co should be explored to obtain catalytic materials that had better selectivity towards the production of long-chain alcohols.